

**APPROACHES TO INHOMOGENEITY ARTIFACT CORRECTION IN
MAGNETIC RESONANCE IMAGING NEAR METALS**

by

Michael Nicholas Hoff

B.Sc., The University of British Columbia, 1997

M.Sc., The University of British Columbia, 2006

A THESIS SUBMITTED IN PARTIAL FULFILLMENT OF
THE REQUIREMENTS FOR THE DEGREE OF

DOCTOR OF PHILOSOPHY

in

THE FACULTY OF GRADUATE STUDIES

(Physics)

THE UNIVERSITY OF BRITISH COLUMBIA

(Vancouver)

October 2012

© Michael Nicholas Hoff, 2012

Abstract

Clinical procedures such as image-guided surgery and assessment of tissue regions near implants can greatly benefit from magnetic resonance imaging (MRI) near metals. Unfortunately, metals perturb the MRI magnetic field, causing deleterious image distortion, signal loss, and signal overlap artifacts. Several techniques have been developed to correct these artifacts, but those which provide comprehensive solutions require scan times which are too lengthy for time-constrained imaging applications. This study outlines an approach for reconstructing metal artifact corrected images with unique contrast in minimal scan time.

First, a technique was developed to completely eliminate distortion in spin-echo images of metals using added phase gradients along the distorted dimension. Attempts to generalize this technique for the correction of signal loss and overlap artifacts faced difficulties. However, these investigations provoked the discovery of a new framework for imaging near metals.

This framework is based on the balanced steady state free precession (bSSFP) sequence, which generates images near metals with little to no signal overlap, signal loss, and distortion. Two methods were developed to completely remove problematic signal modulation and banding artifacts using four images with variable radiofrequency phase cycling. One technique employs geometric intuition, and the other an algebraic derivation to calculate unique expressions for the same base demodulated signal. The variable performance of the two techniques on noisy data inspires their variance-weighted summation for robust and high performance image reconstruction.

Complementary techniques for reduction of bSSFP signal loss, distortion, and scan time were also devised. Shimming with imaging gradients is shown to recover biphasic signal loss at the cost of extra scan time. Residual distortion is corrected using the phase of the geometric demodulation solution. Two techniques reduce the amount of image data required for signal demodulation.

When all developments are considered, a customized balance of image fidelity and scan time may be achieved. Images without bSSFP banding or distortion may be formed of regions close to metals, and residual signal loss may be recovered at the expense of longer scan time. Additional data reduction measures complete the described framework's capacity for flexible and efficient imaging near metals.

Preface

All research discussed in this report was completed by Professor Qing-San Xiang and myself at the Children's & Women's Health Centre of British Columbia. Guidance for pulse sequence programming and scanner operation was provided by Dr. Jordin Green of Siemens Healthcare.

Table of Contents

Abstract.....	ii
Preface.....	iv
Table of Contents	v
List of Tables	viii
List of Figures.....	ix
List of Abbreviations	xi
List of Symbols	xiii
Acknowledgements	xvii
Chapter 1: Outline.....	1
Chapter 2: Magnetic Resonance Imaging Basics.....	3
2.1 Spins.....	3
2.2 Gradients.....	5
2.2.1 Slice Selection.....	6
2.2.2 Frequency Encoding.....	7
2.2.3 Phase Encoding.....	7
2.3 Fourier Transformation and k-Space	9
2.4 Relaxation	10
2.5 Pulse Sequences	11
2.5.1 Spin Echo.....	11
2.5.2 Gradient Echo	13
2.5.3 Balanced Steady State Free Precession.....	14
2.6 Summary	21
Chapter 3: MRI B_0 Inhomogeneity Artifacts near Metals.....	22
3.1 Background.....	22
3.2 Artifact Source: Susceptibility Effects.....	23
3.3 Artifact Types	25
3.3.1 Distortion	26
3.3.2 Signal Overlap	27
3.3.3 Signal Loss.....	28
3.3.4 Signal Modulation.....	29
3.4 Artifact Correction Techniques.....	30
3.4.1 Standard Clinical Strategies.....	31
3.4.2 B_0 and Susceptibility Mapping.....	32

3.4.3	Single Point Imaging.....	32
3.4.4	UTE.....	32
3.4.5	VAT and MARS	33
3.4.6	SEMAC.....	33
3.4.7	MAVRIC.....	33
3.4.8	Low Field Techniques.....	34
3.4.9	Variable Bandwidth Excitation / Refocusing	35
3.4.10	Multi-Acquisition bSSFP Techniques	35
3.4.11	Which Correction Technique to Choose?.....	37
3.5	Summary.....	37
Chapter 4: B_0 Inhomogeneity Artifact Correction with 3D-PLACE.....		38
4.1	3D-PLACE Distortion Correction	38
4.1.1	Background.....	38
4.1.2	Methods.....	41
4.1.3	Results.....	44
4.1.4	Discussion.....	45
4.2	Multi-Layer 3D-PLACE for Correcting Signal Overlap	46
4.2.1	Theory.....	47
4.2.2	Simulations	49
4.2.3	Phantom Experiments	51
4.3	Summary.....	54
Chapter 5: B_0 Inhomogeneity Artifact Correction with bSSFP		55
5.1	Prelude: a Gradient Echo Technique for Imaging near Metals.....	55
5.2	Geometric Solution for bSSFP Signal Off-Resonance Demodulation	56
5.2.1	Background.....	56
5.2.2	Theory: Geometric Solution	57
5.2.3	Theory: GS-guided Weighted Average	59
5.2.4	Methods: Simulation.....	60
5.2.5	Methods: Experiments	61
5.2.6	Results.....	63
5.2.7	Discussion.....	67
5.3	Algebraic and Geometric-Algebraic Solution for bSSFP Signal Off-Resonance Demodulation.....	69
5.3.1	Background.....	69
5.3.2	Theory.....	70
5.3.3	Methods.....	71
5.3.4	Results: Simulations.....	73
5.3.5	Results: Experiments	76
5.3.6	Results: Performance Comparisons	79

5.3.7	Discussion.....	81
5.4	Shimming bSSFP for Signal Loss Recovery	83
5.4.1	Background.....	84
5.4.2	Methods and Results.....	87
5.4.3	Discussion.....	88
5.5	Using bSSFP Signal Ellipse Phase for Distortion Correction	89
5.5.1	Background.....	90
5.5.2	Methods and Results.....	90
5.6	Imaging Near Metals with bSSFP Discussion.....	93
5.7	Summary.....	94
Chapter 6: Reducing Scan Time of bSSFP Signal Off-Resonance Demodulation.....		95
6.1	Geometric XS-Guided Solution for Reduced-Time Demodulation.....	95
6.1.1	Background.....	95
6.1.2	Methods.....	96
6.1.3	Results.....	97
6.1.4	Discussion.....	99
6.2	Algebraically Weighted Solution for Reduced-Time Demodulation	100
6.2.1	Theory.....	100
6.2.2	Methods.....	102
6.2.3	Results and Discussion	102
6.3	Summary.....	104
Chapter 7: Conclusion.....		105
7.1	Future Work.....	106
7.1.1	Scan Time Reduction.....	106
7.1.2	Comprehensive bSSFP Metal Artifact Correction.....	106
Bibliography.....		107
Appendices.....		119
	Appendix A Derivation of bSSFP Centre-of-Mass	119
	Appendix B Proof: The bSSFP Ellipse Must Be Vertical in the Complex Plane.....	120
	Appendix C Derivation of a Minimal-Variance Sum of Two Images.....	121

List of Tables

Table 2.1 Elliptical characteristics expressed in terms of the bSSFP parameters.	19
Table 3.1 Common material susceptibilities.....	24
Table 5.1 Comparison of 3D-PLACE and geometric solution-guided weighted average (GS-WA) metal artifact correction metrics.	65
Table 5.2 Total relative error (TRE) calculations for simulated data reconstructions.....	76
Table 5.3 The phantom signal-to-noise ratio (SNR) of bSSFP demodulation techniques	78
Table 5.4 Geometric solution, algebraic solution, and geometric-algebraic solution performance comparison.....	81

List of Figures

Figure 2.1	Precession of the magnetization $M(t)$ about the main B_0 magnetic field (1).	4
Figure 2.2	Magnetization $M(t)$ is rotated into the transverse plane.	5
Figure 2.3	Slice selection.	6
Figure 2.4	Slice of water voxels with variable encoding.	8
Figure 2.5	Pulse sequence timing diagram for 2D and 3D gradient echo MRI (1).	9
Figure 2.6	Carr-Purcell-Meiboom-Gill spin echo.	12
Figure 2.7	3D turbo spin echo pulse sequence timing diagram.	12
Figure 2.8	Balanced steady state free precession sequence timing diagram.	15
Figure 2.9	Tissue plot of bSSFP parameters b vs. a .	16
Figure 2.10	bSSFP signal frequency response profile.	17
Figure 2.11	bSSFP elliptical orientation depends on tissue parameters.	20
Figure 3.1	B_0 inhomogeneity artifact categorization map.	25
Figure 3.2	Metal flake in the sinus causes artifacts in turbo spin echo brain images.	26
Figure 3.3	Slice selection (SS) with perturbed frequency-position mapping.	28
Figure 3.4	bSSFP signal magnitude (above) and phase (below) off-resonance profiles.	29
Figure 3.5	bSSFP signal modulation in the eye.	30
Figure 3.6	Through-plane slice skipping / missed excitation.	34
Figure 3.7	Phase-cycled bSSFP frequency response profiles and combination schemes.	35
Figure 4.1	Turbo spin echo (TSE) PLACE pulse sequence timing diagrams.	39
Figure 4.2	The effects of the PLACE gradient on true object phase.	39
Figure 4.3	The phase difference of PLACE images.	40
Figure 4.4	Chromium-cobalt-molybdenum hip prosthesis/Lego phantom.	41
Figure 4.5	CrCoMo/Lego phantom PLACE corrections using variable phase ramps.	43
Figure 4.6	Turbo spin echo (TSE) phantom images and their PLACE corrections.	44
Figure 4.7	Two-layer PLACE (2L) simulation workflow.	50
Figure 4.8	Two-layer PLACE (2L) noisy simulation.	51
Figure 4.9	Bright signal appears to arise from in-plane pixel overlap.	52
Figure 4.10	Phantom PLACE-1L and PLACE-2L corrections.	53
Figure 5.1	bSSFP signal ellipse shows M parameter localization.	57

Figure 5.2 Revised chromium-cobalt-molybdenum hip prosthesis/Lego phantom with fiducial marking.....	62
Figure 5.3 Demodulation of continuously varying bSSFP parameter simulated data.....	63
Figure 5.4 Four phase-cycled CrCoMo/Lego phantom bSSFP magnitude images.....	64
Figure 5.5 Demodulation of bSSFP CrCoMo phantom data.....	64
Figure 5.6 Artifacts vs. true signal loss for the geometric solution-guided weighted average (GS-WA).....	66
Figure 5.7 Geometric solution-guided weighted average (GS-WA) correction of in vivo bSSFP calf images with nearby CrCoMo implant.....	67
Figure 5.8 Demodulation of continuously varying bSSFP parameter simulated data cont'd.....	73
Figure 5.9 Variance maps of continuously varying bSSFP parameter simulated data.....	74
Figure 5.10 Demodulation of segmented “tri-tissue” bSSFP simulated data.....	75
Figure 5.11 Demodulation of bSSFP CrCoMo/water/paté/gelatin phantom data.....	77
Figure 5.12 Demodulation of bSSFP in vivo thigh images.....	79
Figure 5.13 Total relative error (TRE) vs. image noise and T_1/T_2	80
Figure 5.14 Biphasic signal cancellation in the CrCoMo/Lego phantom.....	85
Figure 5.15 Biphasic signal cancellation in a low resolution phantom image.....	86
Figure 5.16 bSSFP pulse sequence timing diagrams with and without shim gradients.....	87
Figure 5.17 Shimming bSSFP for signal loss recovery in the CrCoMo/Lego phantom.....	88
Figure 5.18 Geometric solution a) magnitude and b) phase of the CrCoMo/Lego phantom.....	91
Figure 5.19 Ellipse phase distortion correction in the CrCoMo/Lego phantom.....	92
Figure 6.1 Workflow for the XS-guided solution (XGS).....	96
Figure 6.2 XS-guided solution (XGS) of “tri-tissue” bSSFP simulated data.....	98
Figure 6.3 XS-guided solution (XGS) of bSSFP CrCoMo/Lego phantom data.....	98
Figure 6.4 XS-guided solution (XGS) total relative error (TRE) curves for varied geometric cross-solution k-space coverage.....	99
Figure 6.5 Algebraic weighted solution (AWS) of segmented “tri-tissue” bSSFP simulated data.....	103
Figure 6.6 Algebraic weighted solution (AWS) of bSSFP CrCoMo/Lego phantom data.....	103

List of Abbreviations

AS	Four-image Algebraic Solution
AS2	Two-image Algebraic Solution
AWS	Algebraically Weighted Solution
bSSFP	Balanced Steady State Free Precession
CrCoMo	Chromium Cobalt Molybdenum
CS	Complex Sum
FE	Frequency Encoding
FID	Free Induction Decay
FOV	Field Of View
FT	Fourier Transform
GAS	Four-image Geometric-Algebraic Solution
GRE	GRradient Echo
GS	Four-image Geometric Solution
GS-WA	Four-Image Geometrical Solution-guided Weighted Average
MARS	Metal Artifact Reduction Sequence
MAVRIC	Multi-Acquisition Variable-Resonance Image Combination
MI	Maximum Intensity
MR	Magnetic Resonance
MRI	Magnetic Resonance Imaging
NLA	NonLinear Average
PE	Phase Encoding
PLACE	Phase Labeling for Alternate Coordinate Encoding
PLACE-1L	Single Layer PLACE
PLACE-2L	Double Layer PLACE
RF	Radio Frequency
SNR	Signal-to-Noise Ratio
SE	Spin Echo
SEMAC	Slice Encoding for Metal Artifact Correction
SOS	Sum Of Squares

SS	Slice Selection
SSFP	Steady State Free Precession
TE	Echo Time
TR	Repetition Time
TrueFISP	True Fast Imaging with Steady state Precession (bSSFP)
TRE	Total Relative Error
TSE	Turbo Spin Echo
UTE	Ultra-short Echo Time
VAT	View Angle Tilting
XGS	Low Resolution XS-Guided Solution
XS	Four-image Cross Solution (same as GS)

List of Symbols

a	implant replica image area
b	reconstruction signal loss area
<i>a</i>	bSSFP sample parameter = E_2
<i>b</i>	bSSFP sample/system parameter
<i>d</i>	slice thickness
<i>e</i>	exponential constant = 2.71828
<i>i</i>	imaginary number
k_x	k-space coordinate
k_y	k-space coordinate
<i>m</i>	number of 2π phase twists across FOV
<i>r</i>	polar coordinate
<i>t</i>	time coordinate
<i>w</i>	weighting factor
<i>x</i>	Cartesian coordinate
x'	rotating reference frame coordinate
x_c	elliptical centre <i>x</i> -coordinate
x_j	real component of the <i>j</i> th bSSFP image
<i>y</i>	Cartesian coordinate
y'	rotating reference frame coordinate
y_c	elliptical centre <i>y</i> -coordinate
y_j	imaginary component of the <i>j</i> th bSSFP image
<i>z</i>	Cartesian coordinate
z'	rotating reference frame coordinate
<i>A</i>	elliptical semi-major axis
A_j	signal magnitude of layer <i>j</i>
<i>B</i>	elliptical semi-minor axis
B_0	main magnetic field
B_1	RF excitation magnetic field

B_G	gradient field
BW_{RO}	readout/receiver bandwidth
BW_{RF}	RF pulse bandwidth
E	regional differential energy
E_1	spin-lattice relaxation parameter
E_2	spin-spin relaxation parameter
G_x	frequency encoding gradient
G_y	phase encoding gradient
G_z	slice selection gradient
I	complex image or pixel signal
I_w	weighted signal average
I_{recon}	reconstructed signal
I_{gold}	gold standard signal
Im	imaginary
L	number of overlapping signal layers
M	bSSFP sample/system parameter
M_0	net/equilibrium magnetization
M_j	j th AWS solution
$M_{material}$	material magnetization
$M(t, r)$	precessing magnetization
$M(x, y)$	transverse magnetization
M_{xy}	transverse magnetization
M_x	real component of transverse magnetization
M_y	imaginary component of transverse magnetization
M_z	longitudinal magnetization
M_{AS}	algebraic solution calculation of bSSFP parameter M
M_{GS}	geometric solution calculation of bSSFP parameter M
M_{GAS}	geometric-algebraic solution calculation of bSSFP parameter M
N	number of relatively phase-cycled images
N_x	number of pixels across the x -FOV

O	the original object prior to imaging
P_j	layer j phasor, or point j on the bSSFP signal ellipse
Re	real
R_{eff}	effective resistance
R_j	resistance of resistor j
S	detected signal
T	PE gradient duration, or the magnetic field unit [T] Tesla
T_1	spin-lattice longitudinal relaxation time
T_2	spin-spin transverse relaxation time
T_2^*	spin-spin and field inhomogeneity transverse relaxation time
V_{AS}	regional variance of the algebraic solution
V_{GS}	regional variance of the geometric solution
V_{GAS}	regional variance of the geometric-algebraic solution
Hz	Hertz, a frequency unit
α	RF pulse flip angle
φ	ellipse/off-resonant phase accumulated from $t = 0 \rightarrow TE$
γ	gyromagnetic ratio
π	mathematical constant = 3.14159
θ	off-resonant phase accumulated per TR
θ_0	arbitrary θ value
τ	time between 90° and 180° pulses in a spin-echo sequence
μ_0	permeability of a vacuum
ω	general precession frequency
ω_0	resonant/Larmor precession frequency
χ	magnetic susceptibility
Φ	phase factor
$area_{blip}$	PLACE gradient area
$\Delta\theta$	RF phase cycling increment
$\Delta\omega$	off-resonant frequency shift
Δx	pixel shift along x -direction

Δz	spin mis-localization along z -direction
$\Delta\Phi$	phase difference
$\angle I(\theta)$	bSSFP signal phase
$\langle I \rangle$	bSSFP signal ellipse centre-of-mass

Acknowledgements

I am deeply indebted to my PhD supervisor Prof. Qing-San Xiang for his ceaseless efforts in training me to think critically and to appreciate the elegance of simplified scientific expression. His guidance and intuition created an environment which cultivated inspiration and curiosity.

I'd like to thank my research committee for all their assistance. I appreciate Prof. Piotr Kozłowski's words of wisdom, Prof. Alex MacKay's timely research and career assistance, and Prof. Carl Michal's insightful perspective. I'd also like to thank my examining committee: Prof. Stefan Reinsberg and Prof. David Wilson both dedicated time to perusing this thesis, and offered very insightful questions and comments. Prof. Brian Hargreaves provided detailed suggestions and annotations for this work, and for his comprehensive analysis I am very grateful.

I would also like to thank the National Science and Engineering Research Council, the Children's & Women's Health Centre of British Columbia, and the University of British Columbia for the funding without which my research would not have been possible.

Finally, I thank my daughter for her tolerance, consideration, and grace during the long hours of research. My parents also deserve my gratitude for always standing behind me and supporting my goals. Special thanks to my friends who have kept me strong in times of strife.

Chapter 1: Outline

This thesis will demonstrate novel and efficient techniques for imaging near metals. Chapters 2 and 3 will introduce the basic principles of magnetic resonance imaging (MRI), the image artifacts which arise near metals, and the prevalent methods of correcting those artifacts. It will become apparent that in order to provide good artifact correction, significant scan time is required. The novel research performed by the author and Prof. Qing-San Xiang is described in Chapters 4, 5, and 6. It will be evident that very good images near metals may be acquired in little scan time, and with marginal increases in scan time there lies the possibility of more comprehensive metal artifact correction.

Chapter 2 outlines the basic principles of MRI. A framework covering topics such as spins, gradients, spatial localization, Fourier transformation, and pulse sequences is laid out, providing a foundation for later discussion of topics more specific to the research of this study. Specifically, these descriptions will lay the groundwork for subsequent explanations of image artifacts near metals, and allow an appreciation for the novel correction techniques introduced.

Chapter 3 discusses the source of B_0 imaging artifacts and delineates the types of artifacts observed. Current methods of overcoming these artifacts are outlined, with the understanding that longer scan times are typically necessary for better artifact reduction.

Chapter 4 introduces a novel technique for imaging near metals in moderate scan time. The PLACE technique is applied in concert with 3D imaging for distortion elimination near metals with the acquisition of only two spin-echo images. The possibility of generalizing the technique to a multiple layer model to correct signal loss and overlap artifacts is also explored.

Chapter 5 outlines the principal techniques proposed for imaging near metals. It introduces the balanced steady state free precession (bSSFP) sequence, keys on its efficiency and excellent signal refocusing, and proposes various techniques for metal artifact correction with

bSSFP imaging. The sensitivity of bSSFP to off-resonant magnetization precession is addressed with two cutting edge techniques which exactly demodulate bSSFP signal of its off-resonance dependence. Performance improvements are suggested via linear techniques and a variance-weighted combination. Further bSSFP artifact reduction is then explored with methods for signal loss recovery through inhomogeneous field shimming and residual distortion elimination with demodulation phase data. Finally, the techniques are discussed in terms of their utility for imaging near metals, and conclusions made on their clinical viability for flexible artifact correction near metals.

The bSSFP imaging demodulation efforts of Chapter 5 indicate an inherent redundancy through the existence of two independent four image solutions. This inspires demodulation efforts using less data, which would be advantageous for time-constrained procedures such as motion-sensitive imaging. Chapter 6 demonstrates two techniques which exploit the fact that the weighted average of two alternately phase-cycled bSSFP images yields a demodulated solution. One method demonstrates that a subsampled geometric cross solution can successfully guide the linear solution, while the other method indicates that a two image algebraic solution can achieve respectable debanding.

Finally, Chapter 7 concludes on the findings, and makes recommendations for further work.

Chapter 2: Magnetic Resonance Imaging Basics

This chapter outlines the basic principles of magnetic resonance imaging (MRI). A framework covering topics such as spins, gradients, spatial localization, Fourier transformation, and pulse sequences is laid out, providing a foundation for later description of image artifacts near metals. Furthermore, this introduction will allow an appreciation for the novel artifact correction techniques that will be demonstrated. Just as one should understand the inner workings of a car prior to attempting its repair, here the inner workings of MRI are briefly described to provide background for metal artifact correction.

2.1 Spins

Although MRI is fundamentally a quantum mechanical technique, it may be elegantly described by classical physics. Nuclei with an odd number of protons or neutrons have an intrinsic magnetic propensity, or magnetic moment; MRI is most often concerned with the magnetic moment of “spins” such as hydrogen’s proton.

Spins within an external magnetic field B_0 are subjected to a magnetic torque, yielding spin precession at the Larmor frequency ω_0 :

$$\omega_0 = \gamma B_0 \quad [2.1]$$

where γ is the gyromagnetic ratio particular to the nucleus in [radians/second/Tesla], such that if the field is in Tesla [T], the ω_0 frequency is in [radians/second]. Any computations of frequency in Hertz [Hz] will require a substitution of $\gamma \rightarrow \gamma/2\pi$.

An excess of these spins polarize along the B_0 field direction, forming a net magnetization M_0 along the physical z-axis by convention. Figure 2.1 demonstrates the classical perspective of the precessing net magnetization $M(t)$ about B_0 :

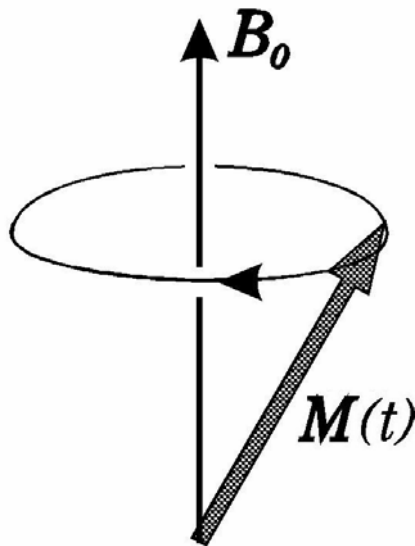


Figure 2.1 Precession of the magnetization $M(t)$ about the main B_0 magnetic field (1).

The key to MRI is in the manipulation of $M(t)$ in order to reveal characteristic information of its representative tissue. The first step is to employ an orthogonally oriented coil to excite $M(t)$ with an alternating radiofrequency (RF) current tuned to the resonant frequency ω_0 . Commonly an RF pulse is applied to rotate the magnetization by 90° into the physical xy plane orthogonal to the B_0 direction, otherwise known as the transverse or complex plane. Figure 2.2 depicts this secondary B_1 magnetic field rotating $M(t)$ into the transverse plane when viewed from a reference frame rotating at ω_0 . The subsequent transverse magnetization M_{xy} will continue to precess, permitting eventual detection by appropriately oriented receiver coils.

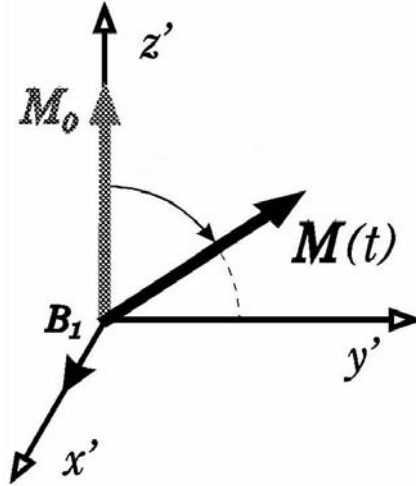


Figure 2.2 Magnetization $M(t)$ is rotated into the transverse plane. The B_1 field rotates the net magnetization M_0 in a rotating frame x', y', z' (1).

2.2 Gradients

Image creation is achieved by spatially differentiating signal with magnetic field gradients. A magnetic field B_G is superimposed with the same directionality as B_0 but variable strength as a function of position r

$$B_G = r \cdot G = xG_x + yG_y + zG_z \quad [2.2]$$

For 2D MRI, spatial localization of signal is achieved along three orthogonal gradient directions, denoted G_z slice selection (SS), G_x frequency encoding (FE), and G_y phase encoding (PE); Figure 2.5b will show that G_z is supplemented with an added PE gradients for 3D MRI. While the physical coordinates x, y, z defined earlier depend on the direction of B_0 , the $G_x, G_y,$ and G_z directions are logical naming conventions that can be set in any desired physical orientation. The resultant field is a superposition of B_G and B_0 , such that ω_0 given in Eq. [2.1] varies with position.

2.2.1 Slice Selection

The SS gradient G_z causes spins along the logical z -axis to precess at different frequencies. Equation [2.1] becomes

$$\omega(z) = \gamma(B_0 + z \cdot G_z) \quad [2.3]$$

An RF pulse of frequency ω_0 will ideally excite a slice of spins perpendicular to the z -axis at one position z where $\omega(z) = \omega_0$, as depicted in Figure 2.3

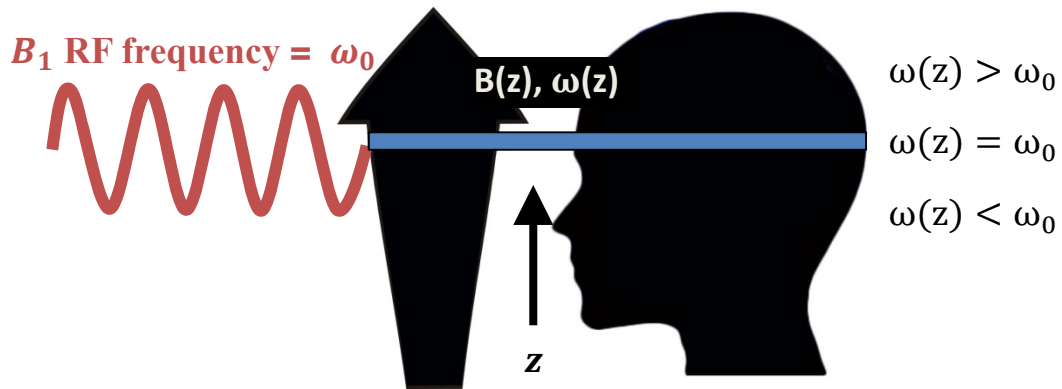


Figure 2.3 Slice selection. A radiofrequency pulse of frequency ω_0 will ideally excite a slice of spins perpendicular to the logical z -axis at one position z where $\omega(z) = \omega_0$.

An RF pulse's amplitude modulation over time excites a frequency range of spins defined by the pulse bandwidth BW_{RF} , which due to the gradient corresponds to a slice thickness d :

$$d = \frac{2\pi BW_{RF}}{\gamma G_z} \quad [2.4]$$

After the pulse, only spins within the slice will have transverse magnetization M_{xy} that can be used to induce signal in a receiver coil. Selective 3D MRI employs a reduced slice gradient amplitude in order to excite a thick “slab” of spins, and adds z -phase encoding.

2.2.2 Frequency Encoding

Once the slice selection gradient is turned off, a linear FE gradient field G_x is applied along the logical x -axis of the excited slice, encoding spins with variable frequency (2). The field in the slice is a superposition of the B_0 field and G_x , modifying the frequency values of Eq. [2.1]

$$\omega(x) = \gamma(B_0 + x \cdot G_x) \quad [2.5]$$

While the SS gradient prepares spins for slice excitation with frequency encoding along the z -axis, the FE gradient encodes all excited spins in the slice for signal localization along the x -axis.

2.2.3 Phase Encoding

After the SS but prior to the FE gradient, a PE gradient G_y is applied along the logical y -axis for a finite period T (3,4). During G_y , spins along y will have variable frequency. After G_y , spins along y will return to equivalent frequencies of precession, but their phase $\Phi(y)$ in a frame rotating with the Larmor frequency will be variable:

$$\Phi(y) = \gamma(y \cdot G_y \cdot T) \quad [2.6]$$

where Eq. [2.6] gives the position-dependent phase caused by a rectangular PE gradient. After the application of a phase encoding gradient along y , frequency encoding along x is applied and signal is detected; Figure 2.4 from Bjarnason *et al.* (5) shows how each voxel (volume element) in a slice will have unique frequency and phase information at this point.

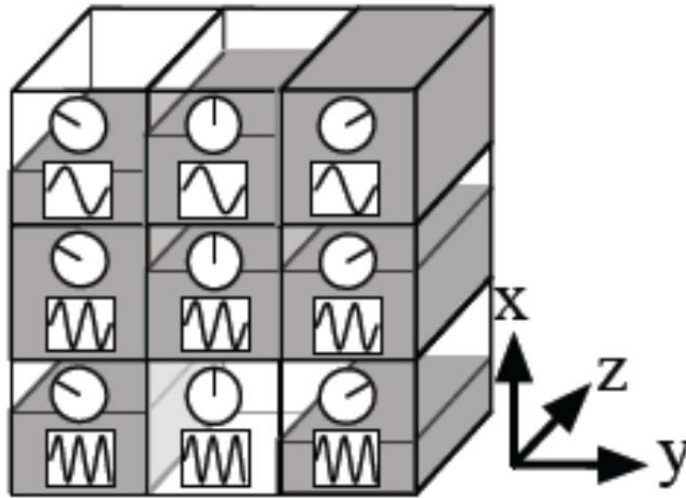


Figure 2.4 Slice of water voxels with variable encoding. Phase and frequency encoding yield variable proton phase indicated by the “clocks” along y , and variable frequency indicated by sinusoidal waves along x . © Thoranin Albert Bjarnason, 2011, by permission (5).

Phase encoding is time consuming, as it must be repeated over a range of amplitudes to achieve the desired y -resolution. However, it yields excellent spatial resolution. Figure 2.5 depicts pulse sequence timing diagrams for 2D and 3D MRI, showing the above described steps as they are implemented by the MRI hardware. The RF pulse, gradients, and signal acquisition are delimited vertically, and their relative timing is represented horizontally.

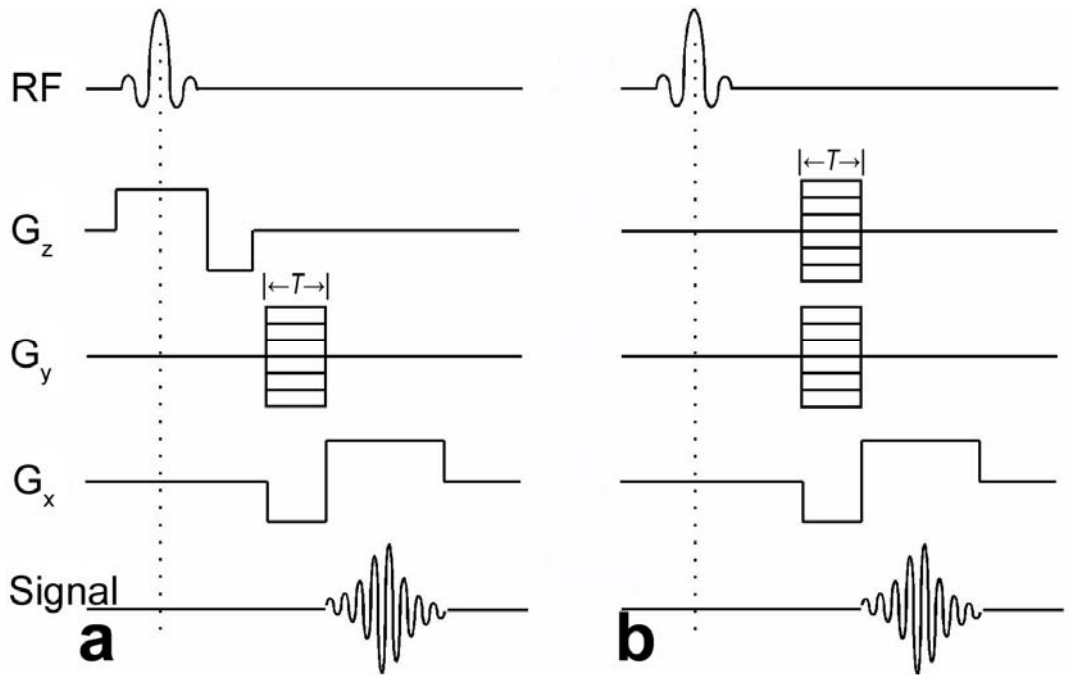


Figure 2.5 Pulse sequence timing diagram for 2D and 3D gradient echo MRI (1). a) 2D pulse sequence includes the radiofrequency (RF) pulse, frequency encoding G_x , phase encoding G_y , and slice selection G_z gradients. b) 3D pulse sequence adds phase encoding along the G_z axis. Timing is horizontal, and T is the G_y gradient duration.

2.3 Fourier Transformation and k-Space

Gradients cause spins to dephase, or become incoherent in a given voxel. Pulse sequences enable signal coherence within a voxel through rephasing. At a certain point during the FE readout gradient, signal is detected that is comprised of all rephased spins across the slice. This is directly proportional to the integral of the magnetization $M(r)$ over all positions r in the slice, multiplied by complex phase factors Φ representing the unique spin frequencies and phase of each voxel

$$Signal \propto \int M(r)e^{i\Phi} dr \quad [2.7]$$

These positions r may be separated into x and y components to quantify the contributions of the FE and PE gradients. Assuming rectangular gradients, G_x contributes a phase rotation of

$\gamma x G_x t$ at position x and time t measured from the center of the echo, while G_y of duration T contributes a phase rotation of $\gamma y G_y T$. Substituting

$$k_x = \frac{\gamma}{2\pi} G_x t \quad [2.8]$$

$$k_y = \frac{\gamma}{2\pi} G_y T \quad [2.9]$$

permits Eq. [2.7] to be rewritten

$$S(k_x, k_y) = \int M(x, y) e^{i2\pi(x \cdot k_x)} e^{i2\pi(y \cdot k_y)} dx dy \quad [2.10]$$

Here effects such as coil sensitivity, diffusion, and relaxation are incorporated into the magnetization. This tells us that the desired image magnetization $M(x, y)$ and the signal $S(k_x, k_y)$ form a Fourier transform (FT) pair. The signal is acquired in Fourier space, or “k-space”, and a 2D FT of the data will yield the image space.

2.4 Relaxation

Relaxation is the tendency for the net magnetization to realign with B_0 and return to thermal equilibrium M_0 . Transverse magnetization M_{xy} loses phase coherence as random oscillating magnetic fields between spins cause M_{xy} to decay at a rate inversely dependent on the T_2 transverse relaxation time. External magnetic field inhomogeneity can cause additional dephasing and further shorten this time; the resulting T_2^* relaxation is the primary cause of signal loss artifacts that will be discussed in future chapters. Simultaneously, the spin system transfers energy to its environment via spin-lattice relaxation, and returns to thermal equilibrium along the B_0 “longitudinal” direction at a rate inversely correlated with the longitudinal T_1 relaxation time. These relaxation times vary from tissue to tissue due to differentiated molecular environments.

2.5 Pulse Sequences

Pulse sequences achieve signal detection by rephasing magnetization that has previously been dephased to incoherence during the gradient encoding procedure. Spin-echo (SE) pulse sequences flip transverse magnetization with an RF pulse of angle $\alpha = 180^\circ$ to reverse the dephasing process, while gradient echo sequences (GRE) use alternating polarity gradients. MRI has many pulse sequences from which to choose, each yielding a different level of refocusing efficiency and image contrast. Balanced steady state free precession (bSSFP) sequences are typically considered to be a specialized GRE sequence, but are described here in a separate category due to their unique characteristics and importance to this study.

2.5.1 Spin Echo

The Carr-Purcell SE pulse sequence (6,7) involves an initial RF pulse that rotates the longitudinal magnetization M_z by a flip angle $\alpha = 90^\circ$ into the transverse plane. At time τ after the original 90° pulse, a 180° pulse flips the dephased spins like a pancake. A reversal of the original dephasing process occurs, and at time 2τ spins rephase to form a detectable “spin-echo”. RF amplitude error is reduced with the Carr-Purcell-Meiboom-Gill SE sequence (8), which applies the $\alpha = 90^\circ$ excitation pulse and the $\alpha = 180^\circ$ refocusing pulse along orthogonal axes; this process is illustrated in Figure 2.6. Spin-echo signal experiences contrast. Other characteristic T_2 rather than T_2^* , as it reverses the effects of local field inhomogeneity-induced frequency shifts within a voxel. It is thus typically employed for imaging in inhomogeneous magnetic fields near metals, as will be further discussed next chapter.

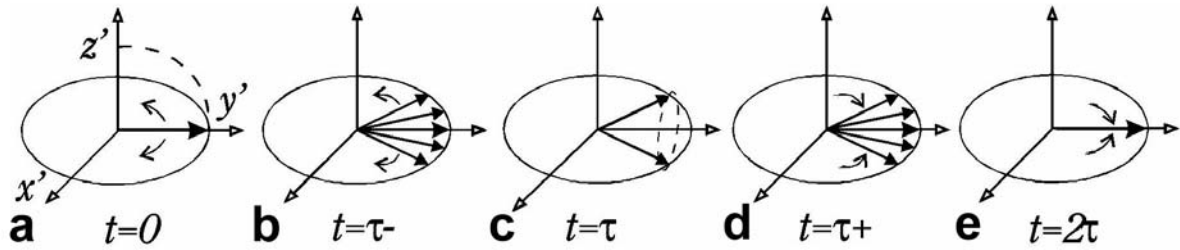


Figure 2.6 Carr-Purcell-Meiboom-Gill spin echo. a) After a flip about the rotating frame x' axis into the xy plane, magnetization is coherent along y' . b) Spins dephase. c) 180° pulse about y' flips dephased magnetization at time $t = \tau$. d) Magnetization rephases. e) Magnetization is refocused at $t = 2\tau$.

Rapid acquisition with relaxation enhancement (9), turbo spin echo (TSE), and fast spin echo pulse sequences continually flip the magnetization with 180° pulses until T_2 relaxation unrecoverably diminishes M_{xy} ; this increases the imaging efficiency of the relatively slow SE technique. A 3D version of the TSE pulse sequence timing diagram is demonstrated in Figure 2.7.

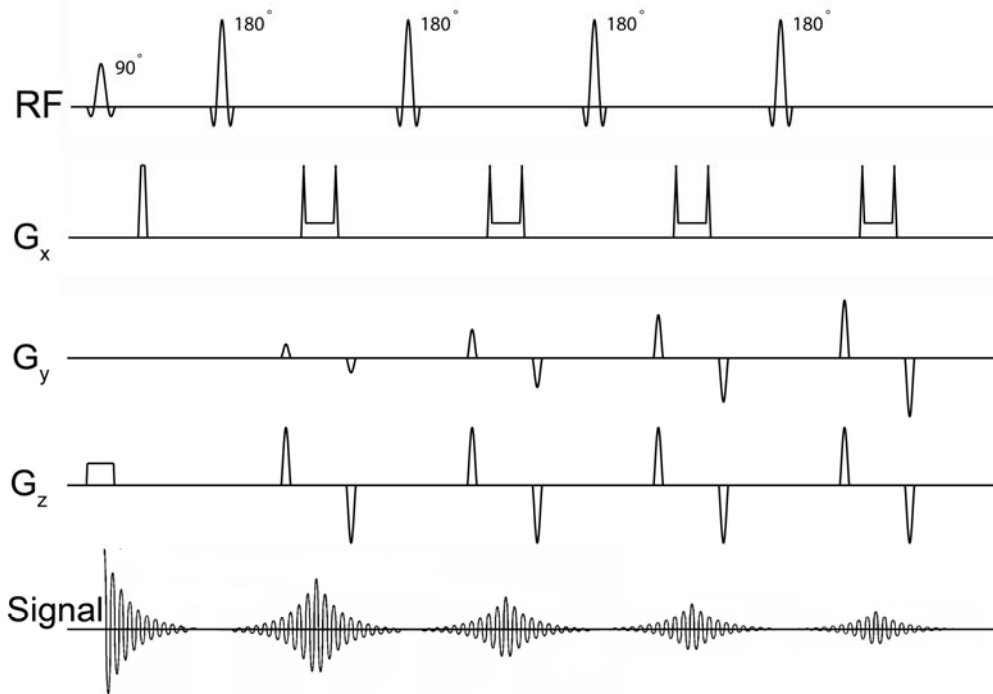


Figure 2.7 3D turbo spin echo pulse sequence timing diagram. 90° RF pulse flips magnetization into the transverse plane and 180° pulses continually refocus magnetization for detection. G_z has phase encoding in this 3D sequence.

2.5.2 Gradient Echo

When an RF pulse rotates magnetization into the transverse plane, free induction decay (FID) signal is generated. The GRE pulse sequence (10) dephases the FID with a prephasing FE gradient, and then rephases signal with an FE “readout” gradient of opposing polarity, as depicted in the GRE pulse sequence timing diagram illustrated in Figure 2.5. As the gradients balance during the readout, a rephased gradient-recalled echo may be detected. GRE sequences typically employ one RF pulse with $\alpha < 90^\circ$ within each repetition time TR, and repeat the TR segment until a dynamic equilibrium is established.

GRE imaging is faster than SE imaging, with higher sensitivity to field inhomogeneity. While the 180° pulse in SE sequences refocuses intravoxel phase evolution caused by magnetic field inhomogeneity, GRE sequences’ off-resonant phase continues to accumulate until the echo time (TE). GRE sequences are thus weighted by T_2^* ; as shall be seen next chapter, the subsequent dephasing that ensues causes signal loss near metals (11,12).

GRE pulse sequences can be classified according to the state of the transverse magnetization at the end of each TR (13,14). “Spoiled” sequences employ spoiler gradients and random RF phase cycling (shifts in the RF phase) to destroy residual transverse magnetization prior to each RF pulse (10). Thus only the longitudinal magnetization M_z achieves a steady state (15). Steady state free precession (16,17) imaging sequences (SSFP) refocus residual transverse magnetization by ensuring that gradient areas are equal and RF pulse phases are equal or progressively cycled from TR to TR. If $TR < T_2$, both M_z and M_{xy} will achieve a steady state.

The SSFP real and imaginary transverse magnetization components M_x and M_y are given by (17,18)

$$M_x(0) = M_0 \frac{(1 - E_1)(1 - E_2 \cos \theta) \sin \alpha}{(1 - E_1 \cos \alpha)(1 - E_2 \cos \theta) - (E_1 - \cos \alpha)(E_2 - \cos \theta)E_2} \quad [2.11]$$

$$M_y(0) = M_0 \frac{-(1 - E_1)E_2 \sin \theta \sin \alpha}{(1 - E_1 \cos \alpha)(1 - E_2 \cos \theta) - (E_1 - \cos \alpha)(E_2 - \cos \theta)E_2} \quad [2.12]$$

$$E_1 = e^{-\frac{\text{TR}}{T_1}} \quad E_2 = e^{-\frac{\text{TR}}{T_2}} \quad \theta = \Delta\omega \cdot \text{TR} \quad [2.13]$$

when measured directly after an excitation pulse at $t = 0$. The local spin frequency off-resonance is given by $\Delta\omega$, and θ is the off-resonant phase evolution per TR. The complex transverse magnetization M_{xy} at time $t = \text{TE}$ may be computed with Eqs. [2.11] and [2.12] given that $M_{xy}(0) = M_x(0) + iM_y(0)$

$$M_{xy}(\text{TE}) = M_{xy}(0)e^{-i\varphi}e^{-\text{TE}/T_2} \quad [2.14]$$

where

$$\varphi = \Delta\omega \cdot \text{TE} = \frac{\theta \cdot \text{TE}}{\text{TR}} \quad [2.15]$$

The factors $e^{-\text{TE}/T_2}$ and $e^{-i\varphi}$ account for the T_2 decay and off-resonant phase evolution that occur from $t = 0 \rightarrow \text{TE}$.

2.5.3 Balanced Steady State Free Precession

Of particular importance to this treatise is the bSSFP sequence (19), which is essentially an SSFP sequence with balanced gradients that sum to zero along each axis within a given TR. This may be observed in its pulse sequence timing diagram shown in Figure 2.8.

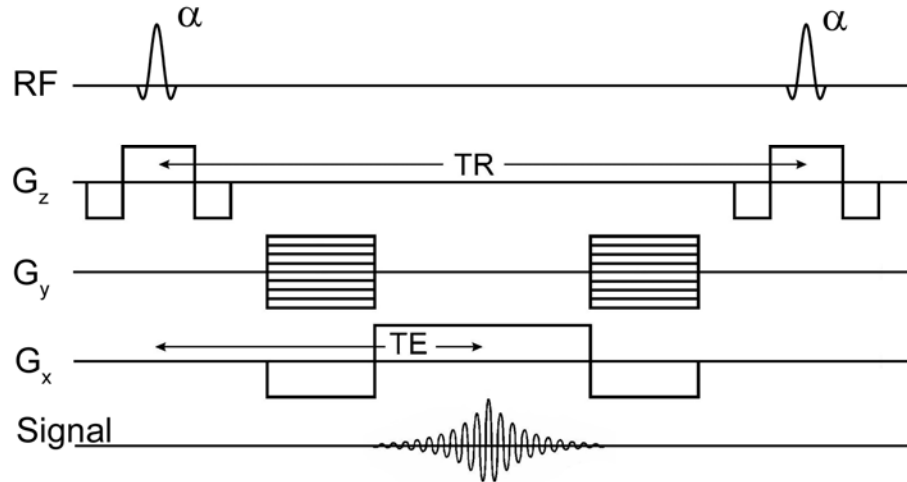


Figure 2.8 Balanced steady state free precession sequence timing diagram. All gradients are balanced and symmetric, $TE = TR/2$, and $\alpha < 90^\circ$. It achieves both longitudinal and transverse magnetization steady states.

Signal acquisition at the center of the TR interval permits very spin-echo-like refocusing (18,20) of up to half the equilibrium magnetization, but the sequence suffers from signal modulation as a function of off-resonant phase accumulation. Shortened TR has been facilitated by the advent of more powerful gradients, limiting off-resonant phase evolution and clinically entrenching this efficient sequence (21).

The bSSFP signal $M_{xy}(TE)$ may be reformulated in parametric form as the complex $I(\theta)$, taking $TE = TR/2$ into account (22,23):

$$I(\theta) = M \frac{1 - ae^{i\theta}}{1 - b \cos \theta} e^{-i\theta/2} e^{-TE/T_2} \quad [2.16]$$

where

$$M = \frac{M_0(1 - E_1) \sin \alpha}{1 - E_1 \cos \alpha - E_2^2(E_1 - \cos \alpha)} \quad [2.17]$$

$$b = \frac{E_2(1 - E_1)(1 + \cos \alpha)}{1 - E_1 \cos \alpha - E_2^2(E_1 - \cos \alpha)} \quad [2.18]$$

$$a = E_2 \quad [2.19]$$

The parameters a and b must be valued between 0 and 1 (23), and are dependent on tissue (T_1, T_2) and system (α, TR) characteristics. The parameter M is additionally dependent on the M_0 equilibrium magnetization, and must be real. Figure 2.9 demonstrates where certain tissues fall in a b vs. a plot if $\alpha = 41^\circ$, $TR = 4.2\text{ms}$, and approximate T_1 and T_2 values are taken from the literature (24-28).

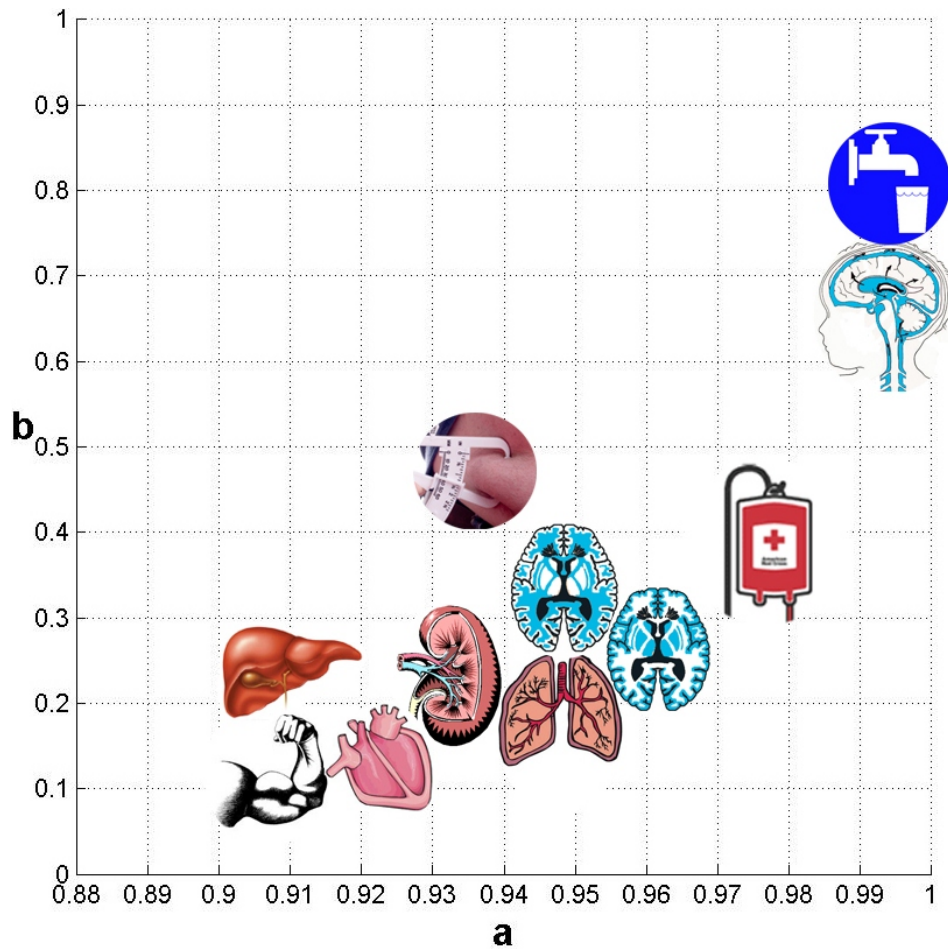


Figure 2.9 Tissue plot of bSSFP parameters b vs. a . Generalized values for muscle, liver, heart, kidneys, fat, lungs, white matter, grey matter, blood, cerebrospinal fluid, and water shown left to right were calculated using Eqs. [2.18] and [2.19] with $\alpha = 41^\circ$ and $TR = 4.2\text{ms}$.

The bSSFP sequence differentiates T_1/T_2 ratios, such that there is strong contrast between blood/fat/liquids and muscle/tissue. The flip angle α , added magnetization preparation

sequence blocks, and the length of the preparatory stage prior to onset of the steady state can also influence contrast (15,29).

Note that the newly defined parameters M , a , and b are all independent of the θ off-resonant phase evolution. Next chapter will outline how θ stems predominately from regional field inhomogeneity that is especially acute near metals, implying that these parameters will prove to be useful for imaging near metals with bSSFP.

Figure 2.10 demonstrates simulated bSSFP magnitude/phase frequency response profiles over a 4π range of θ off-resonance using Eq. [2.16] with $T_1 = T_2 = 3000\text{ms}$, and $\alpha = 40^\circ$.

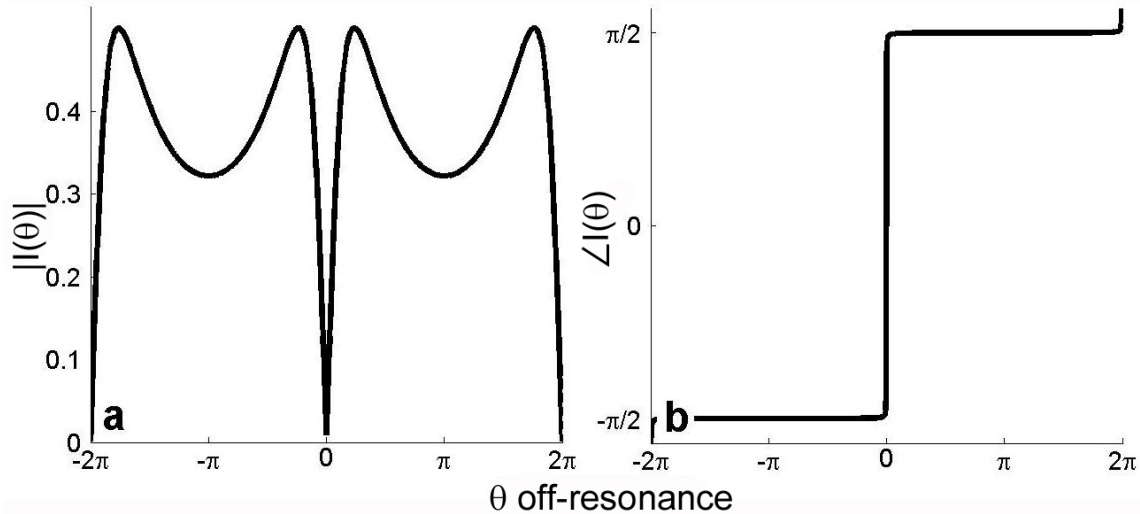


Figure 2.10 bSSFP signal frequency response profile. a) Magnitude and b) phase plots are simulated using Eq. [2.16], with $T_1 = T_2 = 3000\text{ms}$, and $\alpha = 40^\circ$ over a 4π range of off-resonance θ .

The relatively flat bSSFP phase demonstrates the spin-echo-like refocusing of bSSFP; this signal phase may be derived from Eq. [2.16] to yield an slightly different expression than that derived in Schmitt *et al.* (30):

$$\angle I(\theta) = \tan^{-1} \left(\frac{1+a}{1-a} \tan \frac{\theta}{2} \right) \quad [2.20]$$

The $(1+a)/(1-a)$ factor can dominate the expression when $\text{TR} \ll T_2$, causing the signal phase to be almost independent of off-resonance θ , save for the singular values of the tangent

that shift the phase by $\pm\pi$. This $\pm\pi$ binary phase change in Figure 2.10b occurs at the banded signal drop regions of Figure 2.10a, which are of particular interest to this study.

Another powerful way to visualize bSSFP magnetization is in the complex plane; this perspective will prove to be especially useful when a geometric bSSFP θ -demodulation technique is introduced in a later chapter. When $TE = 0$ such that $I(\theta) = M(1 - ae^{i\theta})/(1 - b \cos \theta)$, the locus of magnetization vectors $I(\theta)$ for $\theta = 0 \rightarrow 2\pi$ trace out an ellipse in the complex plane (18,31,32). If $TE = TR/2$, multiplication by $\exp(-TE/T_2)$ uniformly diminishes all values in a given ellipse, which is not important in the context of this study due to the factor's independence of the θ off-resonance value. Multiplication by the $\exp(-i \cdot \theta/2)$ factor coupled with the symmetric gradients of bSSFP essentially flattens the elliptical variation into a biphasic line of values. The multiplication may alternatively be viewed as a simple rotation of the $TE = 0$ signal ellipse by an angle $\varphi = \theta/2$. If the ellipse is considered from a reference frame rotating with this “ellipse phase” φ , the phase factor may be safely ignored.

A standard Cartesian-form ellipse is expressed in Eq. [2.21] of Table 2.1, where A and B are the semi-major and semi-minor axes, and (x_c, y_c) are the centre coordinates. Substituting the real $x = \text{Re}[I(\theta)]$ and imaginary $y = \text{Im}[I(\theta)]$ components of the $I(\theta)$ signal permits the bSSFP magnetization to be similarly expressed in complex plane Cartesian coordinates. Table 2.1 gives a list of elliptical parameters such as x_c , y_c , A , and B in terms of bSSFP parameters a , b , and M .

Elliptical property	Expression
Cartesian elliptical form	$1 = \frac{(x - x_c)^2}{A^2} + \frac{(y - y_c)^2}{B^2}$ [2.21]
Parametric elliptical form	$I(\theta) = M \frac{1 - ae^{i\theta}}{1 - b \cos \theta}$ [2.22]
Geometric centre position	$(x_c, y_c) = \left(M \frac{1 - ab}{1 - b^2}, 0 \right)$ [2.23]
Center-of-mass	$\langle I \rangle = M \left[1 + \frac{b - a}{b} \left(\frac{1}{\sqrt{1 - b^2}} - 1 \right) \right]$ [2.24]
Semi-major/minor axes	$A = M \frac{ a - b }{1 - b^2} \quad B = M \frac{a}{\sqrt{1 - b^2}}$ [2.25]
Major/minor condition	$\begin{aligned} \text{if } b < \frac{2a}{1 + a^2}, \quad A < B \\ \text{if } b > \frac{2a}{1 + a^2}, \quad A > B \end{aligned}$ [2.26]
Eccentricity	$= \begin{cases} \sqrt{1 - \frac{(a - b)^2}{a^2(1 - b^2)}} & \text{if } A < B \\ \sqrt{1 - \frac{a^2(1 - b^2)}{(a - b)^2}} & \text{if } A > B \end{cases}$ [2.27]
Focci positions	$= \begin{cases} 0, \pm M \frac{\sqrt{ b^2 - 2ab + a^2b^2 }}{1 - b^2} & \text{if } A < B \\ \pm M \frac{\sqrt{ b^2 - 2ab + a^2b^2 }}{1 - b^2}, 0 & \text{if } A > B \end{cases}$ [2.28]

Table 2.1 Elliptical characteristics expressed in terms of the bSSFP parameters. Equation [2.21] with $x = \text{Re}[I(\theta)]$ and $y = \text{Im}[I(\theta)]$ and Eq. [2.22] are used to describe the ellipse in terms of a , b , and M .

Most of these parameter derivations required relatively straightforward calculations; an exception is the ‘‘centre-of-mass’’ $\langle I \rangle$ derived in Appendix A. Equation [2.26] shows that

depending on the relative size of b and $2a/(1 + a^2)$, $A < B$, $A > B$, or $A = B$. That is, the ellipse may have its semi-major axis horizontally oriented, vertically oriented, or circular in the complex plane. Figure 2.11a describes this relationship in a b vs. a plot similar to the tissue plot of Figure 2.9, with the horizontal and vertical ellipse regions listed on either side of the $b = 2a/(1 + a^2)$ “circle-line”. A specific example of horizontal and vertical ellipses is shown in Figure 2.11b; however, Appendix B shows that since $0 < E_1, E_2 < 1$ and $-1 < \cos \alpha < 1$, real-world ellipses are always vertical in the complex plane.

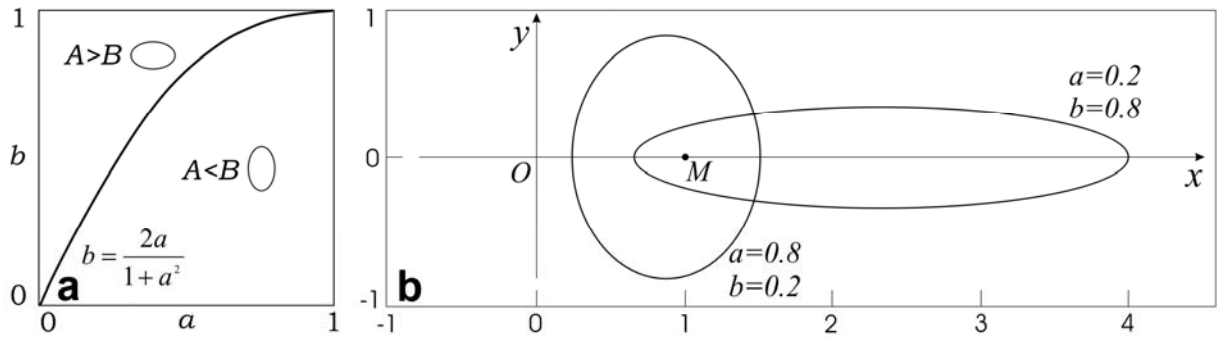


Figure 2.11 bSSFP elliptical orientation depends on tissue parameters. a) $A < B$ corresponds to vertical and $A > B$ to horizontal signal ellipses in (a, b) parameter space. $A = B$ or $b = 2a/(1 + a^2)$ yields a circle. b) The vertical ellipse with $(M, a, b) = (1, 0.8, 0.2)$ corresponds to $(A, B) = (0.6250, 0.8165)$, and the horizontal ellipse with $(M, a, b) = (1, 0.2, 0.8)$ corresponds to $(A, B) = (1.667, 0.3333)$.

The bSSFP sequence is characterized by a unique combination of biphasic spin-echo-like magnetization refocusing and signal modulation that is periodic in off-resonance. Reframing the bSSFP signal into parametric equations and modeling the off-resonant response in the complex plane enables an interesting visualization of the signal. It has an elliptical profile with characteristic points that are independent of the off-resonance modulation if considered from a rotating frame of reference. Further discussion on this topic is left for sections 3.3.4 and 5.2; readers interested in a slightly different geometric perspective of the bSSFP signal are directed to Schmitt *et al* (33).

2.6 Summary

The basics of MRI have been outlined to paint the technical backdrop for this study. The described relationship between magnetic fields and precession frequency will be referenced ubiquitously. The spatial localization and gradient concepts discussed here are essential for comprehension of the mechanisms responsible for the metal artifacts discussed in the next chapter. The pertinent characteristics of the bSSFP pulse sequence have been outlined, which will pay dividends when introducing the principal developments of this study.

Chapter 3: MRI B_0 Inhomogeneity Artifacts near Metals

While MRI is a powerful diagnostic tool, the presence of metals within the scanner can pose obstacles to the imaging procedure. Here the source of B_0 imaging artifacts is discussed, followed by a delineation of the types of artifacts observed. Finally, current methods of overcoming these artifacts are outlined, with the understanding that longer scan times are typically necessary for better artifact reduction.

3.1 Background

Metals are becoming very common in the human body, and it is frequently desirable to image near them. Orthopedic screws and prosthetics are often employed in the repair and reconstruction of joints; potential loosening, abrasion, infection, fracture, and osteolysis (34-36) could be diagnosed at onset with imaging. Brain imaging is essential in spite of a patient's metal braces or plates, and image-guided surgery frequently employs metallic devices such as biopsy needles. Computed tomography is often the imaging modality of choice near metals, but associated beam hardening and streaking artifacts, dosage issues, and poor soft tissue differentiation inspire the current push to develop methods of MR imaging near metals.

However, the existence of metals in the MR scanner can generate several problems. From a safety standpoint, forces and torques may be induced by the magnetic field on/in metals (37-39), and general RF heating can also occur (40). From an imaging standpoint, the B_1 field and subsequent excitation reliability can be disturbed by RF shielding as RF pulses induce eddy currents in metals (41,42), but the main difficulty is associated with the B_0 field. Metals can cause perturbations to the B_0 field, yielding image artifacts – it is this effect which is of interest to this treatise.

3.2 Artifact Source: Susceptibility Effects

The interaction of the B_0 field in MRI with the magnetic moments of nuclei within the scanner induces variable magnetic responses that depend on the particular magnetic susceptibility of a substance. Macroscopically, magnetization is formed within a material from the interactions of the microscopic fields with the external field. The relationship between the magnetization of a material $M_{material}$ and the external B_0 field is

$$M_{material} = \frac{\chi B_0}{\mu_0} \quad [3.1]$$

where μ_0 is the permeability of a vacuum, and χ is the material's magnetic susceptibility.

Ignoring B_1 and gradient fields, the field in the scanner will be a superposition of the B_0 field and field perturbations caused by a material's magnetization. For example, the summed B field inside a sphere of radius r_0 may be expressed by (39,43)

$$B = B_0 + \frac{2}{3}\mu_0 M_{material} = B_0 \left(1 + \frac{2}{3}\chi\right) \quad [3.2]$$

Outside the sphere, the magnetic field is spatially inhomogeneous and depends on the physical position x, y, z ; for example, the z-component may be expressed as

$$B_z = B_0 \left[1 + \frac{r_0^3 (2z^2 - x^2 - y^2)}{3(x^2 + y^2 + z^2)^{\frac{5}{2}}} \chi \right] \quad [3.3]$$

Materials of more general shape will induce field perturbations that depend on the object's size, shape, and orientation. Sharp edges yield the strongest field perturbations, and the ensuing susceptibility effect (39,44) of shifted spin frequencies leads to strong image artifacts (45,46). Equations [3.2] and [3.3] indicate that

$$\Delta B \propto \chi B_0 \quad [3.4]$$

This relationship and the subsequent susceptibility effect are verified by studies showing that artifacts become more severe with larger B_0 (47) and susceptibility χ (48). Table 3.1 (36) lists some common χ values for metals used in MRI; note the relatively high susceptibility of chromium-cobalt-molybdenum (CrCoMo), the material used in tests throughout this study.

Material	χ [ppm]	Source
Tissue/bone	-10	(49)
Air	0.3	(49)
Titanium	182	(49)
Chromium-cobalt	900	(50)
Chromium-cobalt-molybdenum	1300	(51)
Stainless steel, MR-safe	3000-5000	(49)

Table 3.1 Common material susceptibilities. © Journal of magnetic resonance imaging, 2010, adapted by permission (36).

While most materials exhibit multiple types of magnetic interactions, their overall magnetic response is classified into three general categories. Ferromagnetic materials such as iron, cobalt, nickel, stainless steels, lodestone and gadolinium are characterized by a strong tendency for neighbouring magnetic moments to align with one another and the external field. Susceptibility values are large ($\chi = 10^3 - 10^4$), yielding widespread signal loss artifacts in images. Diamagnetic materials such as mercury, gold, bismuth, copper, silver, lead, water, bone, and some tissue induce magnetic moments that opposes the external field, yielding small and negative susceptibility. Paramagnetic materials such as aluminum, titanium, nonmagnetic stainless steel, mediloy, elgiloy, nitinol, molybdenum, and chromium/nickel alloy steels have randomly oriented magnetic moments that tend to align with the external field, producing moderate susceptibility ($\chi = 10^{-5} - 10^{-3}$).

Metals induce the largest field perturbations and subsequent image artifacts of all materials in MRI. Generally, ferromagnetic materials are unsafe in MRI due to induced forces, and diamagnetism is a relatively weak effect, so the metallic devices of concern in MRI are of the

paramagnetic variety. The CrCoMo implant tested in later chapters represents a paramagnetic material which suffers from particularly strong artifacts due to its relatively high susceptibility.

3.3 Artifact Types

A classification of B_0 inhomogeneity artifacts is depicted pictorially in Figure 3.1.

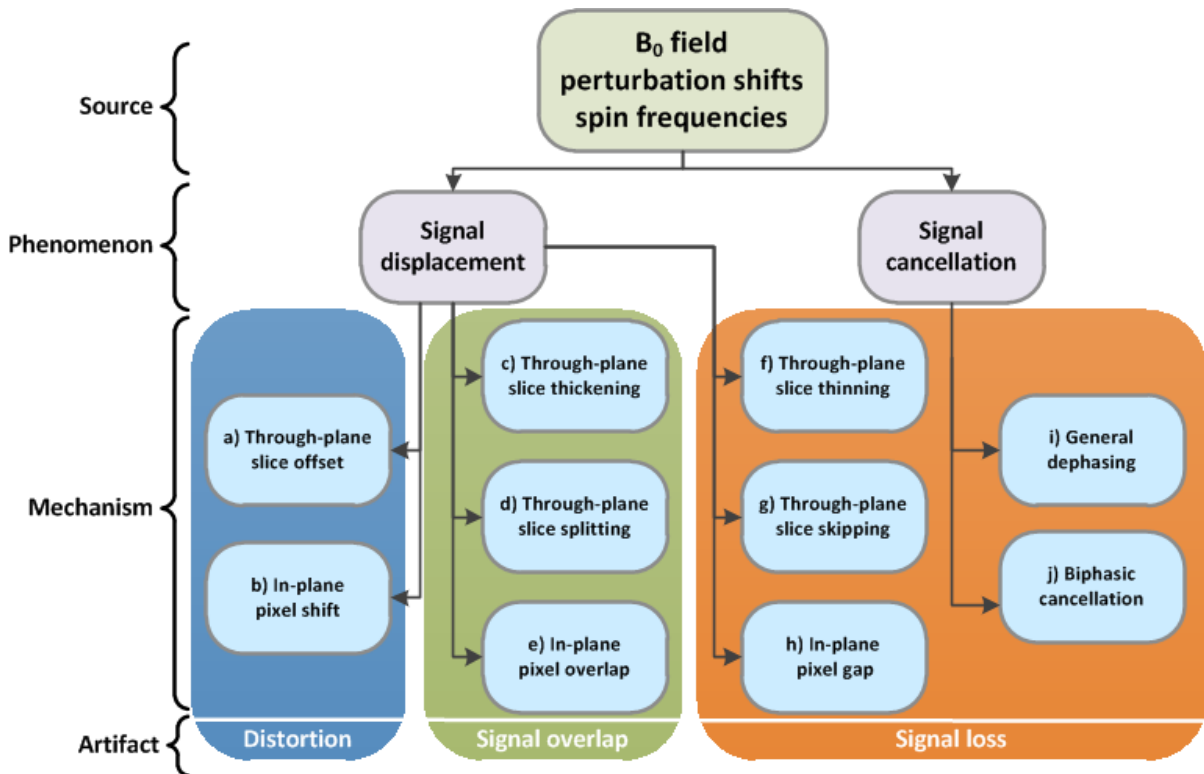


Figure 3.1 B_0 inhomogeneity artifact categorization map. The effects of a source B_0 field perturbation on MR images may be broken down into two phenomena responsible for multiple artifact generating mechanisms. Subsequent artifacts are seen as distortion, signal overlap, and signal loss.

The B_0 field perturbation induces spin frequency variations that can lead to two artifact-causing phenomena: signal cancellation stemming from phase cancellation within voxels, and “in-plane” (in the image plane along the FE x-axis) and “through-plane” (between image slices along the z-axis) signal displacement. These phenomena can in turn result in a variety of mechanisms that generate distortion, signal loss and signal overlap; these artifacts may be visualized in Figure 3.2 from Kaur *et al.* (52).

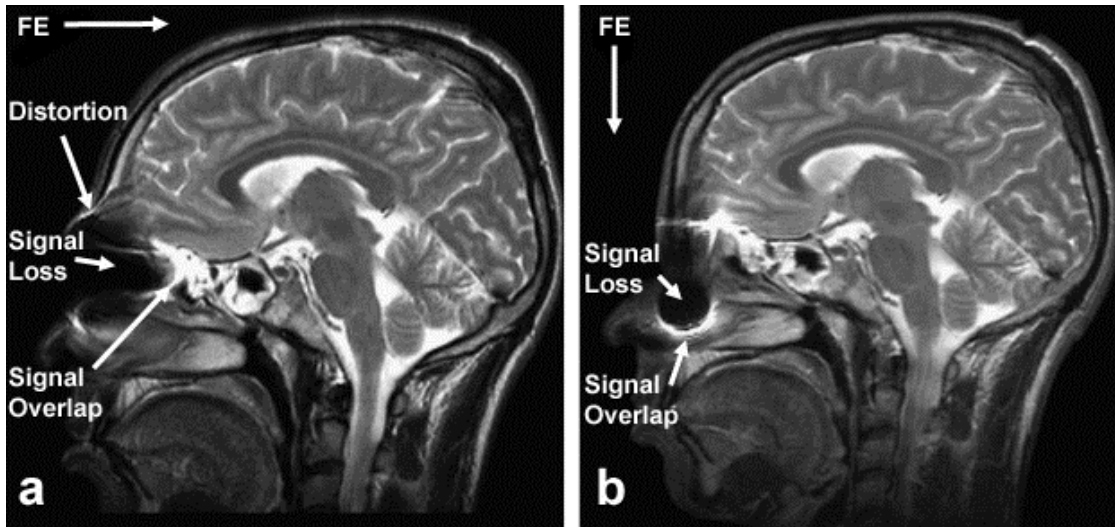


Figure 3.2 Metal flake in the sinus causes artifacts in turbo spin echo brain images. Frequency encoding (FE) direction is a) horizontal and b) vertical. Distortion, signal loss, and signal overlap are indicated. © Radiography, 2007, by permission (52).

The artifacts and their contributing mechanisms as lettered in Figure 3.1 are presently described in turn, although in reality it can be difficult to determine which mechanisms are responsible for each artifact. Signal modulation in bSSFP sequences is discussed separately as it does not strictly conform to any of the artifact types. Chemical shift artifacts may also arise due to non-uniform fat suppression (53).

3.3.1 Distortion

Image distortion stemming from susceptibility effects is relatively common in MRI. Frequency encoded spatial localization hinges on linearly changing spin frequencies, and so frequency shifts generate spatial signal displacement. Phase encoding is resilient to these distortions, which is why 3D imaging is frequently employed throughout this report. Coupling Eq. [3.4] with Eq. [2.5], the FE in-plane pixel shift for a spin subjected to a ΔB field perturbation may be shown to obey the following relationship (39)

$$\Delta x \propto \frac{\chi B_0}{G_x} \quad [3.5]$$

It is evident why many prevalent metal artifact correction techniques described later in this chapter employ high readout bandwidth BW_{RO} , since this corresponds to strong G_x gradients which reduce Δx (54,55). The SS axis suffers from similar through-plane frequency shifts, $\Delta z \propto \chi B_0 / G_z$, but are manifested in a different way. Through plane shifts Δz may be expressed using the Eq. [2.4] expression for the slice thickness d

$$\Delta z \propto \frac{\gamma \chi B_0}{2\pi BW_{RF}} d \quad [3.6]$$

These through-plane frequency shifts cause spin mis-localization, and can result in a) slice offset, c) slice thickening (signal overlap) and f) slice thinning (signal loss), depending on the local Δz value – the next section and the dark grey region of Figure 3.3 further elucidate these artifact mechanisms.

3.3.2 Signal Overlap

Signal overlap is often called “pile-up”, and stems from displaced signal generating spuriously bright regions in images. In-plane pixel shifts defined in Eq. [3.5] can yield e) in-plane signal overlap if signal from disparate locations are mapped to the same target pixel (56). Through-plane Δz frequency shifts can cause c) slice thickening as a broadened range of spins along the slice direction are excited and piled up in an image. The light grey region of Figure 3.3 from Lu *et al.* (57) demonstrates d) through-plane slice splitting, where a field perturbation causes multiple slice locations along the SS axis to have similar precession frequencies, and thus all are excited and overlapped in a 2D image.

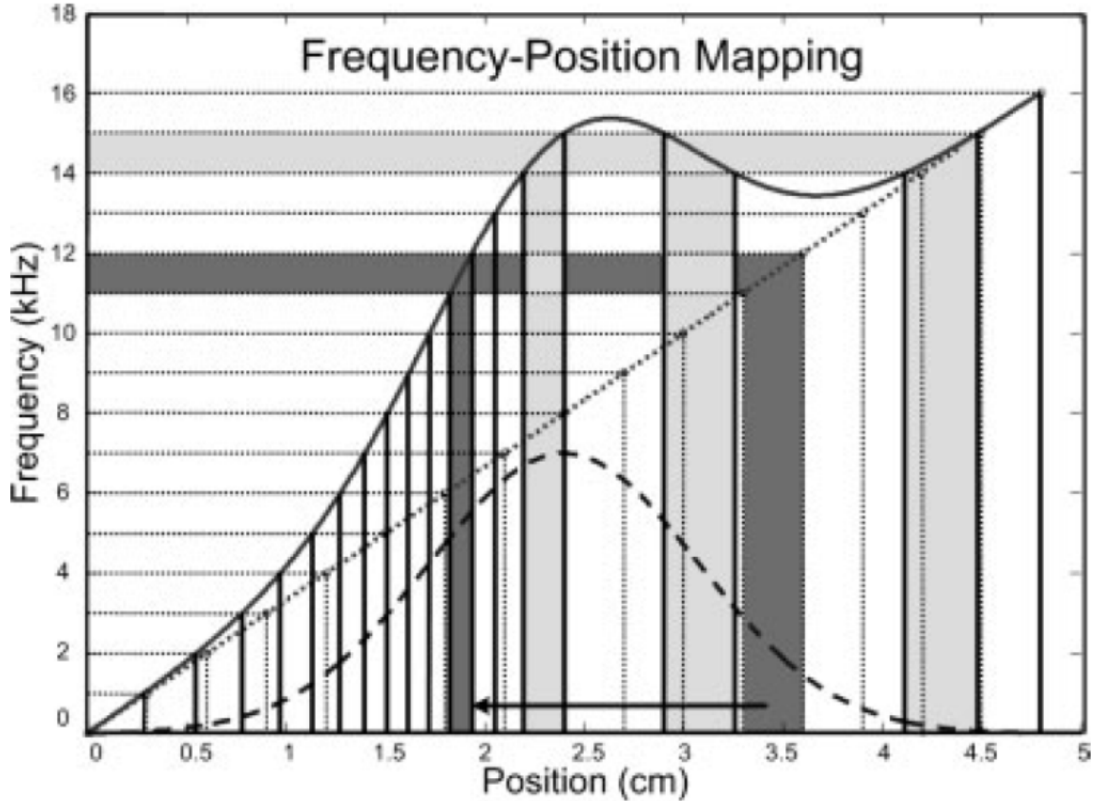


Figure 3.3 Slice selection (SS) with perturbed frequency-position mapping. Field inhomogeneity (dashed line) perturbs the linear SS gradient (dotted line) to yield a nonlinear SS range of spin frequencies (solid line). Dark grey region at ~11.5kHz RF frequency shows slice thinning and offset, and light grey region at ~14.5kHz RF frequency shows slice splitting, thinning, and thickening. © Magnetic Resonance in Medicine, 2009, by permission (57).

3.3.3 Signal Loss

Imaging near metals yields multiple sources of signal loss. Some loss is caused by RF shielding (45,46,48), but much of the dark or dimmed regions in images stem from B_0 sources such as signal displacement. Frequency shifts can cause h) in-plane pixel gap if no signal is mapped to a particular target pixel. The dark grey region of Figure 3.3 illustrates how dimmer signal from f) slice thinning can occur due to through-plane Δz frequency shifts. Figure 3.6 will show that g) slice skipping may occur near metal implants (58) if large field perturbations cause precession frequencies to be beyond the RF excitation bandwidth (59).

Another B_0 source of signal loss is intravoxel signal cancellation. The last chapter discussed how gradient echo signal can be dimmed or completely eliminated when inhomogeneous magnetic fields cause off-resonant phase cancellation within a voxel, or i) general dephasing. Water diffusion in microscopically inhomogeneous fields can also yield dephasing (39). Imaging with bSSFP suffers from a more coherent form of dephasing dubbed j) biphasic cancellation. Spatially periodic dark signal bands manifest wherever the signal's biphasic, or predominately opposed phase magnetization, exists in one voxel and cancels. This becomes a serious problem near metals, where the field inhomogeneity gradient may be strong enough that most voxels' magnetization is biphasic and experience signal cancellation. This mechanism and the signal modulation artifacts described next will be further explored in Chapter 5.

3.3.4 Signal Modulation

Figure 2.10a demonstrated that bSSFP signal experiences periodic signal modulation as a function of off-resonance θ . This variation depends on T_1 , T_2 , and α ; Figure 3.4 shows Bangerter *et al.*'s (60) efficient depiction of this frequency response profile dependence.

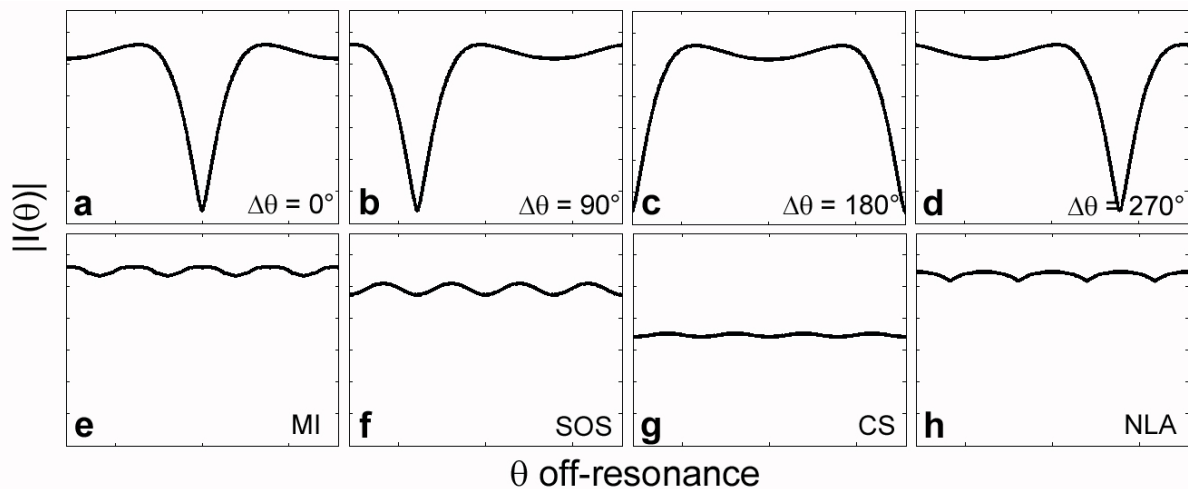


Figure 3.4 bSSFP signal magnitude (above) and phase (below) off-resonance profiles. Magnitude responses are shown for $T_1/T_2 =$ a) 300/150 ms, b) 300/90 ms, and c) 900/90 ms, with flip angle $\alpha = 30^\circ$ (solid lines), 60° (dotted lines), and 90° (dashed lines) for each T_1/T_2 ratio. © Magnetic Resonance in Medicine, 2004, adapted by permission (60).

Beyond the banding discussed in the last section, the bSSFP profiles exhibit general tissue and system parameter-dependent magnitude variability. Observing only the solid magnitude $\alpha = 30^\circ$ lines, at $T_1/T_2 = 900/90\text{ms}$ the response is quite flat and wide in the non-banded regions, while at $T_1/T_2 = 300/150\text{ms}$ and $300/90\text{ms}$ the response in these regions is saddle-shaped. A good example of this modulated signal intensity can be seen in Figure 3.5 from Muir *et al.* (61), where bSSFP images of the eye depict both banding signal drops and variable signal in non-banded regions.

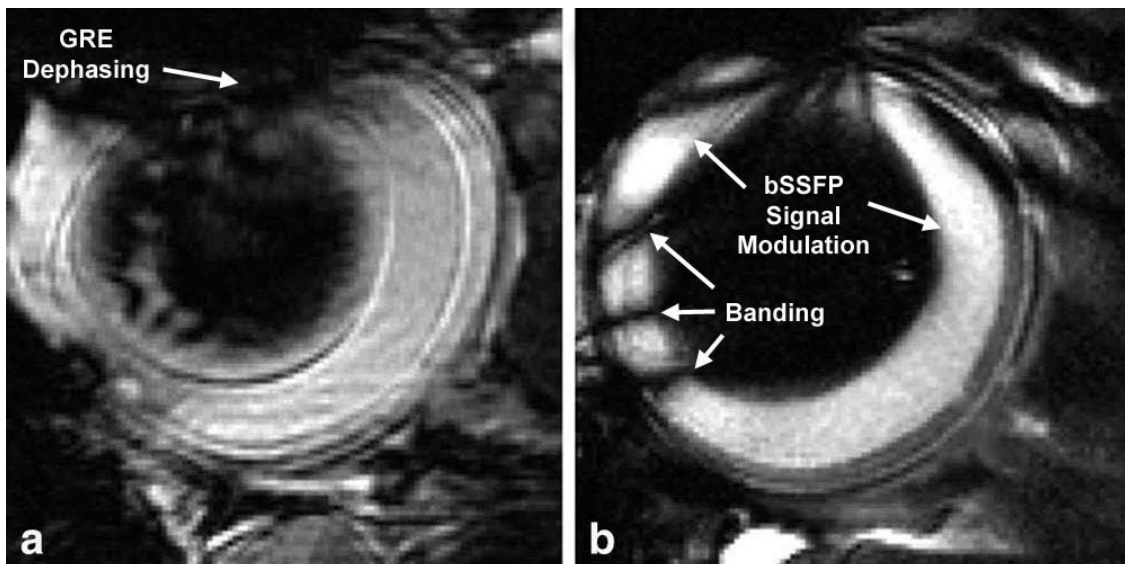


Figure 3.5 bSSFP signal modulation in the eye. a) Dephasing in a gradient echo image of the eye is shown for comparison. b) bSSFP image of an eye shows banding and general signal modulation throughout the retina. © Magnetic Resonance in Medicine, 2011, by permission (61).

3.4 Artifact Correction Techniques

The demand for MR imaging near metals has driven metal artifact correction research. There are various standard clinical strategies that may be implemented on any MR scanner, but they typically only marginally reduce artifacts. Recently, advanced methods that require added scan time to acquire multiple spin-echo images have been developed to correct artifacts. Here most prominent metal artifact correction schemes are outlined.

3.4.1 Standard Clinical Strategies

The MRI system plays a role in the severity of metal artifacts. Earlier, Eq. [3.5] introduced how increased BW_{RO} or G_x is an excellent way to reduce in-plane signal displacement (55), and Eq. [3.6] indicated that increased BW_{RF} can reduce through-plane displacement. Increased gradient amplitude may also be used to reduce voxel size, which can limit distortion and intravoxel dephasing at the expense of increased scan time (62,63). Unfortunately, increased gradients and subsequent imaging bandwidths BW_{RF} and BW_{RO} can reduce image signal-to-noise ratio (SNR) and increase power deposition to the patient (53). Reduced artifacts are also associated with lower B_0 field strength (47,64), but since higher field magnets generally have stronger maximum gradients, decreased field magnets do not necessarily ensure reduced artifacts (65,66).

The chosen pulse sequence and its parameters can also be modified to minimize artifacts. Fast spin echo imaging and minimization of TE is often employed to reduce dephasing and other artifacts (11,67,68). Slab selective 3D imaging applies two dimensions of phase encoding to minimize artifacts, although Eq. [3.6] indicates that large slabs will suffer from large through-plane signal displacement. Non-selective 3D imaging without a z-gradient can circumvent these complications. Figure 3.2 demonstrated the relationship between artifacts and the FE direction. It is helpful to orient the long axis of a metal parallel to the FE direction (69) and the B_0 field (65,70) in order to reduce susceptibility artifacts.

Specific steps are typically taken to address bSSFP signal modulation and chemical shift effects. Clinical bSSFP imaging phase cycles the RF by $\Delta\theta = \pi$ to shift the bands off-resonance, and uses powerful gradients to limit the TR during which off-resonant phase may accumulate. Fat suppression in inhomogeneous B_0 fields can be achieved with a Short TI Inversion Recovery sequence (71), which is independent of resonant frequency and thus performs better than other techniques near metals (53).

3.4.2 B_0 and Susceptibility Mapping

Much of the early inhomogeneity artifact correction work revolved around remapping displaced signal using magnetic field estimates (72). A priori estimations (56), phase mapping (73,74), and two-image acquisitions with variable TE (75) or gradients (76) have all been employed to generate field maps. Unfortunately, these techniques are often unable to map the full range of inhomogeneity near metals, and prior knowledge and numerical analysis are frequently necessary. Susceptibility mapping employs iterative and convolution-based methods to calculate field maps from susceptibility models (77,78). However, this method requires a three dimensional map of the susceptibility variation and experiences difficulties near susceptibility interfaces (79).

3.4.3 Single Point Imaging

While prohibitively time-consuming, it is possible to do away with frequency encoding entirely and acquire MR data with phase encoding along all three imaging axes to avoid signal displacement artifacts (80-82). Efforts have been made to speed up the acquisition of these techniques (72,83-85), but scan time reductions come at the expense of lessened artifact correction. The technique is also typically non-selective, and thus the entire field of view (FOV) must be imaged to avoid aliasing artifacts. An interesting combination of single point imaging and field mapping adds PE gradients along both in-plane directions; the degree of image blurring may then be measured to permit distortion correction (86).

3.4.4 UTE

Ultra-short TE (UTE) applications (87,88) are currently being considered for B_0 inhomogeneity artifact mitigation, as these techniques experience minimal artifacts due to the short time available for deleterious phase accumulation (89,90). UTE employs a hard pulse, high BW_{RF} and BW_{RO} , and directly samples the FID during the gradient ramp. The technique has been combined with other techniques that exhibit more thorough metal artifact correction (91,92) with moderate success. However, the scheme essentially only recovers

signal lost by T_2^* dephasing. Since radial imaging is more sensitive to frequency offsets than standard Cartesian sampling approaches, residual distortion and blurring often remain. It can also suffer from eddy currents and band artifacts due to the rapid gradient switching (36).

3.4.5 VAT and MARS

View angle tilting (VAT) mitigates FE distortion artifacts by employing a SS compensation gradient concurrent with the FE readout gradient to tilt the slice angle in SE imaging (93). VAT was first demonstrated on images near metals in 1997 (94), and the metal artifact reduction sequence (MARS) later strengthened gradients and increased BW_{RF} to further reduce distortion (95-97). While it can considerably reduce in-plane artifacts, it does not correct through-plane artifacts, and residual blur due to slice profile modulation must be addressed (98).

3.4.6 SEMAC

Using elements of gradient echo slice excitation profile imaging (99) to address through-plane artifacts and VAT to address in-plane artifacts, SEPI-VAT (100) corrects a given slice by applying an FT to 16 variably z-phase encoded VAT images. SEMAC, or slice encoding for metal artifact correction (57), modifies SEPI-VAT with increased gradient strength; after an FT, spatial spin positioning, and summing of multiple slices on a voxel-by-voxel basis, through-plane artifacts are reduced. The BW_{RF} and BW_{RO} are adjusted to achieve the desired trade-off between residual in-plane and through-plane artifacts. While the ~15-20 minute scan time cost for this technique has inspired acceleration attempts (101), it can nevertheless achieve near-comprehensive metal artifact correction.

3.4.7 MAVRIC

The BW_{RF} can miss spins that are outside the excitation frequency range, yielding signal loss near metals. Heindel *et al.* showed in Figure 3.6 that by applying an RF pulse of shifted central frequency, the “lost” spins may be excited (59).

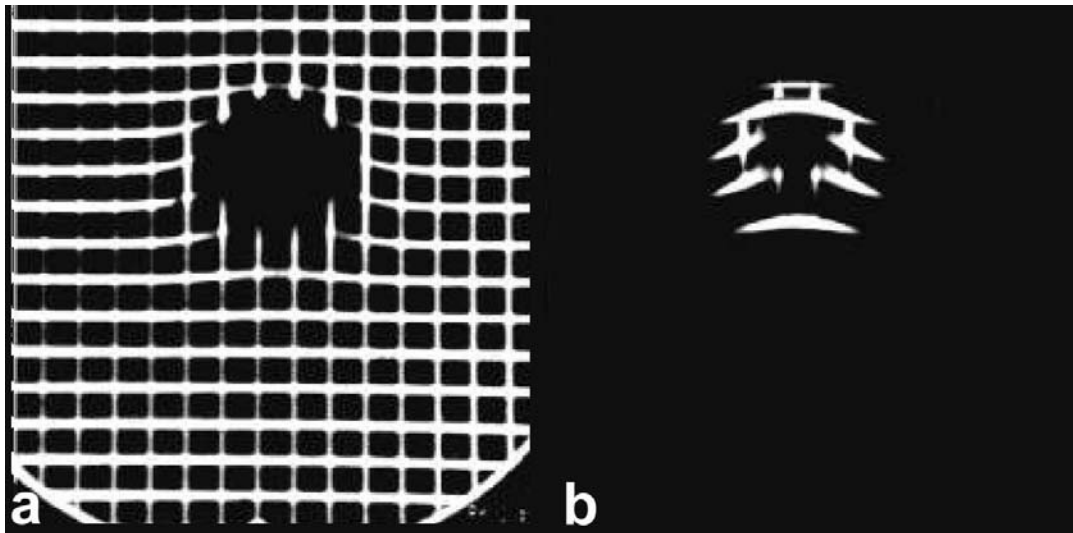


Figure 3.6 Through-plane slice skipping / missed excitation. a) Surgical instrument metal particles cause signal loss in a grid phantom. b) Shifting the RF pulse frequency permits signal loss recovery. © Journal of Computer Assisted Tomography, 1986, adapted by permission (59).

MAVRIC, or multi-acquisition variable-resonance image combination (102) builds upon this work by performing a sum of squares combination of several images acquired at variable central RF frequencies. Non-selective 3D imaging is employed to avoid slab selection artifacts, and scan time is minimized by reducing the FOV for acquisitions that only excite spins near the metal. MAVRIC suffers from residual artifacts stemming from image combination and the disruption of the Fourier encoding process by strong regional inhomogeneity gradients (36). Like SEMAC, this method requires significant scan time in excess of 20 minutes for a standard scan, but provides thorough artifact correction.

3.4.8 Low Field Techniques

Since susceptibility artifacts scale with field strength (47,64), prepolarized MRI has been developed to generate images at weaker fields (103). It employs two electromagnets in place of the standard single superconducting magnet; the first magnet polarizes the sample with a strong but less homogeneous field, and as it is ramped down a weaker more homogeneous magnet is turned on for low field imaging. The method employs a non-selective RF pulse, low BW_{RO} , and weak field to achieve in-plane artifact reduction. Prepolarized MRI offers

good signal near metals, but requires a specialized system that is not readily available in clinical scenarios (36).

3.4.9 Variable Bandwidth Excitation / Refocusing

A recent method employed for metal artifact reduction is the use of different BW_{RF} for excitation and refocusing pulses (104). This prevents refocusing of off-resonant spins that arise from variable slice displacement of the excitation and refocusing pulses. Unfortunately, some signal is lost in the process, and subsequent saturation between slices can introduce slice gaps (53).

3.4.10 Multi-Acquisition bSSFP Techniques

The banded signal loss and general signal modulation in bSSFP imaging discussed in sections 2.5.3 and 3.3.4 may be reduced using multi-acquisition techniques. Shifting the MR imaging frequency (105) or RF phase cycling (106,107) can shift the bSSFP frequency response profile; Figure 3.7a-d depicts this mechanism for a range of $\Delta\theta$ phase cycles.

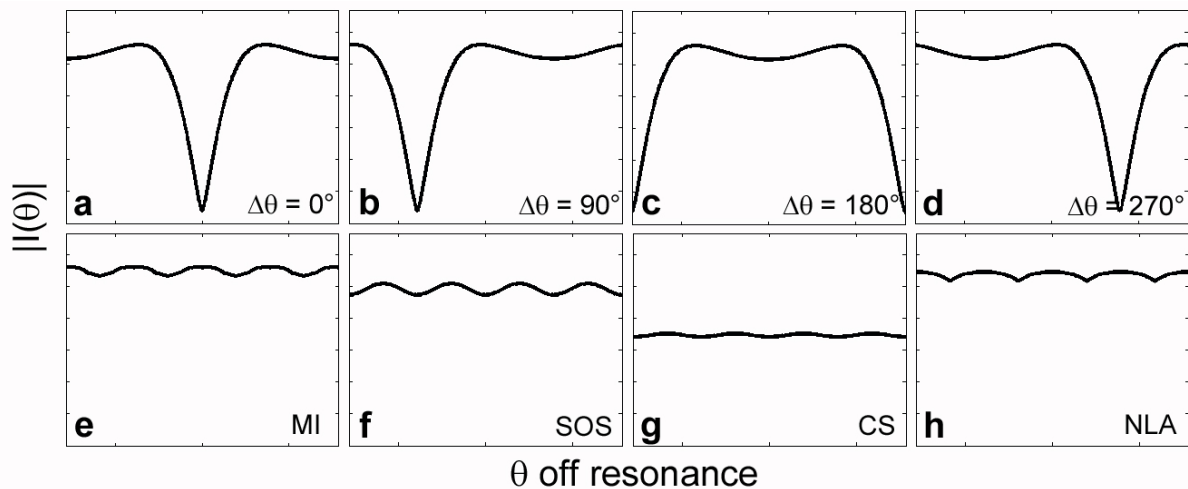


Figure 3.7 Phase-cycled bSSFP frequency response profiles and combination schemes. Using $\alpha = 40^\circ$, $T_1/T_2 = 300/90$ ms, and $TR = 4.2$ ms, $\Delta\theta =$ a) 0° b) 90° , c) 180° , and d) 270° phase-cycled bSSFP magnitude data are simulated, and e) maximum intensity, f) sum of squares, g) complex sum, and h) non-linear average reconstructions are formed.

Since no two relatively phase-cycled images should have bands at the same off-resonant phase values, combining acquisitions can ameliorate banding. The ability to reduce bands will depend on the technique employed, the tissue/system parameters (T_1 , T_2 , and α), and the number N of relatively phase-cycled images. Although bands disappear entirely as $N \rightarrow \infty$, most combination techniques only reduce bands while simultaneously increasing their spatial frequency N -fold relative to any one bSSFP magnitude image. The new techniques described in Chapter 5 will alleviate these difficulties by exactly calculating a characteristic bSSFP signal value, as opposed to arbitrarily combining relatively phase-cycled bSSFP images.

Various multi-acquisition pixelwise image combination strategies have been proposed. Maximum intensity (MI) uses the largest magnitude from the component images in the final image (108). The best band reduction is achieved with the complex sum (CS), which averages the complex data and takes the magnitude (105,107) to achieve smoothed signal. As $N \rightarrow \infty$, the CS approaches $\langle I \rangle$, the centre-of-mass of the bSSFP signal ellipse as defined by Eq. [2.24]. The sum of squares (SOS) technique takes the sum of the squared image values, and finds the square root for appropriate scaling (60). The nonlinear average (NLA) discards the lowest magnitude signal and averages the rest (109).

Expressions for the MI, CS, and SOS are given in Eqs. [3.7]-[3.9], where $I_i(\theta)$ is a given complex bSSFP pixel value for image i , and simulated reconstructions are given in Figure 3.7e-h. It is evident that with $N = 4$ images, all techniques exhibit residual banding artifacts and variable signal strength.

$$\text{MI} = \max_{i=1..N} (|I_i(\theta)|) \quad [3.7]$$

$$\text{CS} = \left| \sum_{i=1}^N I_i(\theta) \right| \quad [3.8]$$

$$\text{SOS} = \sqrt{\sum_{i=1}^N |I_i(\theta)|^2} \quad [3.9]$$

3.4.11 Which Correction Technique to Choose?

There are multiple metal artifact correction schemes, but the best choice is not immediately obvious. Methods such as Single Point Imaging, MAVRIC, and SEMAC provide strong artifact correction, but take significant scan time to do so. Techniques such as UTE and MARS take little time, but are by no means mature in their artifact correction abilities. Current methods of debanding bSSFP signal are not nearly robust enough to inspire the use of bSSFP imaging near metals where strong banding is prevalent. It is apparent that the best choice depends on available hardware and software, time constraints, and desired image clarity. It is also evident that fast techniques with strong artifact correction are not currently available, which has inspired the current research.

3.5 Summary

The effects of metals on the magnetic field and spin precession in MRI were described to characterize the prominent source of MRI metal artifacts. The subsequent phenomena and mechanisms of artifact generation were discussed, and delineated in terms of the different image artifact types to which they contribute. Finally, many artifact correction schemes were described that purport to facilitate diagnostic imaging near metals. Unfortunately, the temporal demands of image-guided surgery and respiratory, cardiac, and other motion-sensitive clinical imaging applications require expedited procedures. This overview leads to an appreciation for this study's search for ways to image near metals in short scan time.

Chapter 4: B_0 Inhomogeneity Artifact Correction with 3D-PLACE

This chapter introduces a novel technique for imaging near metals in moderate scan time. The PLACE technique, or phase labeling for additional coordinate encoding (110), is applied in concert with 3D imaging to correct distortion near metals using two spin-echo images (111). The possibility of generalizing the technique to a multiple layer model for correction of signal loss and overlap artifacts is also explored.

4.1 3D-PLACE Distortion Correction

PLACE was originally implemented to eliminate ghosting and distortion along the PE direction in Echo Planar Imaging (110,112). The distortion is caused by field inhomogeneity-induced phase accumulation; as outlined in section 3.3.1, this problem also occurs along the FE axis when imaging near metals with spin-echo sequences. Here two TSE images are acquired with variable phase gradients applied along the FE direction to correct in-plane distortions stemming from susceptibility effects near metals. 3D MRI is added to reduce through-plane signal displacement within the slab via z-phase encoding; this metal artifact correction technique is thus dubbed 3D-PLACE (111).

4.1.1 Background

Understanding of the 3D-PLACE method requires an introduction to the fundamentals of PLACE. One TSE image is acquired in a regular fashion, and a second image is acquired with a phase encoding gradient applied prior to data acquisition along the FE axis, henceforth called the “blip”, or “PLACE gradient”. These two pulse sequences are shown in Figure 4.1. The TSE sequence requires gradient balancing from pulse to pulse, so an additional PLACE gradient of inverted polarity is applied along the FE axis following the readout gradient.

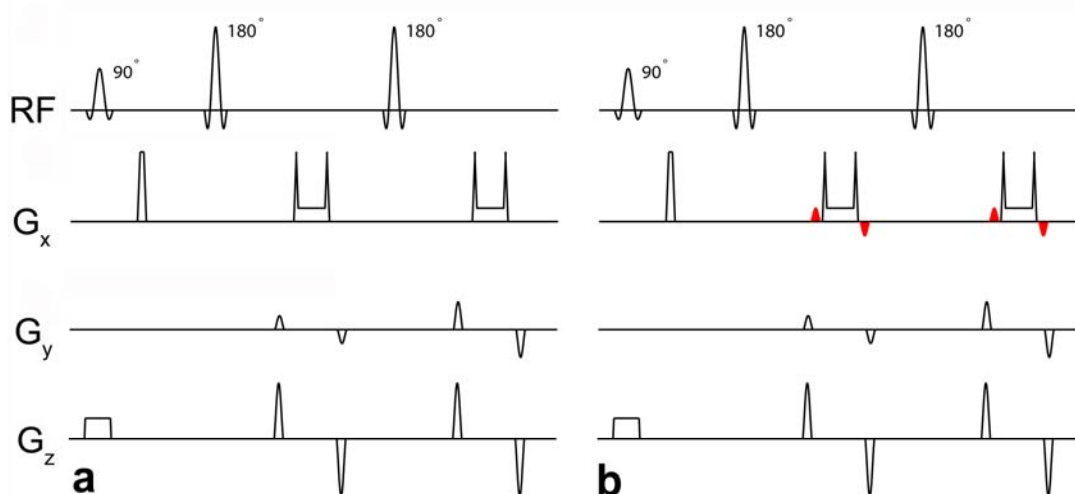


Figure 4.1 Turbo spin echo (TSE) PLACE pulse sequence timing diagrams. a) 1st PLACE image is a basic TSE sequence. b) 2nd PLACE image includes additional phase gradients applied on the FE G_x axis in red, alternated to preserve spin-echo refocusing.

The PLACE gradient shifts the k-space data along the G_x direction, which according to the Fourier shift theorem (113) applies a linear phase ramp across the FE FOV of the reciprocal space. Consider the phase prior to the field-perturbation-dependent imaging procedure. Figure 4.2 depicts this object space; the first, unramped object phase O_1 has no PLACE gradient, while the second object O_2 has a PLACE gradient-induced phase ramp across the FE FOV.

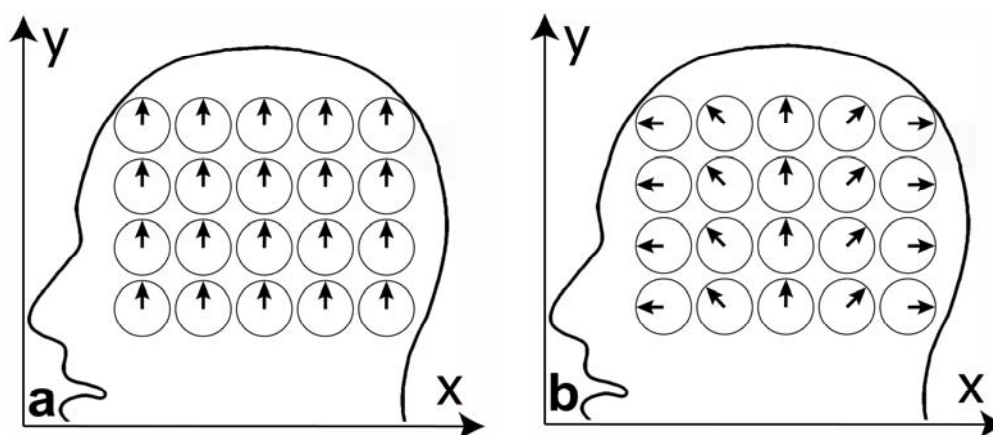


Figure 4.2 The effects of the PLACE gradient on true object phase. a) The 1st object O_1 has oversimplified, aligned phase. b) The 2nd object O_2 has a relative phase ramp applied across the x -axis field of view.

The key idea is that the phase ramp is linear and applied to the original object O_2 prior to readout and subsequent signal detection. A field perturbation will add equivalent phase to each object in the generation of respective images I_1 and I_2 . Figure 4.3 shows phase row plots Φ_1 and Φ_2 from one y -value of images of I_1 and I_2 as a function of x -position. While the perturbation affects both images, the phase difference $\Delta\Phi$ of the two images will be linear and independent of the perturbation.

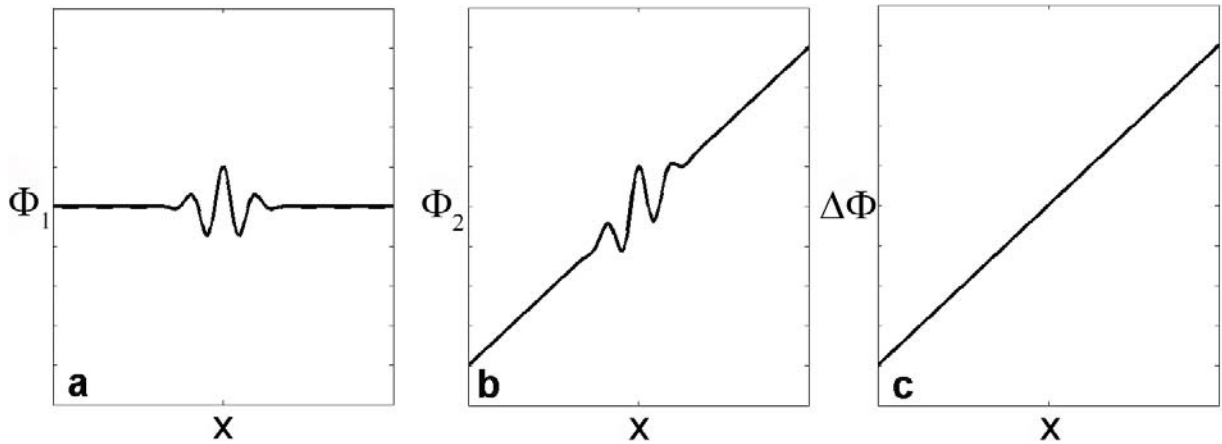


Figure 4.3 The phase difference of PLACE images. Objects O_1 and O_2 of Figure 4.2 in the presence of a field perturbation result in images I_1 and I_2 ; a) and b) plot the phase Φ_1 and Φ_2 from a row of pixels from each respective image. c) The $\Delta\Phi = \Phi_2 - \Phi_1$ phase difference is independent of the perturbation.

Consider a scenario where the PLACE gradient area generates exactly one 2π phase twist across the FE FOV of O_2 . The phase difference of complex I_1 and I_2 may be computed via their complex conjugate product

$$I_1 I_2^* = |I_1 I_2| e^{\frac{i2\pi x}{\text{FOV}}} \quad \frac{-\text{FOV}}{2} \leq x \leq \frac{\text{FOV}}{2} \quad [4.1]$$

$|I_1|$ and $|I_2|$ are the nearly identical signal magnitudes of the two images, the exponential represents the added 2π phase twist across the FE FOV caused by the PLACE gradient, and x represents the true FE coordinate measured from the magnet isocentre. Only the magnitudes remain of the original images since the complex conjugate product cancels their distorted phase, which should be equal since the added phase ramp is assumed to be independent of the sample-induced field inhomogeneity.

The true signal position x is then easily found

$$x = \frac{\text{FOV}}{2\pi} \text{ATAN2}[\text{Im}(I_1 I_2^*), \text{Re}(I_1 I_2^*)] \quad [4.2]$$

where $\text{ATAN2}[\text{Im}(I_1 I_2^*), \text{Re}(I_1 I_2^*)]$ finds the argument or phase of $I_1 I_2^*$. If this procedure is applied pixel-by-pixel, x is a map of true target pixel locations that may be used to send pixels in a distorted magnitude image to their true target locations.

4.1.2 Methods

Figure 4.4 shows the phantom built for this study: a Lego™ (Billund, Denmark) structure is constructed around a Zimmer™ (Warsaw, IN) ASTM F75 CrCoMo alloy hip prosthesis and placed in a bottle of water with sponges positioned for stabilization.

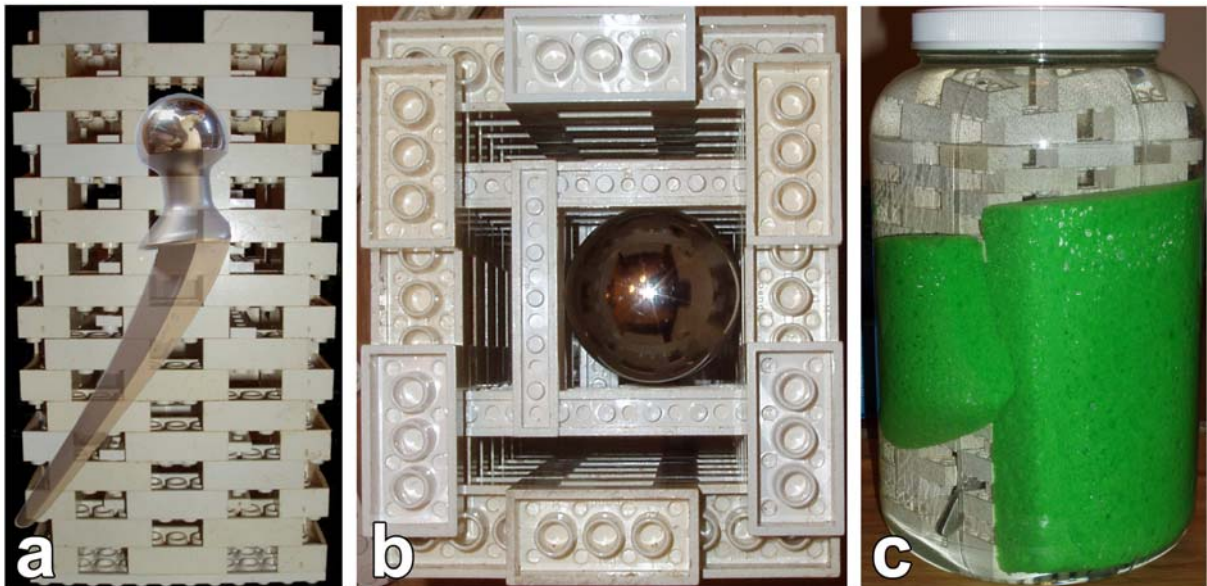


Figure 4.4 Chromium-cobalt-molybdenum hip prosthesis/Lego phantom. a) Profile view of the Lego structure with Zimmer™ (Warsaw, IN) ASTM F75 implant overlaid. b) View from above the implant in the Lego building. c) The entire structure is placed in a bottle of water with sponges for stabilization.

The phantom was imaged using a body coil in a 1.5T Siemens Avanto scanner. Each sagittal image set required 4 minutes and 20 seconds scan time, and employed $\text{TR/TE} = 300/11$ ms, $BW_{RO} = 33$ kHz, 256/256/12 matrix size, and 1.17/1.17/5 mm voxel size along frequency/

phase/slice directions. Axial image sets were identical except that the PE size was 152 pixels, and each required 2 minutes and 38 seconds scan time. Two complex images were acquired using a 3D TSE sequence, and differed only by the PLACE gradient applied along the FE axis of the 2nd image acquisition as discussed in the last section.

The earlier discussion involved only $m = 1 \times 2\pi$ phase twist across the FE FOV. PLACE achieves greater correction resolution if the in-plane pixel displacement occupies a greater proportion of the 2π phase twist spatial range. Since distortions do not typically extend across the entire FOV, larger PLACE gradients should be employed since they correspond to a shortened 2π phase twist range. However, if the pixel shifts are greater than the 2π phase twist range, the remapping procedure can incorrectly calculate the true pixel location and send pixels across phase wraps. For example, if a PLACE gradient is employed that yields a $-5\pi \rightarrow 5\pi$ phase ramp across the FOV, any distortions exceeding FOV/5 could potentially be aliased to an incorrect subregion of the image.

Equation [2.6] gives the phase from a rectangular phase encoding gradient of area $G_y \cdot T$, thus the PLACE phase encoding gradient $area_{blip}$ is given by

$$area_{blip} = \frac{\Delta\Phi(\Delta x)}{\gamma\Delta x} \quad [4.3]$$

where $\Delta\Phi(\Delta x)$ is the amount of accumulated phase stemming from the blip over a distance Δx . The gradient area corresponding to $m \times 2\pi$ phase twists across the FOV is thus

$$area_{blip} = \frac{2\pi m}{\gamma\text{FOV}} \quad [4.4]$$

Figure 4.5 shows PLACE corrections for PLACE gradients with $m = 1, 2, 5, 10,$ and $15 \times 2\pi$ phase twists across the FE FOV. Larger ramps yield better distortion correction resolution, until $m = 15$ where significant aliasing artifacts occur. A conservative value should be chosen to avoid aliasing, since it is not feasible to test various ramp strengths for every imaging procedure. Further experiments balanced performance and signal wrap avoidance

by employing an $m = 5$ equivalent PLACE gradient, which corresponds a $-5\pi \rightarrow 5\pi$ phase ramp across the FOV.

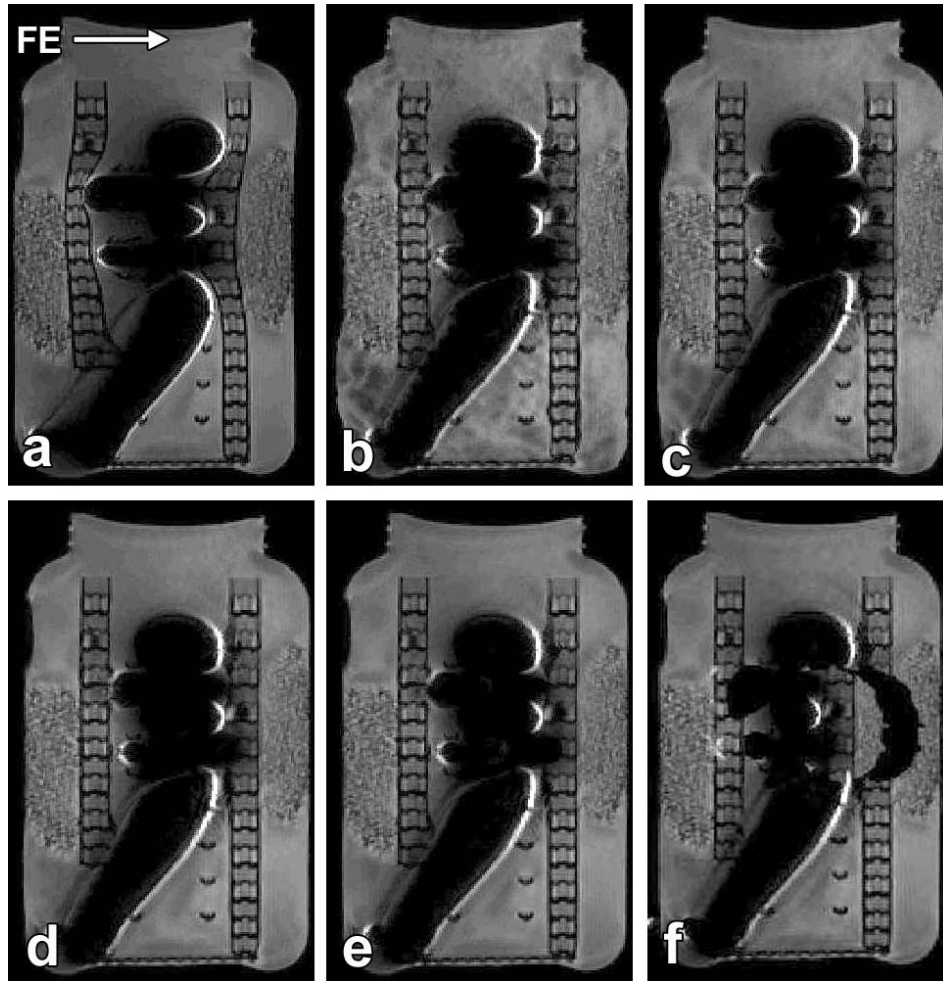


Figure 4.5 CrCoMo/Lego phantom PLACE corrections using variable phase ramps. a) Turbo spin echo magnitude image. PLACE corrections use b) 1, c) 2, d) 5, e) 10, and f) 15 $\times 2\pi$ phase twists across the FE FOVs of their position maps.

Stretching and squeezing distorted data into disparate pixel ranges can result in crack and pile-up errors respectively. These problems are resolved by processing the $I_1 I_2^*$ complex data in two ways. 1) The original computation of Eq. [4.2] generates a map indicating the correct pixel locations. By applying a opposing phase ramp to $I_1 I_2^*$ that exactly compensates the existing phase ramp in both strength and direction, Eq. [4.2] generates a flatter “displacement map” with less noise influence; this map details the required pixel displacements that yield an

undistorted image (110). 2) The complex data is expanded and smoothed to permit sub-pixel data interpolation that avoids spurious intensity variations.

The flattened, expanded and smoothed $I_1 I_2^*$ complex data is input into Eq.[4.2] to obtain an expanded and smoothed pixel displacement map. Mapping is then achieved on the average magnitude of the two acquired complex images, and the result is re-binned to its original size. The final image is distortion-free, with no crack or pile-up artifacts.

4.1.3 Results

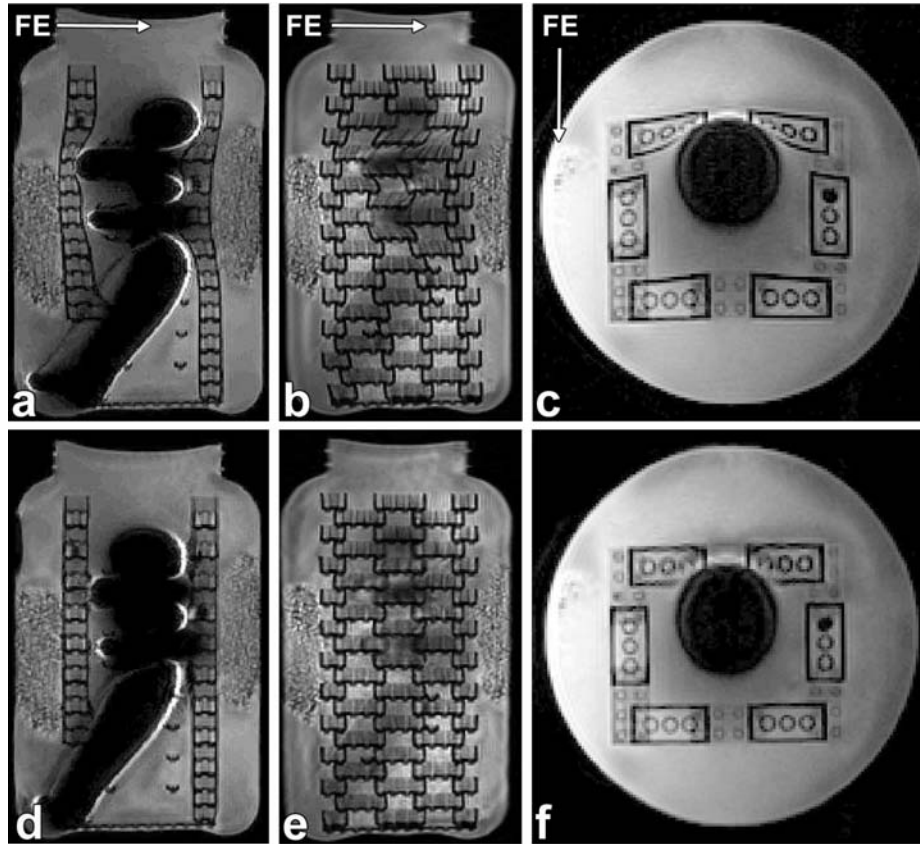


Figure 4.6 Turbo spin echo (TSE) phantom images and their PLACE corrections. a), b) Two different sagittal TSE and c) one axial TSE slice magnitude averages. d), e) Sagittal and f) axial PLACE corrections.

Figure 4.6 depicts one axial and two sagittal images of the CrCoMo/Lego phantom formed from averages of the two acquired TSE images required for PLACE, and their corresponding 3D-PLACE images with distortion corrected. The Lego walls are straightened and display

their expected shape, but signal overlap and loss remain. Signal loss is also more noticeable in regions where the implant has sharper edges, confirming previously discussed results from the literature (45,46).

4.1.4 Discussion

The 3D-PLACE technique eliminates FE distortion stemming from metals in spin-echo images. It is time efficient and simple to execute, requiring only twice the scan time (~5-9 minutes) as would be employed by VAT or MARS, which acquire one SE image. Implementation only requires the addition of PLACE gradients to the pulse sequence, and phase unwrapping is unnecessary in the pixel mapping process if PLACE gradients are chosen carefully.

This technique shows distinct advantages over similar distortion correction techniques. Yamamoto *et al.* (75) generated a phase map for distortion correction from two images acquired at variable TE, which will depend not only on field inhomogeneity but also other effects influenced by TE variations such as eddy currents, T_2 relaxation, and concomitant fields. Chang *et al.* (76) acquired two images with relatively varied readout gradients to reduce distortion, but required numerical analysis and exhibited success only with fiduciary marking or realizable boundary conditions. PLACE's use of added phase gradients along the FE axis circumvent these complications by employing an analytical solution, maintaining sequence timing, and not requiring reference information.

Useful applications of the described method include any scenario where correct spatial positioning is a priority, and image distortion is intolerable. Image-guided radiation therapy is a good example, where image distortion could cause clinicians to erroneously prescribe radiation treatment to healthy tissue. Image guided surgery would also benefit greatly from this imaging technique, if 3D-PLACE could be executed faster and with corrected signal loss and overlap.

Residual signal loss and overlap are the primary limitations of 3D-PLACE. Through-plane components of these artifacts may occur due to the use of slab selection. These problems are shared by techniques such as VAT and MARS, but are largely circumvented by MAVRIC and SEMAC. In-plane signal displacement could also account for signal loss and overlap if the range of frequencies across a pixel due to field inhomogeneity is on the order of the pixel bandwidth BW_{RO}/N_x , where N_x is the number of pixels across the FE FOV. Another limitation of 3D-PLACE is the possibility of aliasing in the PLACE reconstruction if the PLACE gradients are too strong relative to the inhomogeneity gradient.

As an alternative to conservatively setting the PLACE gradient strength to avoid aliasing, gradient strength can be set in a manner similar to the Anti-Aliasing Acquisition (114) technique. This method was originally employed to avert aliasing in velocity encoding. One image would be acquired with a weak phase ramp, yielding poor performance but no aliasing. A second image would be acquired with a strong phase ramp, yielding high performance but potential aliasing. The two datasets could then be suitably combined to achieve good distortion correction without aliasing.

In conclusion, the 3D-PLACE technique can be very useful for removing distortion from images with magnetic field inhomogeneity. It typically takes less than 10 minutes, but does not correct signal loss and overlap. Clinical imaging that requires predictable signal close to metals is thus in need of a more comprehensive solution.

4.2 Multi-Layer 3D-PLACE for Correcting Signal Overlap

3D-PLACE has thus far only considered single layer in-plane pixel shifts; the generalization of PLACE to a multi-layered model could permit correction of in-plane pixel overlap. Once 3D-PLACE had been perfected, numerous variations of multi-layer PLACE were tested for their ability to correct in-plane signal overlap. Here a skeleton framework of a two-layer methodology is presented, indicating that while it may be possible to achieve more comprehensive artifact correction near metals in this manner, much work is needed for successful application.

4.2.1 Theory

Section 3.3.2 details the principles governing in-plane signal overlap near metals in MR images. If a field perturbation causes the same magnetic field to exist in two or more separate sample locations along the frequency encoded direction, complex signal A_j from these locations x_j may be mapped to the same target pixel, yielding a complex summed pixel signal I :

$$I = \sum_{j=1}^L A_j \quad [4.5]$$

where L is the total number of source locations, or layers, mapped to the target pixel.

Phase labeling via the PLACE technique adds additional phase to the original A_j source intensities. Any given pixel in a final image I may then be expressed as

$$I = \sum_{j=1}^L A_j e^{i \frac{2\pi m}{\text{FOV}} x_j} \quad [4.6]$$

where the phase exponential is similar to Eq. [4.1] save for the generalization to $m \times 2\pi$ twists across the FOV.

The goal is to determine the source signals A_j and their original locations x_j . This amounts to an inverse problem, requiring sufficient unique image equations for tractability. Different phase gradient applications m_k can be used to generate sufficient images I_k to resolve all L overlapped layers in a given pixel.

The PLACE formalism derived in section 4.1 assumes only $L = 1$ layer in a given pixel, and thus may be called PLACE-1L. Only two instances of m_k were needed to find the two variables A_1 and x_1 ; say $m_1 = 0$ and $m_2 = 1$

$$I_1 = A_1 \tag{4.7}$$

$$I_2 = A_1 e^{i \frac{2\pi}{\text{FOV}} x_1}$$

This simplifies to Eq. [4.2] when solving for x_1 .

However, if two pixels with signals A_1 and A_2 located at x_1 and x_2 respectively are mapped to a target pixel, an analytical solution will require four images to resolve them. The system may be expressed

$$\begin{bmatrix} P_1^{m_1} & P_2^{m_1} \\ P_1^{m_2} & P_2^{m_2} \\ P_1^{m_3} & P_2^{m_3} \\ P_1^{m_4} & P_2^{m_4} \end{bmatrix} \cdot \begin{bmatrix} A_1 \\ A_2 \end{bmatrix} = \begin{bmatrix} I_1 \\ I_2 \\ I_3 \\ I_4 \end{bmatrix} \tag{4.8}$$

$$\text{where } P_j = e^{i \frac{2\pi}{\text{FOV}} x_j} \tag{4.9}$$

If the values $m_1 = 0$, $m_2 = 1$, $m_3 = 2$, and $m_4 = 3$ are employed, the images will have (0, 1, 2, 3) $\times 2\pi$ phase twists across their respective FE FOVs. The unknowns P_1 , P_2 , A_1 and A_2 may then be solved for in terms of image values I_1 , I_2 , I_3 and I_4 :

$$P_{\frac{1}{2}} = \frac{I_1 I_4 - I_2 I_3}{2(I_1 I_3 - I_2^2)} \pm \sqrt{\left(\frac{I_1 I_4 - I_2 I_3}{2(I_1 I_3 - I_2^2)} \right)^2 - \frac{I_2 I_4 - I_3^2}{I_1 I_3 - I_2^2}} \tag{4.10}$$

$$A_{\frac{1}{2}} = \frac{I_1}{2} \mp \frac{I_1^2 I_4 - 3I_1 I_2 I_3 + 2I_2^3}{4\sqrt{(I_1 I_4 - I_2 I_3)^2 / 4 - (I_1 I_3 - I_2^2)(I_2 I_4 - I_3^2)}} \tag{4.11}$$

This derivation was verified with Maple™. The two complex source signals A_1 and A_2 may then be remapped to their true positions x_1 and x_2 , found from the phasors P_1 and P_2 in a manner similar to Eq. [4.2]

$$x_j = \frac{\text{FOV}}{2\pi} \cdot \text{ARG}(P_j) \quad [4.12]$$

Given the assumption of a two layer model $L = 2$, this solution is coined PLACE-2L.

4.2.2 Simulations

Figure 4.7 demonstrates a composite PLACE 1L/2L solution for a partially overlapped and phase ramped simulated image set. Phase twists of $m = (0, 1, 2, 3) \times 2\pi$ were applied horizontally across the FOV of four copies of a simulated half-square/half-circle object. Each of these four complex objects were manually overlapped on themselves to generate I_1 , I_2 , I_3 and I_4 images as would be acquired on a scanner.

Overlapped pixels have signal given by the complex sum of all contributing spin locations, with pixel magnitude affected by the degree of phase interference. If phase of the different spin locations is altered, the degree of phase interference should also generally change. Since variable phase ramps are applied along the same dimension that signal is overlapped in the noiseless simulation, an absolute magnitude difference of any two of I_1 , I_2 , I_3 and I_4 is only non-zero in overlap regions due to phase interference. Here PLACE-2L is applied by inputting the overlap image regions pixelwise into Eqs. [4.10]-[4.12] and mapping the output A_1 and A_2 signal intensities to positions x_1 and x_2 respectively in two separate images. In non-overlap regions, PLACE-1L is executed with any two images. The combination of the two PLACE-2L images and the PLACE-1L image yields a reconstructed image that matches the original object.

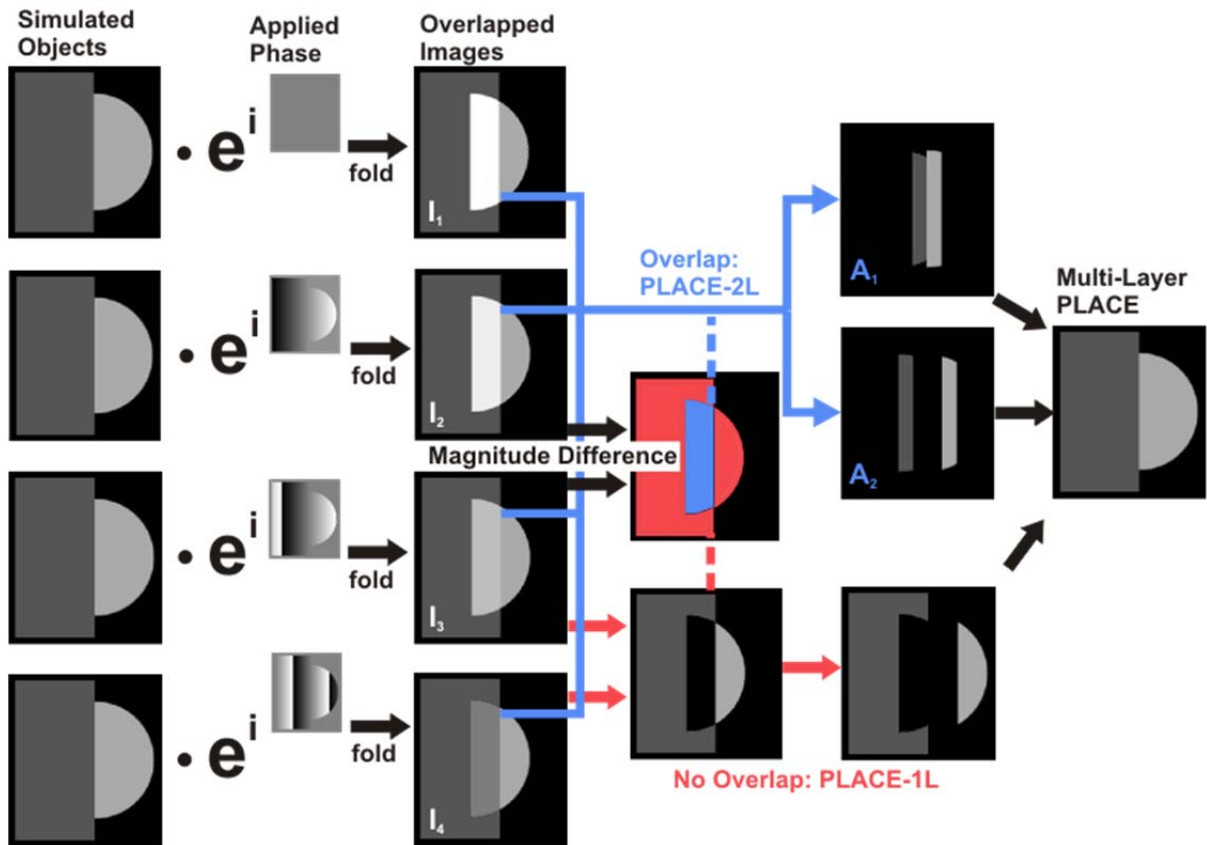


Figure 4.7 Two-layer PLACE (2L) simulation workflow. Four objects (left) are simulated and $m = (0,1,2,3) \times 2\pi$ phase twists applied across their respective FOVs. Data is overlapped to yield $I_1/I_2/I_3/I_4$ images. The magnitude difference of I_2 and I_3 is computed; PLACE-1L of I_2 and I_3 is computed for null regions in red, and PLACE-2L of $I_1/I_2/I_3/I_4$ is computed for overlap regions in blue. The two PLACE-2L images and the PLACE-1L image are combined to reconstruct the original object.

This solution appears robust with noiseless simulated data, but the application to noisy data was less successful. Another circle/square object was replicated four-fold with respectively varied phase ramps as in Figure 4.7. These objects were then manually overlapped and bivariate Gaussian noise of mean zero was added to generate images. Figure 4.8 depicts one of the overlapped images, and the final solution image computed with minimal post-processing.

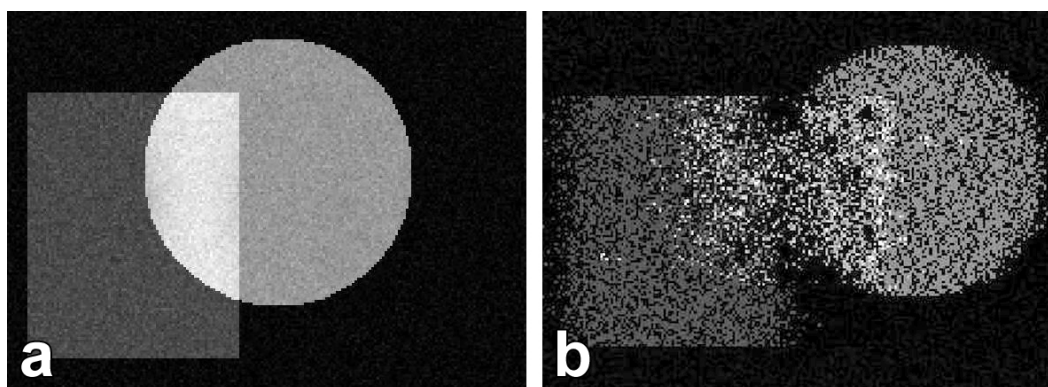


Figure 4.8 Two-layer PLACE (2L) noisy simulation. a) Variably phase ramped, overlapped, noisy image. b) PLACE-2L solution of four variably phased and overlapped images, unprocessed aside from some layer matching (A_1 with x_1 , and A_2 with x_2).

It is immediately obvious that with noise, PLACE-2L experiences difficulties. A matching scheme using phase coherence was required to unambiguously match A_1 with x_1 and A_2 with x_2 ; this complicates an already tenuous correction.

4.2.3 Phantom Experiments

The noiseless simulation asserted that the absolute magnitude difference of two variably phase ramped images should have non-zero pixels in overlap regions as long as the signal displacement occurs along the same dimension as the phase ramps are applied. The same assertion can be made for noisy data, with the more conservative expectation that overlap regions will have only relatively bright pixels in the difference image. The base TSE magnitude images employed in Figure 4.5 and Figure 4.6 with $m = 0$ and $m = 5 \times 2\pi$ phase twists across their respective FOVs are shown in Figure 4.9, along with a magnitude difference image. The brighter regions in the magnitude difference image are located around the perceived overlap regions of the original distorted images, indicating that the brightness could stem from in-plane pixel overlap. An implementation of PLACE-2L may thus prove beneficial for unraveling the overlap.

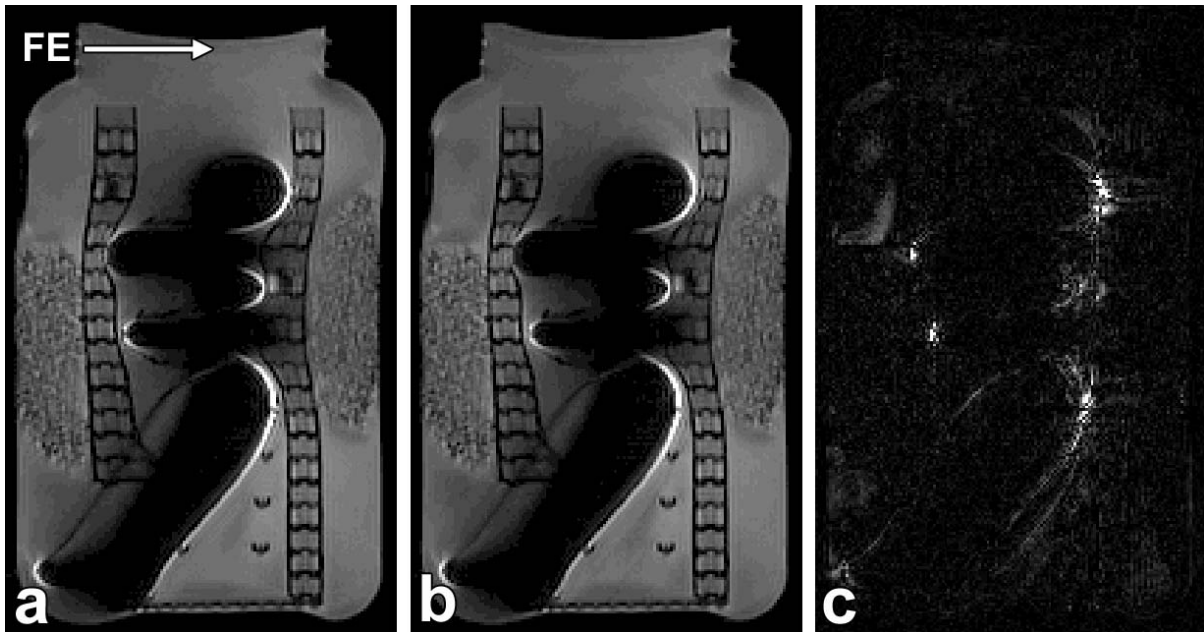


Figure 4.9 Bright signal appears to arise from in-plane pixel overlap. Turbo spin echo magnitude images of the CrCoMo/Lego phantom with $m =$ a) 0 and b) $5 \times 2\pi$ phase twists applied across their respective FE FOVs. c) $|a-b|$ magnitude difference shows dissimilarities in perceived overlap regions.

PLACE-1L and PLACE-2L solutions were executed separately for all pixels of the slice depicted in Figure 4.9. Figure 4.10 depicts the results for both approaches, where PLACE-1L used $m = (0, 2) \times 2\pi$ phase twists across its two images' respective FE FOVs, and PLACE-2L employed $m = (0, 2, 4, 6) \times 2\pi$ phase twists across its four images' respective FE FOVs.

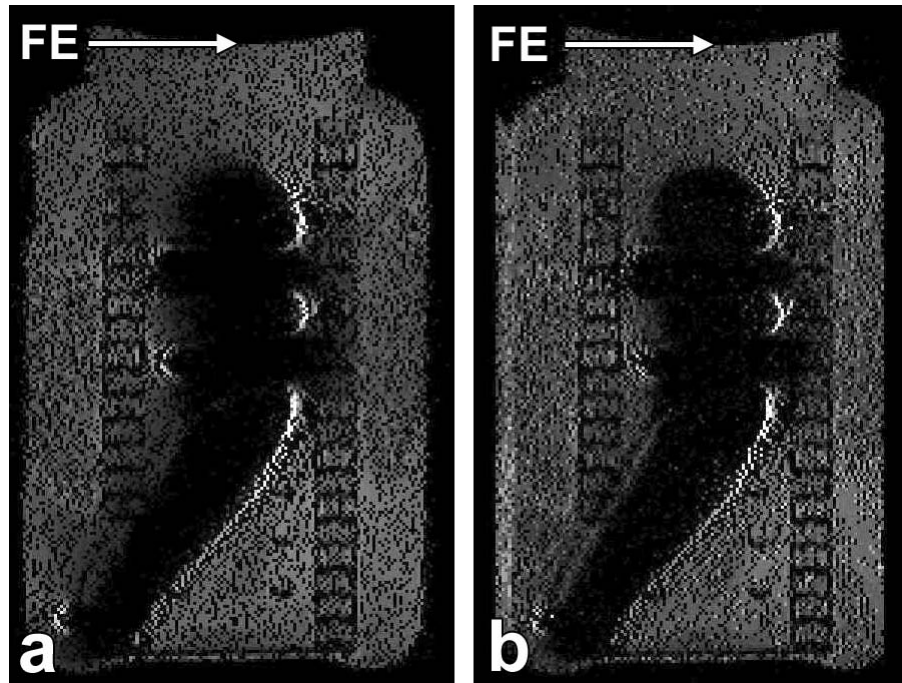


Figure 4.10 Phantom PLACE-1L and PLACE-2L corrections. a) PLACE-1L correction of turbo spin echo (TSE) magnitude images with $m = (0,2) \times 2\pi$ phase twists across their FE FOVs. b) PLACE-2L correction of TSE images with $m = (0,2,4,6) \times 2\pi$ phase twists across their FE FOVs.

Figure 4.10 shows that PLACE-2L is able to achieve distortion correction similar to PLACE-1L, validating the base formalism. Unfortunately, there are several problems with the PLACE-2L solution. Aliasing is evident on the left of the reconstruction; these pixels are aliased due to phase ambiguity in the positioning calculation, as experienced for PLACE-1L in Figure 4.5f. Sporadic bright pixels throughout the PLACE-2L image most likely stem from single-layer pixels erroneously thought to be of the overlapping two-layer variety. Most troublesome is the fact that the unraveling of bright signal overlap regions is not realized. This may indicate that the bright regions are not caused by in-plane signal overlap stemming from pixel shift, but rather a through-plane artifact such as slice thickening or splitting.

The two-layer 3D-PLACE framework for metal artifact correction is sound in theory, shows resounding success with noiseless simulated images, and is able to correct single-layer distortions in the same manner as the regular 3D-PLACE technique described in section 4.1.

However, like PLACE-1L, PLACE-2L is unable to correct through-plane slab selection artifacts, which can yield signal loss near the metal. Furthermore, PLACE-2L shows difficulty in resolving multiple layers in noisy simulated data, and is not viable in its present form for unraveling in-plane signal overlap in experimental images. Due to the technique's sensitivity to noise and the potential that through-plane artifact mechanisms account for uncorrected signal loss and overlap, there are doubts as to the viability of this methodology.

4.3 Summary

The PLACE technique is extremely useful for imaging in regions of in-plane distortion. A strain called 3D-PLACE was shown to correct FE distortions generated by the inhomogeneous magnetic field stemming from metals. However, attempts to correct signal loss and overlap artifacts using a generalization of PLACE faced difficulties. While a two-layer model is cogent in noiseless simulations, data with noise could not be corrected with certainty. While this is in part due to the poor performance of the technique on noisy data, failure to achieve any unraveling of overlapped signal or recovery of signal lost near the implant in experimental data suggests artifacts could also stem from uncorrected through-plane mechanisms. The report subsequently will depart from further study of this method, and instead embrace the more efficient and robust methodology outlined in the next chapter.

Chapter 5: B_0 Inhomogeneity Artifact Correction with bSSFP

This chapter is the heart of the study: it introduces the bSSFP sequence, emphasizes its efficiency and excellent signal refocusing, and proposes various techniques for bSSFP artifact correction near metals. The sensitivity of bSSFP to off-resonant magnetization precession introduced in sections 2.5.3 and 3.3.4 is addressed with two techniques that exactly demodulate bSSFP signal of θ -dependence. Performance improvements that employ linear averaging and variance-weighted combinations are proposed. Signal loss is recovered with gradient shimming of inhomogeneous fields. Residual distortion in demodulated bSSFP images is eliminated using demodulation solution phase data. Finally, the techniques are discussed in terms of their utility for imaging near metals and flexibility for balancing artifact correction and scan time.

5.1 Prelude: a Gradient Echo Technique for Imaging near Metals

Most of the methods for imaging near metals described in section 3.4 have one thing in common: they employ spin-echo sequences. The gradient echo sequence is avoided due to its prominent dephasing in inhomogeneous fields; instead clinicians and researchers opt for spin-echo techniques' improved signal refocusing despite subsequently longer scan time.

The last chapter exemplified that originally this research project also employed spin-echo imaging. However, a fortunate accident at the Children's & Women's Health Centre of British Columbia led to a dramatically altered research direction. After experiencing difficulties with TSE imaging of the CrCoMo/Lego phantom, the Siemens 1.5T scanner's "TrueFISP" brand of bSSFP was tested at random. The results were astounding; resultant images showed very high fidelity with minimal signal loss, distortion, and no visible signal overlap.

How can a gradient echo sequence be useful for imaging near metals in light of their sensitivity to off-resonant precession? The answer is alluded to in the literature, where some have affirmed bSSFP's spin-echo-like refocusing capacities (18,20), and early tests have

validated the sequence's ability to image near metallic biopsy needles in spite of the relatively long TR used at the time (21). Currently, stronger bSSFP gradients permit shorter TR, leaving even less time for artifact-generating off-resonant phase evolution. Finally, it was noted in the last chapter that the strong gradients and large imaging bandwidths of bSSFP yield minimal image distortion.

However, there is no free lunch. In exchange for bSSFP's minimal artifacts near metals, it suffers from banding that a slew of research has focused on reducing (60,107-109,115,116). A primary focus of this chapter is to correct these band artifacts.

5.2 Geometric Solution for bSSFP Signal Off-Resonance Demodulation

This section introduces a complete divergence from contemporary bSSFP band correction with a geometric cross solution to signal modulation using the elliptical signal model. The linearity of the solution is exploited via a second pass weighted average to achieve improved performance. The technique is tested on both simulated and experimental images, verifying its robust abilities to correct band artifacts. Finally, the solution is compared with the 3D-PLACE technique introduced last chapter in an analysis of each technique's relative metal artifact correction abilities.

5.2.1 Background

As mentioned in Chapter 3, standard bSSFP applications attempt to limit off-resonance with short TR and $\Delta\theta = \pi$ phase cycling, and techniques like the CS or SOS combine variably RF phase-cycled images for band suppression. However, these techniques are not robust for all tissue types. Furthermore, even if techniques like the CS and SOS are able to sufficiently mitigate bands, high field inhomogeneity and tissues with complicated frequency response profiles can cause spuriously bright ridge-like structures (109) in images.

There is another approach to the problem. Consider the elliptical signal model described in section 2.5.3. Rather than making a priori assumptions of the magnetic field homogeneity or

tissue properties, can a θ -independent characteristic value of the bSSFP signal ellipse be analytically calculated? The M , a , and b parameters of Eqs. [2.17]-[2.19] and the elliptical parameters given in Table 2.1 are all suitable candidates for a θ -independent characteristic signal value. Their particular dependence on T_1 , T_2 , α , TR, and M_0 are not as important in the context of this study as their independence of θ . Here a breakthrough geometric solution (GS) for exact determination of the M parameter is described, and performance improvements are explored.

5.2.2 Theory: Geometric Solution

Consider two arbitrary points P_1 and P_2 on the Figure 5.1 bSSFP signal ellipse, separated by $\Delta\theta = \pi$ such that $P_1 = I(\theta_0)$ and $P_2 = I(\theta_0 + \pi)$, with θ_0 being an arbitrary off-resonance value.

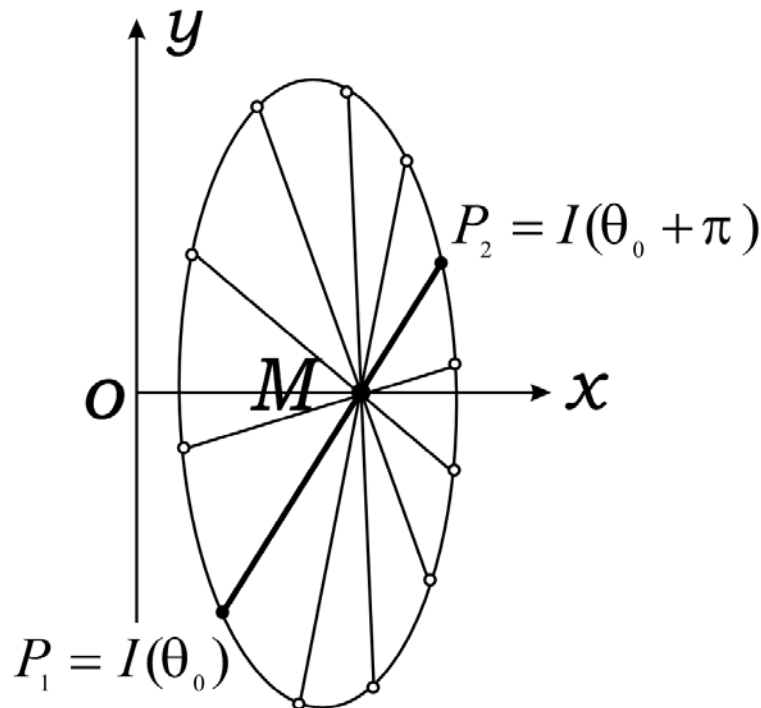


Figure 5.1 bSSFP signal ellipse shows M parameter localization. Equal θ increments non-uniformly populate the ellipse, but a line connecting two points with $\Delta\theta = \pi$ must pass through M .

A line connecting these two points in the complex plane is given by a weighted sum of the two values $P_1w + P_2(1 - w)$ where $0 < w < 1$. Equation [2.22] may be enlisted to parameterize this line

$$P_1w + P_2(1 - w) = M \frac{1 - E_2 e^{-i\theta_0}}{1 - b \cos \theta_0} \cdot w + M \frac{1 + E_2 e^{-i\theta_0}}{1 + b \cos \theta_0} \cdot (1 - w) \quad [5.1]$$

Note that if $w = (1 - b \cos \theta_0)/2$, Eq. [5.1] simplifies to M . Since $0 < b < 1$ and $-1 < \cos \theta_0 < 1$, the requirement $0 < w < 1$ is satisfied: M always lies on a line connecting P_1 and P_2 . Thus by sampling four points on the ellipse consisting of two sets of points each with $\Delta\theta = \pi$ relative phase cycling, M may be located at the intersection of the lines connecting the respective sets. Figure 5.1 illustrates this GS, often called the XS cross-resolution (117) since it is located at the crossing point of two lines. The parameter M can serve as a demodulated signal value much like the ‘‘centre-of-mass’’ $\langle I \rangle$ in Eq. [2.24] that the CS converges upon as $N \rightarrow \infty$. The GS finds M exactly, whereas the CS only approximates $\langle I \rangle$ through averaging.

Assume that x_1, x_2, x_3 , and x_4 are the real and y_1, y_2, y_3 , and y_4 are the imaginary components of the complex-valued pixel signals I_1, I_2, I_3 , and I_4 in four bSSFP images respectively phase cycled by $\Delta\theta = 0^\circ, 90^\circ, 180^\circ$, and 270° . M may be found exactly from the intersection of a line connecting (I_1, I_3) and a line connecting (I_2, I_4) in the complex plane; this can be expressed by

$$M_{GS} = \frac{(x_1 y_3 - x_3 y_1)(I_2 - I_4) - (x_2 y_4 - x_4 y_2)(I_1 - I_3)}{(x_1 - x_3)(y_2 - y_4) - (x_2 - x_4)(y_1 - y_3)} \quad [5.2]$$

M_{GS} unambiguously determines M , yielding a new image contrast as defined by Eq. [2.17]. As discussed in 2.5.3, any additional phase factors simply rotate the signal ellipse, and do not affect the GS. The GS also has the added strength that the real and imaginary (x and y) components may be swapped without affecting the final solution.

5.2.3 Theory: GS-guided Weighted Average

A pixel-by-pixel computation with Eq. [5.2] is a non-linear process that may suffer instabilities in noise, with non-signal background regions yielding sparsely scattered bright pixels. The following steps can regularize and linearize the solution for improved performance (118). First, if a GS reconstruction pixel has a magnitude greater than the maximum magnitude of all four input image pixels, the solution is replaced by the CS. This regularizes and removes singularities from the reconstruction. Second, since M is always located along lines connecting (I_1, I_3) and (I_2, I_4) , it can be expressed as a linear weighted average of either pair.

Let I_w be a weighted average of the image signal pair (I_1, I_3)

$$I_w = I_1 w + I_3(1 - w) \quad [5.3]$$

The proper weight w can be obtained regionally to yield the correct M by using the pixel-by-pixel GS for guidance. This is achieved by minimizing the regional differential energy E between I_w and the solution M_{GS} directly obtained from Eq. [5.2]. E is defined as

$$E = \sum_{\text{region}} (I_w - M_{GS})^* (I_w - M_{GS}) \quad [5.4]$$

where “*” indicates complex conjugation. Inserting I_w from Eq. [5.3]

$$E = \sum_{\text{region}} [(I_1 - I_3)^* (I_1 - I_3) w^2 + (I_3 - M_{GS})^* (I_1 - I_3) w + (I_1 - I_3)^* (I_3 - M_{GS}) w + (I_3 - M_{GS})^* (I_3 - M_{GS})] \quad [5.5]$$

To minimize E , we equate $\partial E / \partial w$ to zero

$$\begin{aligned} \frac{\partial E}{\partial w} = \sum_{\text{region}} [2(I_1 - I_3)^*(I_1 - I_3)w + (I_3 - M_{GS})^*(I_1 - I_3) \\ + (I_1 - I_3)^*(I_3 - M_{GS})] = 0 \end{aligned} \quad [5.6]$$

and solve for w

$$w = \frac{\sum_{\text{region}} [(I_3 - M_{GS})^*(I_3 - I_1) + (I_3 - I_1)^*(I_3 - M_{GS})]}{2 \sum_{\text{region}} [(I_1 - I_3)^*(I_1 - I_3)]} \quad [5.7]$$

With a square region of 5x5 pixels, Eq. [5.7] is computed to find the proper weight w for a central pixel, and for all pixels by shifting the region around. A linear solution image is formed by inputting the weights into Eq. [5.3] at each pixel. The same operation is performed for image set (I_2, I_4) , yielding a second linear solution. The final second pass image is obtained by averaging the two linear solution images for improved SNR. This GS-guided weighted average (GS-WA) is essentially a weighted average of the four original datasets, which should achieve similar SNR to the CS since the weights are within the (0,1) range.

5.2.4 Methods: Simulation

Continuously varying parameter bSSFP images were simulated using Eq. [2.16] with TR = 4.2ms, $\alpha = 40^\circ$, and a , b , M , and θ parameters varied as follows: tissue relaxation values $T_1 = 200\text{--}3000$ ms and $T_2 = 40\text{--}3000$ ms at 1.5T (24-28) correspond to $a = 0.9$ to 0.9999 and $b = 0.1$ to 0.8; this range of a and b were set on the horizontal and vertical axes respectively. For each of the nine a values employed, θ was varied from $-\pi$ to π , yielding a total horizontal θ variation of 18π . To restrict variation to T_1 and T_2 as a and b change, M must also change. Its regional value is found by juggling Eq. [2.17] such that

$$M = \frac{M_0 b \sin \alpha}{a(1 + \cos \alpha)} \quad [5.8]$$

The resulting M/M_0 range is 0.036 to 0.32. Four images were generated with respective RF phase cycling of $\Delta\theta = 0^\circ, 90^\circ, 180^\circ,$ and 270° , and bivariate Gaussian white noise with mean zero was added.

5.2.5 Methods: Experiments

The Siemens 1.5T Avanto scanner was employed to image the phantom from section 4.1.2. A revised phantom was also built for signal loss measurements that would be used for all further phantom measurements in this report. The inside of the Lego structure was hollowed out so that a polyethylene mesh cage holding the CrCoMo implant could be inserted. A second mesh cage holding a replica cast from polymer was also built for comparison purposes; any images of the replica represent gold standard images of the implant without B_0 artifacts. The new phantom is shown in Figure 5.2.

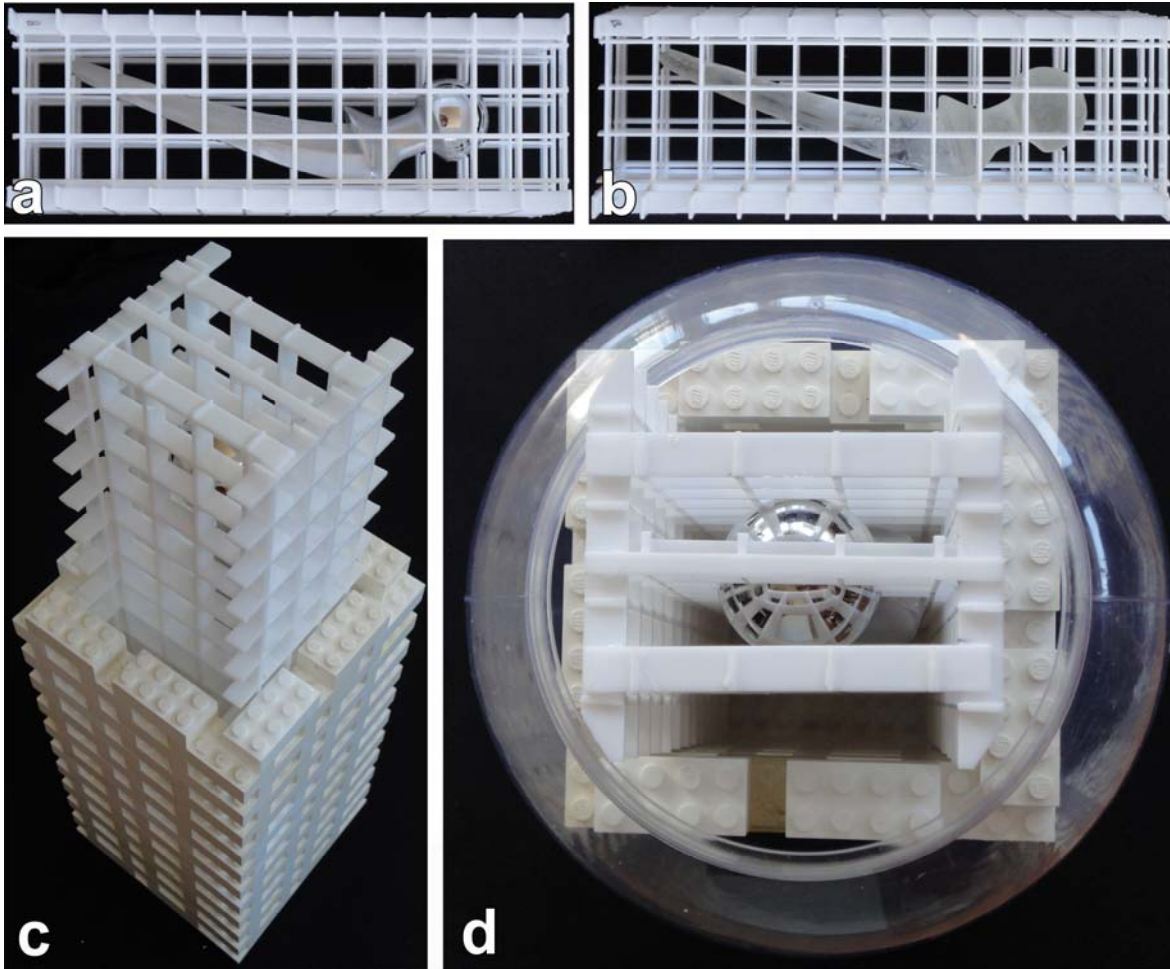


Figure 5.2 Revised chromium-cobalt-molybdenum hip prosthesis/Lego phantom with fiduciary marking. a) Implant and b) a polymer implant replica sealed in separate polyethylene cages. These cages are placed in the c) Lego structure, which was placed in d) a bottle of water.

Four phase-cycled 3D bSSFP magnitude phantom images I_j with $j = 1, 2, 3,$ and 4 were acquired with $\Delta\theta_j = 0^\circ, 90^\circ, 180^\circ,$ and 270° phase cycling respectively. Each image set required 37 seconds to acquire with $\alpha = 41^\circ$, $TR/TE = 4.2/2.1$ ms, $BW_{RO} = 143$ kHz, 256/168/52 matrix size, and 1.17/1.17/3 mm voxel size along frequency/phase/slice directions. A 3D-PLACE comparison scan was formed from two 3D TSE images with vertically applied frequency encoding to match the bSSFP data. The methodology of the 3D-PLACE image formation and its acquisition parameters are identical to that described in section 4.1.2.

Volunteer scans were performed with the CrCoMo metal implant positioned in between the

calves, and bSSFP images acquired with $\alpha = 70^\circ$, TR/TE = 4.16/2.08 ms, 256/152/72 matrix size and 1.25/1.25/3 mm voxel size along frequency/phase/slice directions. All other parameters matched the phantom experiment.

Real components x_j and imaginary components y_j of each image I_j for $j = 1, 2, 3$, and 4 were input into Eq. [5.2] for calculation of M_{GS} on a pixel-by-pixel basis. SNR was improved through the GS-WA second pass solution described in section 5.2.3.

5.2.6 Results

Figure 5.3 shows simulated a) magnitude and b) phase bSSFP images ($\Delta\theta = 0^\circ$), a c) gold standard M image, followed by d) GS, e) GS-WA, and f) CS reconstructions of the four variably phase-cycled images. The GS and GS-WA are able to completely eliminate bands for simulated data, while the CS algorithm has residual banding in some parameter regions with four-fold increased spatial frequency.

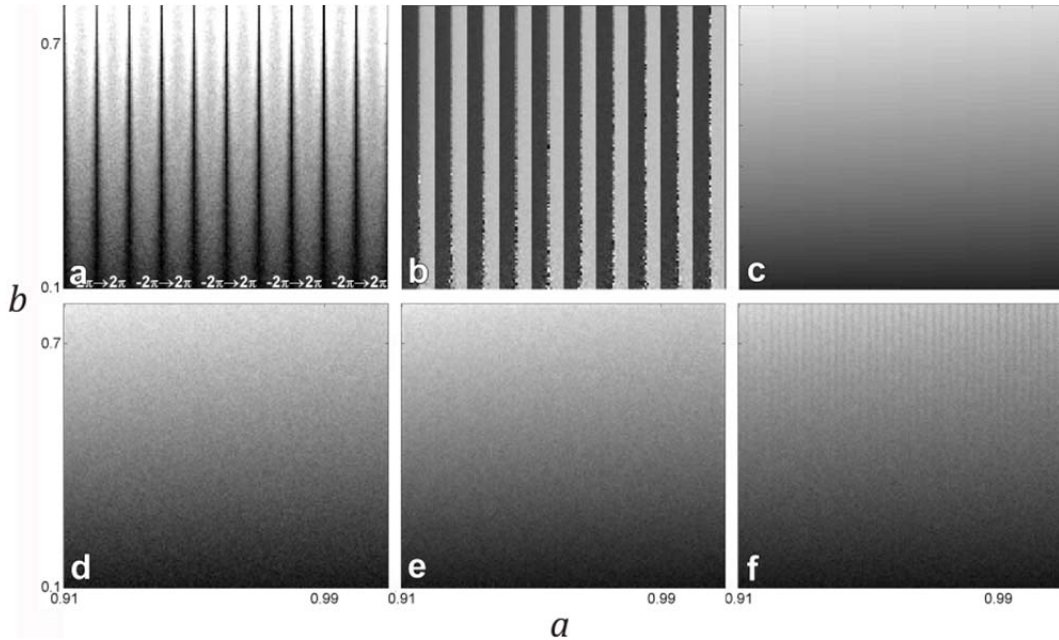


Figure 5.3 Demodulation of continuously varying bSSFP parameter simulated data. $\Delta\theta = 0^\circ$ noisy bSSFP a) magnitude and b) phase images simulated with $0.9 < a < 0.9999$ and an 18π θ -variation horizontally, $0.1 < b < 0.8$ vertically, and $0.036 < M/M_0 < 0.32$ throughout. c) Gold standard M matrix, d) geometric solution (GS), e) GS-guided weighted average, and f) complex sum of four relatively phase-cycled bSSFP datasets.

Figure 5.4 depicts the four relatively phase-cycled bSSFP magnitude images of the phantom; the CrCoMo hip prosthesis generated a strong local magnetic field inhomogeneity, resulting in banding artifacts seen as dark lines in the acquired images:

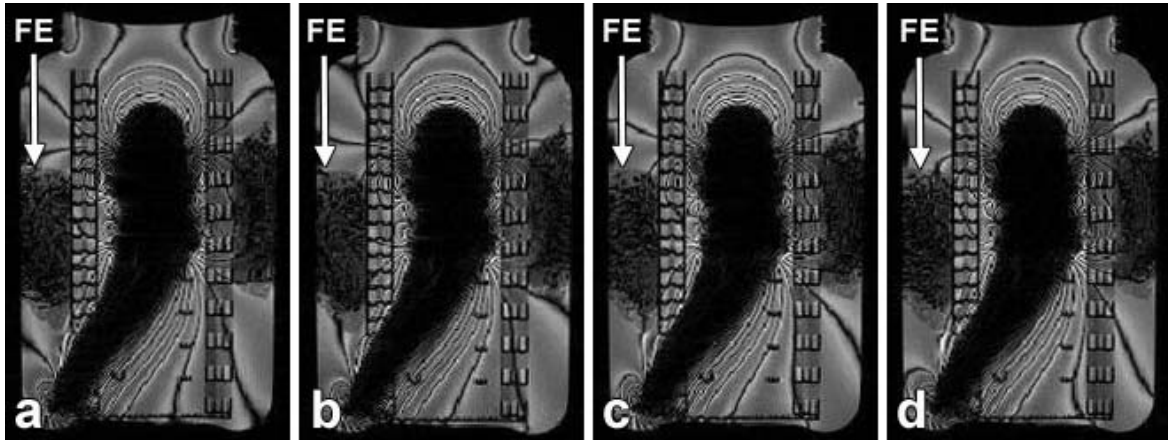


Figure 5.4 Four phase-cycled CrCoMo/Lego phantom bSSFP magnitude images. Images are phase cycled at $\Delta\theta =$ a) 0° , b) 90° , c) 180° , and d) 270° .

Figure 5.5 shows an SE image from the same location as the bSSFP images and its corresponding 3D-PLACE correction. It also shows reconstructions of the images in Figure 5.4 using the CS and the GS-WA techniques.

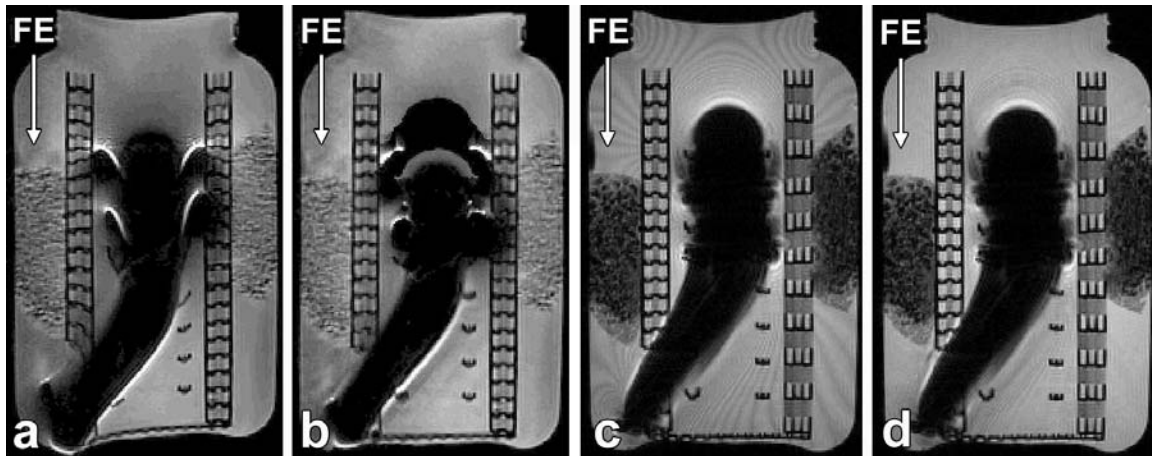


Figure 5.5 Demodulation of bSSFP CrCoMo phantom data. a) Turbo spin echo (TSE) magnitude image, b) 3D-PLACE corrected TSE magnitude image. c) Complex sum and D) geometric solution-guided weighted average reconstructions of the Figure 5.4 bSSFP images.

Although the FE direction is vertical in these images, it is only obvious in the TSE image, since strong bSSFP imaging gradients mitigate (119) and 3D-PLACE eliminates FE distortion. The CS image has residual dark bands with four-fold greater spatial frequency than the original images, while GS-WA eliminates banding artifacts. The GS-WA retains some signal loss and subtle banding near the implant, although no prominent signal overlap is evident.

Table 5.1 compares various reconstruction metrics of the GS-WA and 3D-PLACE. All four of the GS-WA's bSSFP images are acquired in ~1/4 of the time needed for 3D-PLACE's two TSE images. The GS-WA has almost twice the SNR of 3D-PLACE, measured from the mean value of a relatively homogeneous signal region divided by its standard deviation. The GS-WA signal loss is ~60% the size of the 3D-PLACE signal loss, calculated from a ratio \mathbf{b}/\mathbf{a} , where \mathbf{b} is the reconstruction signal loss area and \mathbf{a} is the area of the lack of signal from the replica. These regions are shown in Figure 5.6 for the GS-WA signal loss calculation; a similar calculation is made for 3D-PLACE. Finally, the GS-WA requires minimal and 3D-PLACE requires little pulse sequence programming and post-processing time.

Technique	3D-PLACE	GS-WA
Scan time [minutes]	8.7	2.5
FE distortion	Eliminated	Minimized
Signal loss ' \mathbf{b}/\mathbf{a} '	1.9	1.1
Signal overlap	Yes	Minimal
SNR	8.7	16.4
Pulse sequence programming	Little	None
Post-processing time [seconds]	< 60	< 10

Table 5.1 Comparison of 3D-PLACE and geometric solution-guided weighted average (GS-WA) metal artifact correction metrics. Signal loss = (reconstruction signal loss region ' \mathbf{b} ')/(replica area ' \mathbf{a} '); Figure 5.6 illustrates these regions for the GS-WA. SNR = (signal region mean)/(signal region standard deviation).

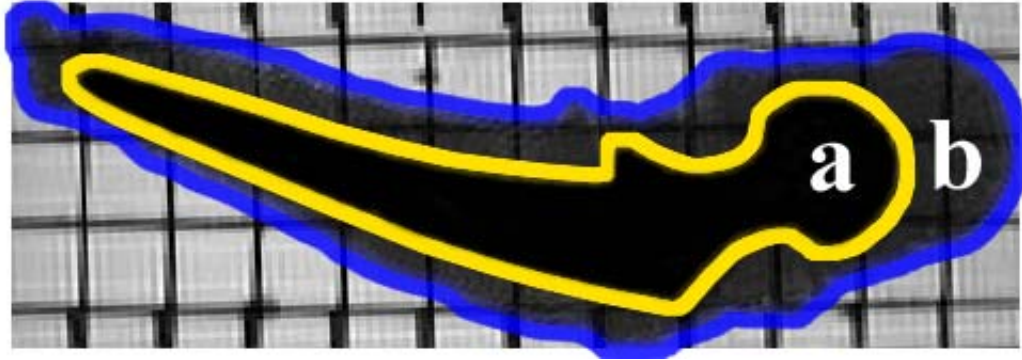


Figure 5.6 Artifactual vs. true signal loss for the geometric solution-guided weighted average (GS-WA). Replica area 'a' is inside yellow contour. GS-WA signal loss region 'b' is inside blue contour.

Figure 5.7 a&c show two image sets of three orthogonal slices each; they are bSSFP magnitude images of one of the four phase cycles acquired of a volunteer with an implant placed between his calves. The corresponding reconstructed GS-WA images in Figure 5.7 b&d demonstrate that all banding artifacts seen as artifactual dark lines have been successfully removed. However, some uncorrected signal loss is evident in both the bSSFP and GS-WA images.

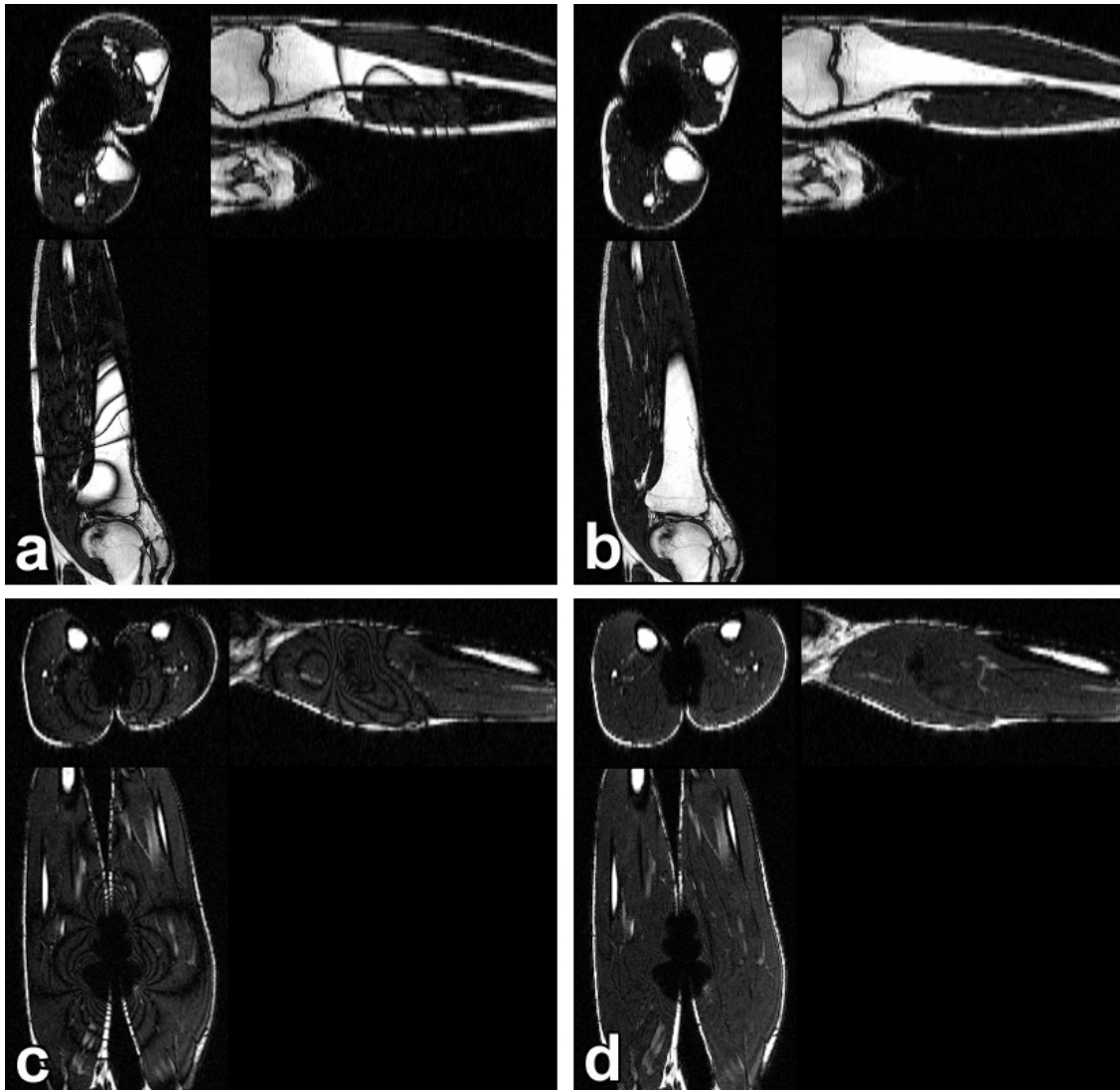


Figure 5.7 Geometric solution-guided weighted average (GS-WA) correction of in vivo bSSFP calf images with nearby CrCoMo implant. a) and c) show $\Delta\theta = 0^\circ$ images of three orthogonal slices each, and b) and d) show the GS-WA reconstructions from four phase-cycled bSSFP images.

5.2.7 Discussion

The GS-WA is a valuable method for bSSFP artifact correction in inhomogeneous magnetic fields. It is robust over all (a, b, θ) parameter combinations tested, uniformly removing dark banding and signal modulation seen as intensity variations. Other multi-acquisition bSSFP reconstructions such as the CS yield residual banding and signal modulation for some parameter regions, thus requiring tissue and/or system parameter assumptions for successful

implementation. The strong bSSFP gradients also limit dephasing and subsequent signal loss relative to 3D-PLACE. This may be understood by considering that since bSSFP employs a greater BW_{RO} than the spin-echo method, a relatively reduced range of off-resonance per voxel ensures a lesser chance of signal cancellation.

The GS-WA technique also surpasses TSE SNR and overall efficiency in the present implementation. Due to high TrueFISP bSSFP signal in water and implicit GS-WA averaging, it almost doubles the phantom image SNR of 3D-PLACE. The required TrueFISP images were acquired in only 2-2.5 minutes, a fraction of that needed for 3D-PLACE and most other metal artifact correction techniques. Siemens TrueFISP sequence programming is unnecessary since phase cycling $\Delta\theta$ may be implemented directly on the console, and the GS-WA reconstruction takes only a few seconds to execute.

While the GS-WA exhibits efficient artifact correction near metals, it is by no means a complete solution. The GS-WA still suffers from some signal loss near the metal. While no prominent signal overlap is evident, it could be hidden in the signal loss regions where precession frequency changes are rapid. Distortion is mitigated by powerful gradients, but not eliminated as with 3D-PLACE. The GS-WA also showed very subtle indications of residual band artifact near signal loss regions, although this is marginal relative to the CS.

This leads to a discussion of the best applications of the technique. It appears useful for fast imaging near metals if some artifacts close to the metal are permissible, but for more comprehensive correction, techniques such as SEMAC and MAVRIC may be more appropriate. The GS-WA in its present form is well suited for general bSSFP imaging in inhomogeneous magnetic fields. It would be valuable for cardiac imaging and angiography where bSSFP is frequently employed, especially if the particular imaging procedure is hindered by banding.

Another concern with the GS-WA is that it may not have the desired contrast for most clinical procedures. Spin-echo imaging has very flexible image contrast which is diagnostically useful, while bSSFP exhibits unique contrast which is not always desirable.

However, bSSFP may be combined with magnetization preparation methods to enhance contrast (120); each of the GS-WA's component bSSFP images could be acquired with added magnetization preparation sequence blocks to ensure flexible imaging.

Section 2.5.3 discussed how bSSFP signal's elliptical characteristics may be analyzed if the global phase factors of equation [2.16] are ignored. The additional phase factors will only rotate the ellipse to another orientation, without affecting the relative location of the geometric solution.

Overall the GS and GS-WA prove to be a great innovation for bSSFP debanding and general signal demodulation of off-resonance dependence. The technique is robust over all tissue types, and thus can be employed for general bSSFP imaging in inhomogeneous fields. It takes little scan time to generate high-fidelity images, even in problematic regions relatively close to a high susceptibility implant. The results also show that there is much room for improvement to achieve comprehensive metal artifact correction.

5.3 Algebraic and Geometric-Algebraic Solution for bSSFP Signal Off-Resonance Demodulation

An algebraic solution (AS) to bSSFP signal modulation that complements the GS was recently discovered. The uniqueness of the two solutions inspires the development of a composite geometric-algebraic solution (GAS) for improved performance. The error, SNR, and overall capabilities of the GAS, GS, AS, GS-WA, and CS are compared. The relative performance of the GS, AS, and GAS as a function of noise and T_1/T_2 ratio is also analyzed. The minimal error and robust performance of GAS indicate its suitability as the demodulation piece of the bSSFP metal artifact correction puzzle.

5.3.1 Background

Phase cycling in bSSFP effectively samples the signal profile at unique off-resonance values; if enough points on the profile are sampled, it should be possible to determine a characteristic

demodulated magnetization. Section 5.2 used geometric intuition to exactly solve for such a point with four phase-cycled datasets (117). This problem may also be viewed from an algebraic standpoint. Since four unique phase-cycled images are sampled, their underlying signal may be formulated by four unique equations. Since there are four parameters in Eq. [2.16], it should be possible to solve for any one of them algebraically.

Here we reveal a new method that uses algebra to demodulate bSSFP signal (121). The AS derives the same underlying M signal as the GS, but exhibits unique performance on noisy data. This motivates the weighted averaging of the two solutions for improved SNR. The discovery of a second independent solution to the problem also inspires further efforts to reduce the amount of data required for exact bSSFP signal demodulation from off-resonance dependence.

5.3.2 Theory

If four complex phase-cycled bSSFP images I_j , where $j = 1, 2, 3,$ and 4 , are acquired with $\Delta\theta_j = 0^\circ, 90^\circ, 180^\circ,$ and 270° respective phase cycling, it is possible to express each image's signal uniquely using Eq. [2.16]

$$I_1 = M \frac{1 - ae^{i\theta}}{1 - b \cos \theta} \quad I_2 = M \frac{1 + iae^{i\theta}}{1 + b \sin \theta} \quad I_3 = M \frac{1 + ae^{i\theta}}{1 + b \cos \theta} \quad I_4 = M \frac{1 - iae^{i\theta}}{1 - b \sin \theta} \quad [5.9]$$

Global phase factors are neglected as discussed in section 2.5.3. These four equations are functions of the four parameters $M, a, b,$ and θ , and so the system can be solved for M in terms of the known image values $I_1, I_2, I_3,$ and I_4

$$M_{AS} = \frac{I_1 I_3 (I_2 - I_4)(1 + i) + I_2 I_4 (I_1 - I_3)(1 - i)}{I_1 I_2 - I_3 I_4 + i(I_2 I_3 - I_1 I_4)} \quad [5.10]$$

This derivation was verified with Maple™. An interesting characteristic of the AS is that the solution fails when real and imaginary components are swapped. This contrasts with the GS, which is invariant to component swapping, and indicates that the two solutions may be independent.

Due to the GS' and AS' identical underlying base signal and their unique performance on noisy data that shall be revealed, corresponding M_{GS} and M_{AS} pixels may be optimally combined. The GAS is formed from a weighted average of the GS and AS with weights determined by their regional image variances V_{GS} and V_{AS} (121) to yield M_{GAS}

$$M_{GAS} = M_{GS}W_1 + M_{AS}W_2 = \frac{V_{AS}^2M_{GS} + V_{GS}^2M_{AS}}{V_{AS}^2 + V_{GS}^2} \quad [5.11]$$

$M_{GS} = M_{AS} = M$ in noiseless scenarios, thus $M_{GAS} = M$ since $W_1 + W_2 = 1$. Appendix C demonstrates that this general formulation yields minimal noise variance in the final image; this will also apply to the GAS combination of Eq. [5.11] if the GS and AS noise are uncorrelated.

5.3.3 Methods

The continuously varying parameter data from Figure 5.3 was employed for this section. A second “tri-tissue” dataset simulates three tissues with T_1/T_2 ratios 420/50, 240/70, and 2400/1400 to emulate liver, fat, and cerebrospinal fluid (24-28) respectively. These correspond to parameter values $a = (0.92, 0.94, 0.997)$, $b = (0.31, 0.52, 0.69)$, and $M/M_0 = (0.12, 0.20, 0.25)$, which were simulated in three horizontally separate regions. Four complex datasets phase cycled by $\Delta\theta = 0^\circ, 90^\circ, 180^\circ, \text{ and } 270^\circ$ were computed using Eq. [2.16], with θ varied from $-2\pi \rightarrow 2\pi$ vertically.

Experimental images were acquired of the CrCoMo/Lego phantom of Figure 5.2, with a liver paté and gelatin packet inserted in the side. The TrueFISP bSSFP acquisition employed $\alpha = 40^\circ$, 256/152/176 matrix size and 1.17/1.17/1 mm voxel size along frequency/phase/slice directions; remaining parameters were identical to those in the GS section 5.2.5.

Experimental in vivo data involved positioning the CrCoMo implant between the thighs of a volunteer, and acquiring bSSFP thigh images with $\alpha = 36^\circ$, TR/TE = 4.5/2.25 ms, 256/192/176 matrix size and 1.09/1.09/2 mm voxel size along frequency/phase/slice

directions. All other parameters matched those from the calf data in section 5.2.5.

The GS, AS, and GAS images of simulated and experimental datasets were computed pixelwise. The GS and AS were first found by inputting complex signal values I_j , their real parts x_j , and imaginary parts y_j with $j = 1, 2, 3$, and 4 into Eqs. [5.2] and [5.10], and the magnitudes computed. Image noise was approximated from the differences of the GS and AS images and smoothed versions of themselves. Regional variance of the two noise images was calculated using a 5x5 region surrounding the pixel of interest; these values were coupled with the GS and AS to find the GAS minimal variance image using Eq. [5.11] for each pixel.

Total relative error (TRE) was computed for simulated data with

$$\text{TRE} = \frac{\sqrt{\sum_{x,y} [I_{recon}(x,y) - |I_{gold}(x,y)|]^2}}{\sum_{x,y} |I_{gold}(x,y)|} \quad [5.12]$$

where I_{recon} is the reconstructed pixel magnitude, and I_{gold} is the known gold standard magnitude that the reconstruction seeks to emulate. Experimental phantom data performance was quantified by the SNR from relatively homogeneous image regions, measured via the mean magnitude signal divided by its standard deviation.

The GS, AS, GAS, and CS reconstruction capabilities were also compared. The TRE was calculated as a function of a) variable base image noise and b) variable T_1/T_2 ratio. A plot of TRE as a function of a) variable noise was achieved by calculating the TRE of GS, AS, GAS, and CS reconstructions of continuously varying parameter data similar to Figure 5.8, and repeating the procedure with variable added bivariate Gaussian noise. The plot of TRE as a function of b) variable T_1/T_2 ratio was achieved by first recognizing that the noisy simulated bSSFP data shown in Figure 5.8 was generated using variable a and b values, which correspond to vertically varying, horizontally constant T_1/T_2 . The TRE of each row thus gives TRE as a function of T_1/T_2 .

5.3.4 Results: Simulations

Figure 5.8 is a continuation of Figure 5.3, with the new focus on contrasting the GS, AS, and GAS. It depicts a $\Delta\theta = 0^\circ$ simulated bSSFP magnitude image with continuously varying M , a , b , and θ , and GS, AS, and GAS images reconstructed using additional $\Delta\theta = 90^\circ$, 180° , and 270° images. All three eliminate banding and signal modulation. Although the GS and AS of noiseless data exactly yield the simulated gold standard M depicted in Figure 5.3c, with noise the AS has difficulty in the higher signal/ b -value regions. Regardless, the GAS technique ameliorates the regional instabilities of either technique via an optimal combination.

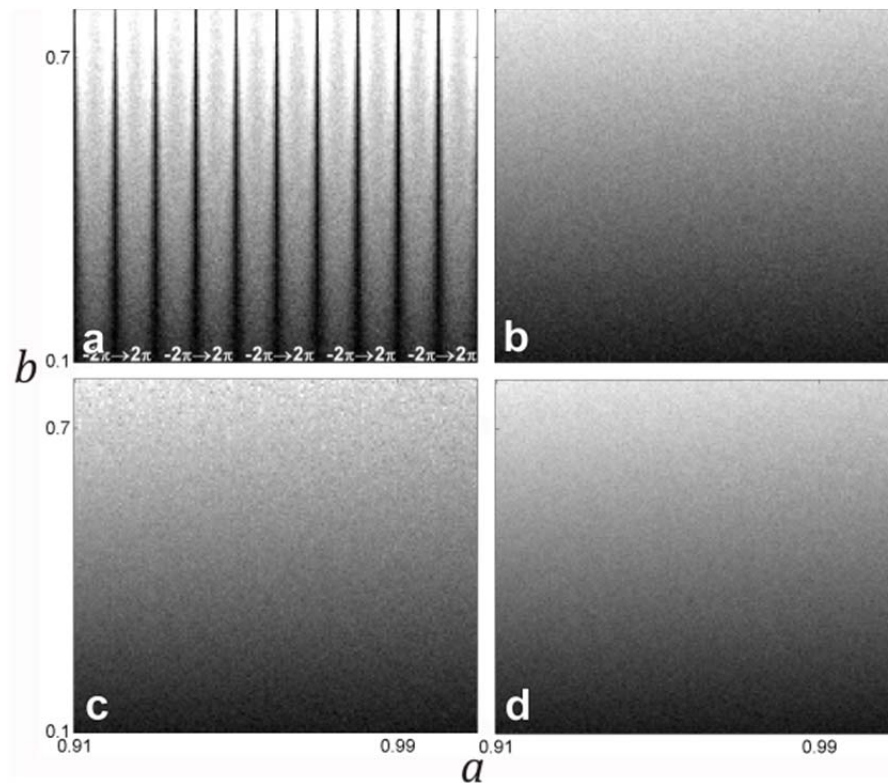


Figure 5.8 Demodulation of continuously varying bSSFP parameter simulated data cont'd. a) $\Delta\theta = 0^\circ$ noisy bSSFP magnitude image simulated with $0.9 < a < 0.9999$ and an 18π θ -variation horizontally, $0.1 < b < 0.8$ vertically, and $0.036 < M/M_0 < 0.32$ throughout. b) Geometric solution, c) algebraic solution, and d) weighted geometric-algebraic solution of four relatively phase-cycled bSSFP datasets.

GS, AS, and GAS regional variance maps for the continuously varying parameter simulation of Figure 5.8 are shown in Figure 5.9. Figure 5.9c accentuates the aforementioned difficulties that the AS has in the upper regions of Figure 5.8c. Figure 5.9d shows white pixels where the GAS had less variance than both the GS and the AS, relaying that in 94.6% of simulated pixels, the GAS has less variance than both the GS and the AS.

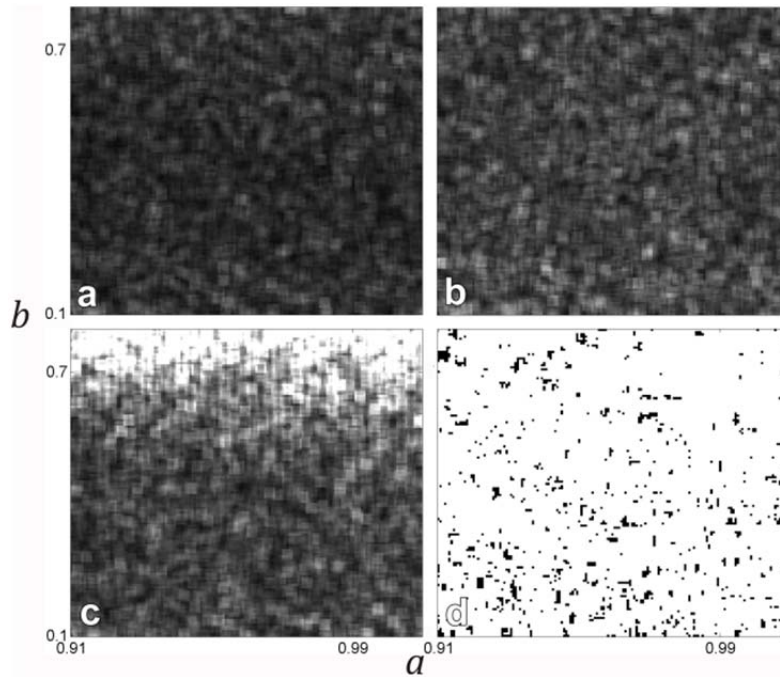


Figure 5.9 Variance maps of continuously varying bSSFP parameter simulated data. a) Geometric-algebraic solution, b) geometric solution, and c) algebraic solution regional variance maps using 5x5 pixel regions in Figure 5.8. d) 94.6% of pixels (white) indicate lower variance in a) than both b) and c).

Figure 5.10 shows all four phase-cycled simulated magnitude and phase images of the “tri-tissue” simulated data, and the corresponding GS, AS, GAS, GS-WA and CS. The GS, AS, and GAS techniques eliminate signal modulation, and visually the GAS and GS-WA appear optimal. The CS shows evidence of residual banding in the left two “tissue” regions.

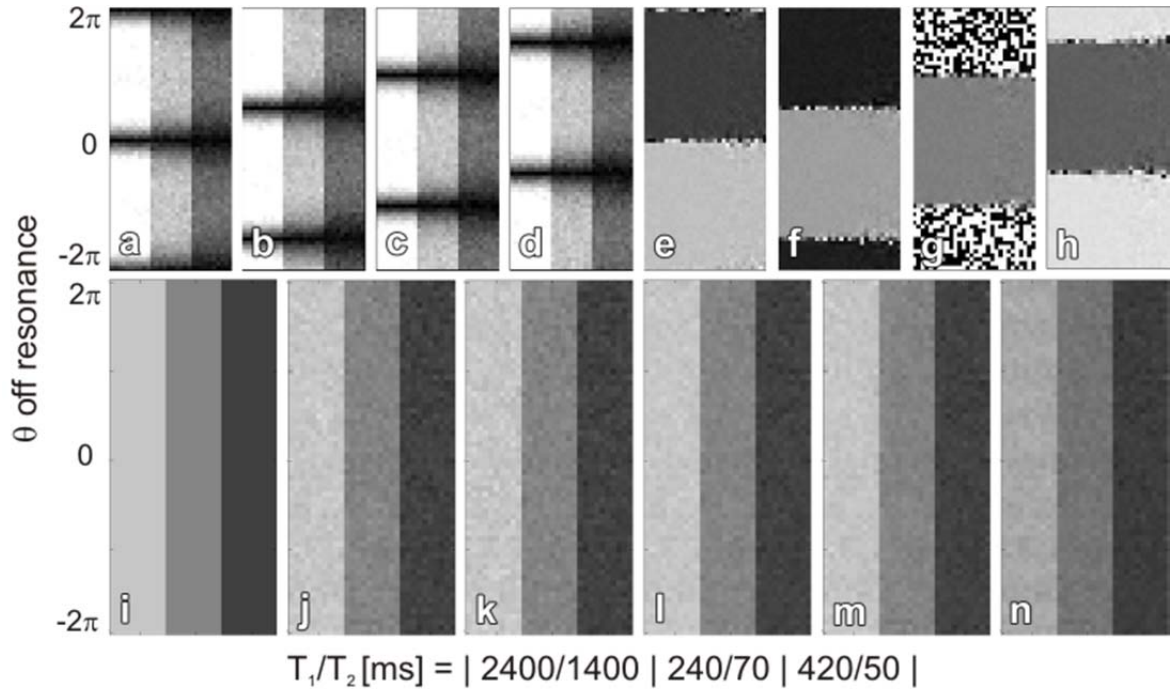


Figure 5.10 Demodulation of segmented “tri-tissue” bSSFP simulated data. Noisy bSSFP magnitude & phase images phase cycled by $\Delta\theta =$ a)&e) 0° , b)&f) 90° , c)&g) 180° , and d)&h) 270° respectively. “Tissues” with $T_1/T_2 = 2400/1400, 240/70,$ and $420/50$ are delimited horizontally, and θ is varied from -2π to 2π vertically. i) Gold standard M image. Reconstructions of a)-h) data include the j) geometric solution (GS), k) algebraic solution, l) geometric-algebraic solution, m) GS-guided weighted average, and n) complex sum.

Table 5.2 details TRE values measured for the GS, AS, GAS, GS-WA, and CS simulations of Figure 5.8 and Figure 5.10. TRE gold standard reference images are M from Figure 5.3c and Figure 5.10i for all but the CS; its gold standard was simulated using $\langle I \rangle$ from Eq. [2.24]. No TRE measurement for the GS-WA in Figure 5.3e was made, since its regional processing creates biased contrast due to unrealistic pixel-to-pixel parameter variations.

The GAS and the GS-WA consistently have low error, with the GAS’ error lower than all techniques in two of the three “tri-tissue” regions. The CS shows that in spite of its residual bands, it exhibits similar and often less error than the GS. The GS in turn typically has less error than the AS. The AS’ high variability in high b , low T_1/T_2 regions of Figure 5.8c and Figure 5.9c is verified by the AS’ high TRE in the low $T_1/T_2 = 2400/1400$ ms tri-tissue region. This implies that in low T_1/T_2 regions, the AS will contribute little to the GAS weighted sum of Eq. [5.11].

Simulation Total Relative Error				
	Continuous Data	Tri-Tissue Data		
		T_1/T_2 [ms]		
		420/50	240/70	2400/1400
GS	0.000329	0.00365	0.00184	0.00120
AS	0.000421	0.00365	0.00175	0.00138
GAS	0.000276	0.00302	0.00148	0.00095
GS-WA	N/A	0.00295	0.00155	0.00110
CS	0.000319	0.00285	0.00155	0.00119

Table 5.2 Total relative error (TRE) calculations for simulated data reconstructions. Continuous data TRE is calculated from Figure 5.8 and Figure 5.3, and “tri-tissue” data TRE is calculated from Figure 5.10. The gold standard references are M from Figure 5.3c and Figure 5.10i respectively, and $\langle I \rangle$ of Eq. [2.24] for the complex sum.

5.3.5 Results: Experiments

Figure 5.11 shows all four phase-cycled magnitude and phase images of the water/paté/gelatin phantom, and corresponding GS, AS, GAS, GS-WA, and CS image reconstructions. Note that the thin black line in all the magnitude images is the plastic holding the gelatin and liver paté. All images visibly eliminate signal modulation in paté and gelatin. The water region has consistent signal in the GS, GS-WA, and GAS, banding in the CS, and noise instability in the AS.

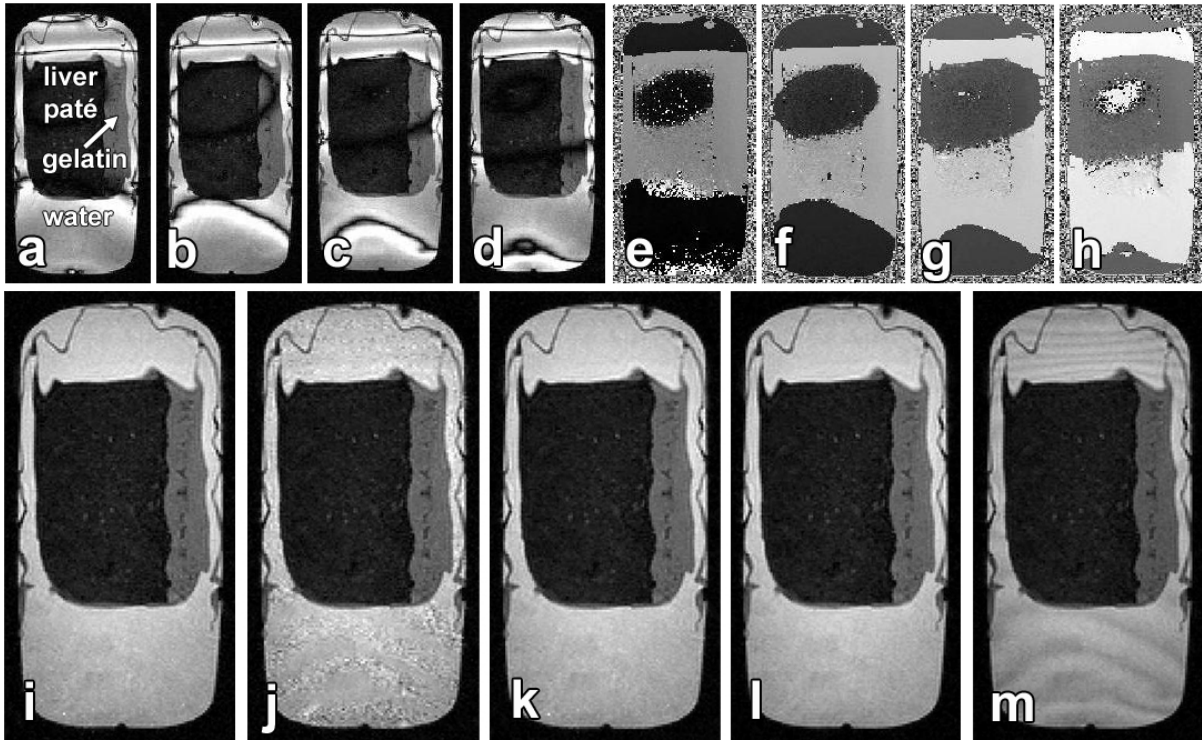


Figure 5.11 Demodulation of bSSFP CrCoMo/water/paté/gelatin phantom data. bSSFP magnitude & phase images phase cycled by $\Delta\theta =$ a)&e) 0° , b)&f) 90° , c)&g) 180° , and d)&h) 270° respectively. Reconstructions of the complex data include the i) geometric solution, j) algebraic solution, k) geometric-algebraic solution, l) geometric solution-guided weighted average, and m) complex sum.

Table 5.3 shows SNR calculations from the phantom images in Figure 5.11. The GS, GAS, and GS-WA perform well in water, where the CS' strong banding limits its SNR. The AS' low relative SNR in water is confirmed, though it marginally outperforms the GS in paté and gelatin. The GAS, GS-WA, and CS all yield relatively high SNR in paté and gelatin.

Phantom SNR			
	Water	Liver paté	Gelatin
GS	11.0	3.76	7.35
AS	7.93	3.84	7.49
GAS	11.1	4.08	7.75
GS-WA	11.1	4.02	8.11
CS	9.62	4.12	7.90

Table 5.3 The phantom signal-to-noise ratio (SNR) of bSSFP demodulation techniques SNR measured from the mean signal divided by its standard deviation in a relatively homogeneous region of interest is compared for various regions of the Figure 5.11 reconstructions.

Figure 5.12 a-d shows all four phase-cycled magnitude images of the in vivo thigh slice, and corresponding GS, AS, GAS, GS-WA, and CS reconstructions. All images have minimal or no banding, except where white arrows in Figure 5.12 h&i indicate residual banding near the implant in the GS-WA muscle and in the CS fat respectively. The AS appears to have similar performance to the GS, with slightly less graininess in low signal muscle regions.

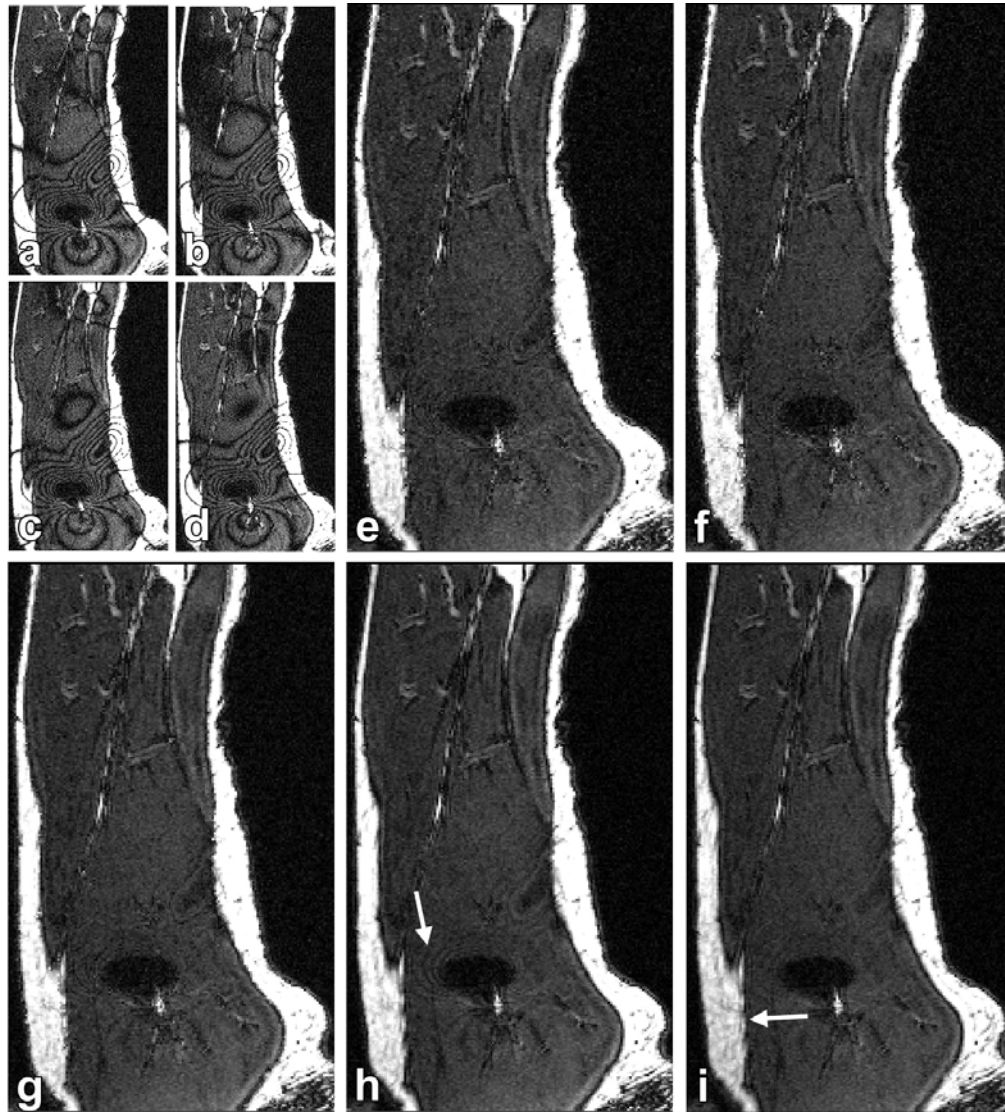


Figure 5.12 Demodulation of bSSFP in vivo thigh images. bSSFP magnitude images phase cycled by $\Delta\theta =$ a) 0° , b) 90° , c) 180° , and d) 270° with a nearby CrCoMo hip prosthesis. Reconstructions include the e) geometric solution, f) algebraic solution, g) weighted geometric-algebraic solution, h) geometric solution-guided weighted average, and i) complex sum. White arrows indicate residual banding.

5.3.6 Results: Performance Comparisons

TRE vs. variable bSSFP image noise for the GS, AS, GAS, and CS techniques is depicted in Figure 5.13a. The GS, AS, and GAS are fundamentally exact solutions that converge on zero error for zero image noise, whereas the CS is only an approximation of the centre-of-mass $\langle I \rangle$

and is error-prone without noise. However, at a certain noise level (4-7% noise) the CS begins to show comparable results as the AS and GS progressively break down. All techniques display increased error with greater noise; the GS, AS, and GAS show linear increases, while the CS increases in a nonlinear fashion as its averaging compounds the added noise in quadrature. The AS is the most sensitive to noise, while the GAS yields the least error regardless of noise level.

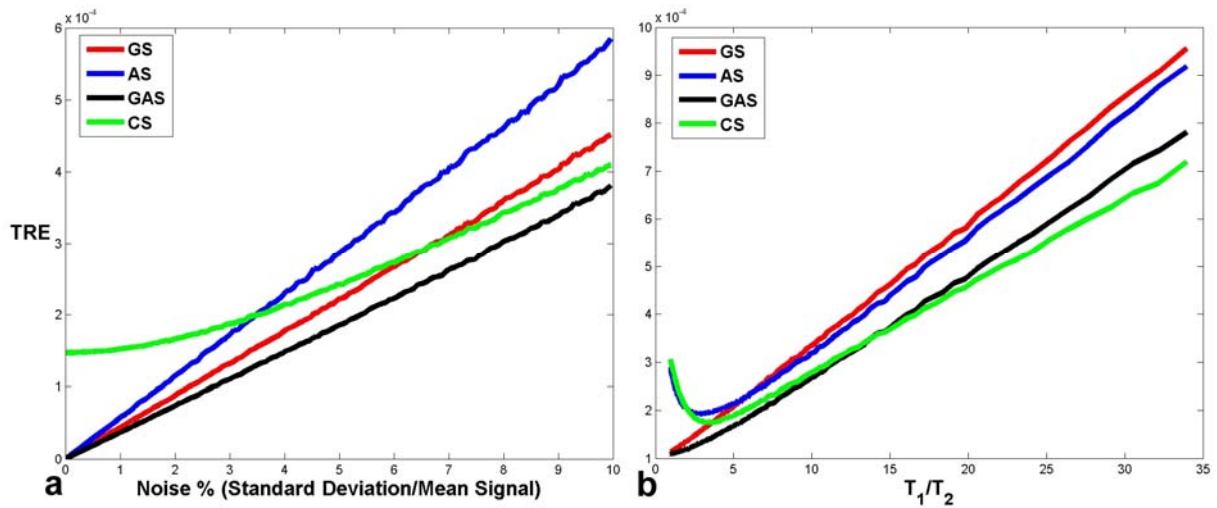


Figure 5.13 Total relative error (TRE) vs. image noise and T_1/T_2 . The TRE of the geometric solution (GS), algebraic solution (AS), geometric-algebraic solution (GAS), and complex sum (CS) is compared for a) variable noise and b) T_1/T_2 .

Figure 5.13b depicts the error of the GS, AS, GAS, and CS as the T_1/T_2 ratio is varied. The AS shows very high error when $T_1/T_2 < 4$, as is evident by its instability in the water of Figure 5.11d and in the simulations. The CS shares this nonlinear increase in error for the lower T_1/T_2 signal species, where residual banding is often seen. Each technique displays a general linear increase in TRE for higher T_1/T_2 species due to the correspondingly lower signal. The AS and GS exhibit very similar error for $T_1/T_2 > 4$, with the AS slightly lower. However, The GAS has consistently lower TRE than the GS and the AS. When $T_1/T_2 > \sim 13$, the CS has the lowest TRE. At these low signal species, the basic averaging of the CS proves optimal.

Table 5.4 summarizes the relative performance of the GS, AS, and GAS in terms of the above comparisons, reaffirming that all three techniques solve for the M parameter of Eq. [2.17], and that while the GS is invariant to real and imaginary component swapping of the original data prior to image reconstruction, the AS breaks down under such a procedure. The GAS is not complex in nature, and thus cannot have its data swapped prior to reconstruction.

	GS	AS	GAS
Complex swapping invariance?	Yes	No	N/A
TRE = 0 for noise = 0?	Yes	Yes	Yes
TRE vs. base image noise	Median	Maximum	Minimum
TRE vs. T_1/T_2 ratio	Linear	Nonlinear	Minimum

Table 5.4 Geometric solution, algebraic solution, and geometric-algebraic solution performance comparison. Techniques are compared in terms of their performance as a function of base image noise, T_1/T_2 ratio, and complex component swapping.

5.3.7 Discussion

Geometric and algebraic solutions that effectively demodulate bSSFP signal of θ -dependence for all tested tissue types have been proposed. Bands are eradicated, and both exactly yield M contrast when noiseless simulated data is employed. However, performance comparisons have indicated that they exhibit unique responses to noisy data. Computing both solutions for a given phase-cycled dataset is thus advantageous, as an optimal GAS mixture of the GS and AS with minimized noise variance may be identified without additional image acquisitions.

The GS shows generally less error than the AS due to several factors. Contrary to the AS, the GS is resilient to real/imaginary component swapping, and is not influenced by noise parallel to lines connecting data points with $\Delta\theta = \pi$. In contrast, the AS' many multiplicative operations yield large error propagation for strong signal, as is evident in water. The AS' very large error in these low T_1/T_2 regions inflates its TRE calculations.

Regardless, the AS is very useful in vivo, since most tissue has a relatively high T_1/T_2 ratio where the AS performs similarly to if not better than the GS.

Regardless of regional strengths and weaknesses of each technique, the GAS variance-weighted average yields an optimal variance-minimized combination of the GS and AS. Simulations and experimental data show that the GAS images consistently yield the least error and greatest SNR, and even approach the performance of the CS in high noise and low signal regions where averaging is powerful. The GS-WA also uses weighted averaging to ameliorate solution instabilities, but shows some evidence of difficulty correcting banding artifacts close to metals.

The GAS technique improves on the GS and AS, but image reconstructions near metals show residual signal loss and overlap. Other more robust techniques described in section 3.4 may thus be more appropriate if signal very close to metals is desired. Regardless, the GAS is an excellent option for imaging in generally inhomogeneous fields for bSSFP applications such as angiography and cardiac imaging.

The variance relationship between the GS and AS images and the GAS image is mirrored by the resistance relationship between two resistors and their effective resistance in parallel. Just as the effective resistance R_{eff} is always smaller than either of the component resistors R_1 or R_2 , so the final variance V_{GAS} should be less than either component variance V_{GS} or V_{AS} :

$$R_{eff} = \frac{R_1 R_2}{R_1 + R_2} \quad \rightarrow \quad V_{GAS}^2 = \frac{V_{GS}^2 V_{AS}^2}{V_{GS}^2 + V_{AS}^2} \quad [5.13]$$

However, the efficiency by which GAS minimizes variance depends upon the component images having identical base signal with uncorrelated noise. While performance comparisons, image and variance analysis and noise covariance calculations indicate that the component images have uncorrelated noise, a thorough statistical analysis is necessary for verification.

The use of regional signal variance calculations to estimate noise in images is contentious. The estimation of signal noise from the difference of an image and a smoothed version of itself is only an approximation of true signal noise. Additionally, variance measurements at tissue edges can be spuriously high. However, no pronounced edge errors are observed in GAS images. Since both the GS and AS generate the same base signal, a miscalculation of their noise values will only generate slightly higher noise content in a few GAS edge pixels that is difficult to observe.

Image fidelity was compared using the TRE from a gold standard for simulated data, and SNR from a region with consistent signal for experimental data. TRE is only possible in instances when a gold standard image is known, and includes all image artifacts such as noise, banding, and general signal modulation. Experimental SNR calculations do not properly assess gradual signal modulation. This is not a problem for GS, AS, and GAS reconstructions that have mostly noise error, but can cause CS SNR measurements to be misleading.

The GAS forms a robust method for bSSFP signal demodulation near metals and in generally inhomogeneous fields. It is comprised of the best of the GS and AS, and exhibits minimal error over all tested parameter variations. Additionally, the relative uniqueness of the GS and AS inspires further data reduction. The take-home message is that the GAS represents the chosen signal demodulation component for the proposed bSSFP metal artifact correction solution.

5.4 Shimming bSSFP for Signal Loss Recovery

Here a method is proposed to address signal loss stemming from metals in bSSFP imaging. A description of the biphasic signal cancellation mechanism is given, followed by a demonstration of how it may be countered to promote signal recovery. The imaging gradient is used to compensate strong field inhomogeneity through shimming, recovering heavily banded signal very close to a metal implant. This banding is ameliorated by a CS combination of two shimmed images that are relatively phase cycled. When the shimmed CS

is combined with a standard GS-WA demodulated image, more thorough bSSFP metal artifact correction in only moderately increased scan time may be realized.

5.4.1 Background

Some observations on signal loss may be made for selective excitation of an imaging block. Since Maxwell's equations require that the magnetic field and spin frequency distribution is continuous and differentiable, signal loss via displacements can only occur if there is also signal loss at the periphery of the block, or if signal overlap occurs within the block. Often neither feature is evident in 3D bSSFP, indicating that only intravoxel signal cancellation can be responsible for signal loss.

As discussed in section 3.3.3, intravoxel signal cancellation in bSSFP imaging near metals arises predominately from biphasic cancellation, in contrast with the general T_2^* dephasing experienced by other GRE sequences. The biphasic bSSFP frequency response phase profile shown in Figure 2.10b consists of predominately two phase values separated by π . If the field inhomogeneity changes in such a radical fashion that a considerable fraction of the frequency response profile exists within a single voxel, the opposed phase spins can yield signal cancellation in the corresponding complex averaged pixel signal.

Figure 5.14 demonstrates this partial volume effect. It shows full and zoomed-in regions of bSSFP magnitude and phase images of the CrCoMo/Lego phantom introduced in Figure 5.2. The dark signal loss areas of the magnitude zoom correspond to regions in the phase zoom where the phase alternates at each contiguous pixel. This implies that each pixel encompasses at least one-half of the period of the frequency response profile; it is here that biphasic signal cancellation should, and does, begin to occur.

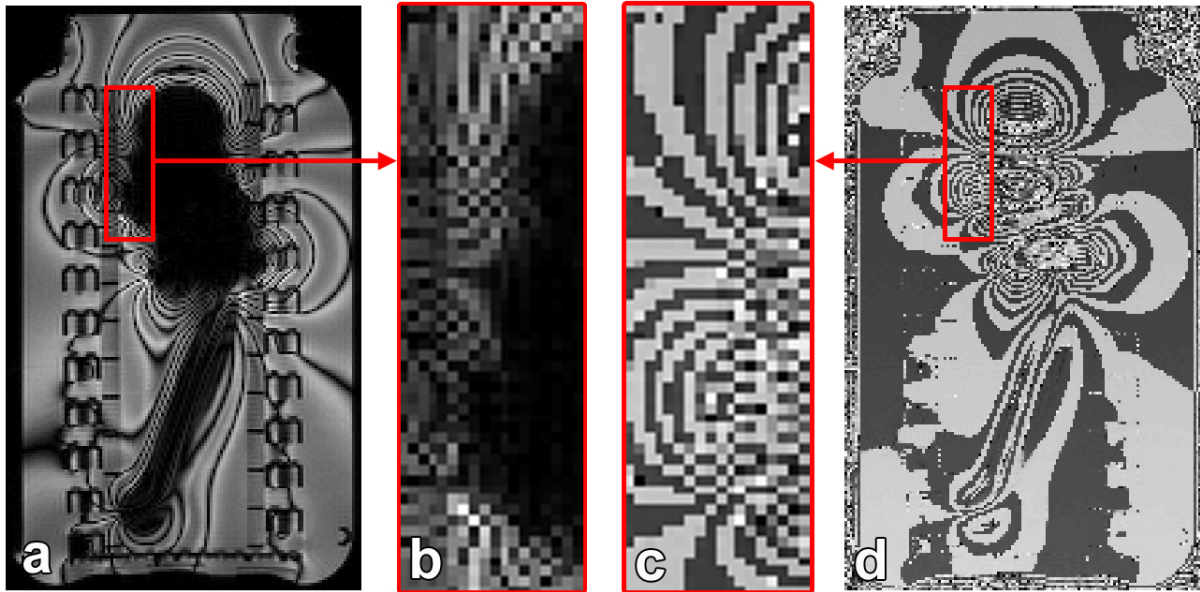


Figure 5.14 Biphasic signal cancellation in the CrCoMo/Lego phantom. a) bSSFP magnitude image and a b) zoom-in of the edge of its signal loss region. c) Zoom-in of the edge of the signal loss region of a d) bSSFP phase image.

If biphasic signal cancellation is responsible for signal loss in bSSFP images, the larger range of off-resonant frequencies in larger pixels should yield signal loss at lower local field inhomogeneities. The 256x152 matrix-size complex data of Figure 5.14 was reduced to half-resolution by complex averaging 2x2 pixel groups, yielding the 128x76 matrix size magnitude and phase images of Figure 5.15. The zoomed magnitude image shows more signal loss in the relatively homogeneous fields located further from the metal, where phase values now alternate in the larger contiguous pixels.

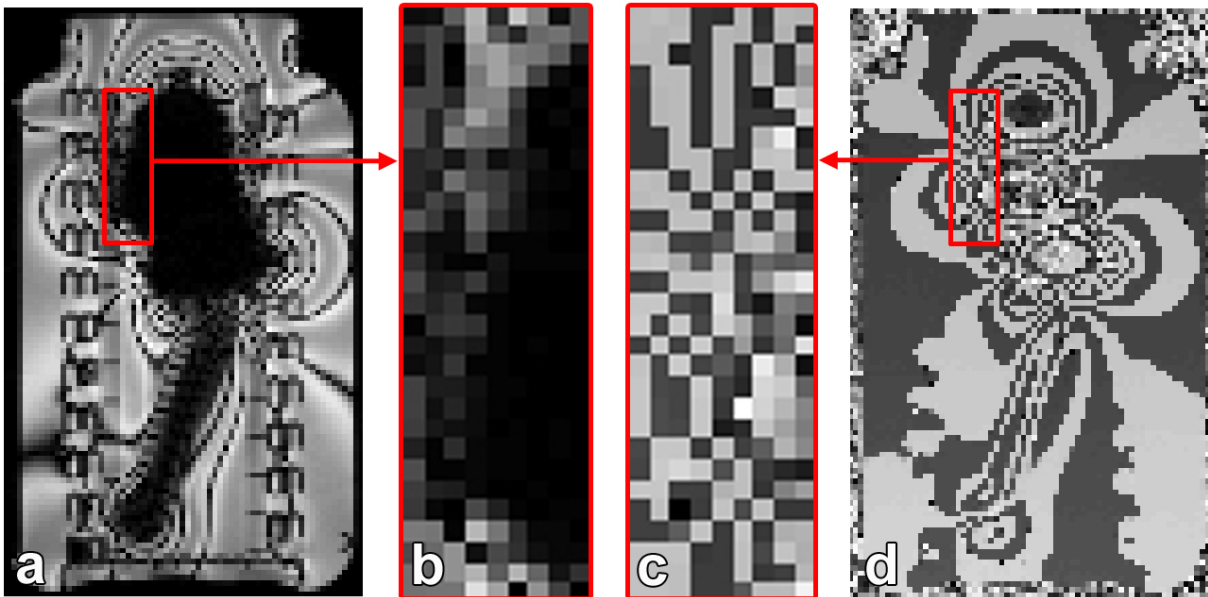


Figure 5.15 Biphasic signal cancellation in a low resolution phantom image. Complex bSSFP data shown in Figure 5.14 is rebinned from 256x152 matrix size to 128x76 matrix size by averaging 2x2 pixel groups. a) Magnitude, b) zoomed magnitude, c) zoomed phase, and d) phase is shown at half resolution.

The goal is to minimize the range of off-resonant frequencies within a pixel to avoid biphasic signal cancellation. This may be achieved by increasing the spatial resolution for a given FOV. However, higher spatial resolution requires larger gradients, which may be difficult to implement when bSSFP gradient strength is already maximized. The other option is to minimize a voxel's range of off-resonant spin frequencies by reducing the field variation.

Here imaging gradients apply first order shims to manually compensate strong field variations. Since recovered signal often has strong banding, $\Delta\theta = 0^\circ$ & 180° phase-cycled images are acquired of the same shim for subsequent combination and band suppression. This process should be repeated with various shimming orientations to account for the 3D nature of the magnetic field inhomogeneity. These acquisitions will lose signal in on-resonant regions, and so a regular GS-WA application is also executed. When all necessary images are acquired, they are combined to yield a bSSFP combination image with recovered signal loss.

5.4.2 Methods and Results

The CrCoMo/Lego phantom was imaged on the Siemens 1.5T scanner with a TrueFISP bSSFP sequence employing $\alpha = 40^\circ$, TR/TE = 4.2/2.1 ms, $BW_{RO} = 143$ kHz, 256/168/176 matrix size, and 1.17/1.17/1 mm voxel size along frequency/phase/slice directions. Four unshimmed datasets with $\Delta\theta = 0^\circ, 90^\circ, 180^\circ,$ and 270° respective phase cycling and two $-x$ shimmed datasets with $\Delta\theta = 0^\circ$ & 180° respective phase cycling were acquired. Both pulse sequence timing diagrams are depicted in Figure 5.16. The added $-x$ shim gradient is indicated in red, and other potential orientations for shims are indicated by dotted lines.

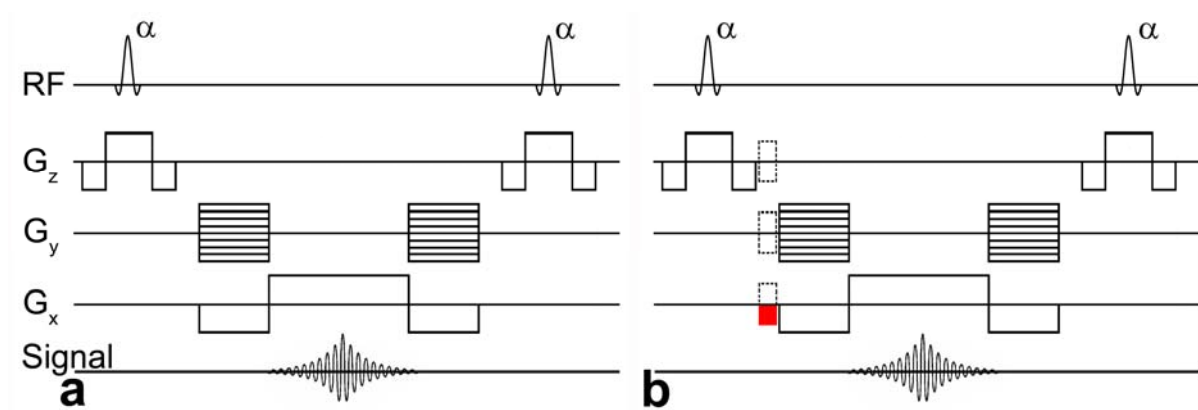


Figure 5.16 bSSFP pulse sequence timing diagrams with and without shim gradients. a) Regular unshimmed bSSFP pulse sequence, and b) gradient-shimmed bSSFP sequence with a $-x$ shim indicated in red. Other potential shim gradients are indicated by dotted lines.

$\Delta\theta = 0^\circ$ magnitude images of the shimmed and unshimmed datasets are shown in Figure 5.17 a&c respectively. The CS of the two shimmed datasets was computed and is shown in Figure 5.17b, and the GS-WA of the four unshimmed datasets was computed and is shown in Figure 5.17d. Finally, the maximum intensity of the $-x$ shimmed CS and the GS-WA was computed and is shown in Figure 5.17e. It is apparent that gradient shimming can recover bSSFP biphasic signal loss.

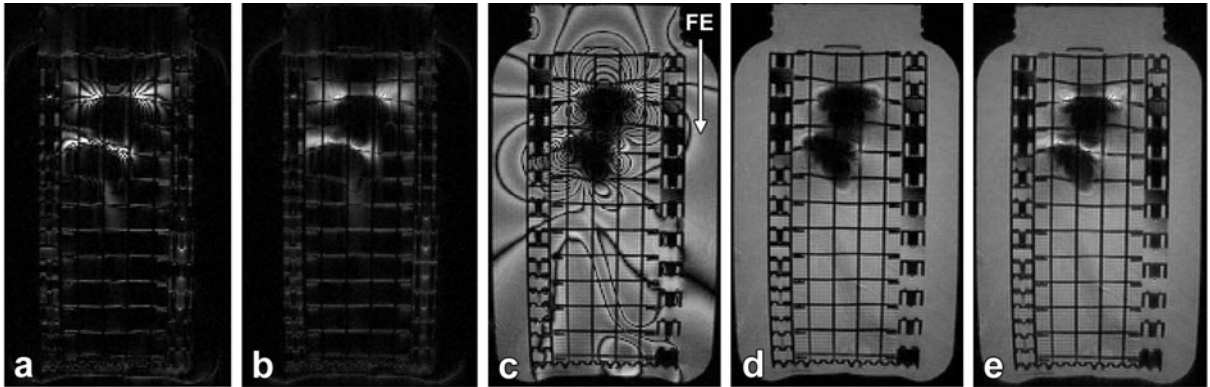


Figure 5.17 Shimming bSSFP for signal loss recovery in the CrCoMo/Lego phantom. a) $\Delta\theta = 0^\circ$, $-x$ shim bSSFP magnitude image, b) complex sum of $\Delta\theta = 0^\circ$ & $180^\circ - x$ shim images, c) $\Delta\theta = 0^\circ$ bSSFP regular magnitude image, and d) geometric solution-guided weighted average of four phase-cycled regular images. e) Maximum intensity of b) and d) yields a composite image with some signal recovered.

5.4.3 Discussion

The diagnostic viability of bSSFP gradient shimming for signal loss recovery near metals depends on optimizing spatial shim orientations, shim strengths, and phase cycles to achieve maximum signal recovery in minimal scan time. An optimized sample-independent relationship between shim orientations and phase cycles should be developed. Calculations of the local susceptibility effect can indicate the necessary shim strength. Finally, the sparsity of the recovered signal can be exploited using subsampling techniques such as compressed sensing (122,123) to minimize the shimmed data scan time.

The shimming method described has some similarities with MAVRIC technique described in section 3.4.7. While MAVRIC attempts to adjust the excitation frequency in order to track perturbed precession frequencies near metals, this procedure attempts to bring those perturbed precession frequencies in range of the excitation frequency with shims. Each technique requires a predetermined estimate of the off-resonant frequency range in order to maximize recovered signal. They also both combine a series of images with potentially overlapping signal, and thus may suffer from image combination artifacts. An advantage that MAVRIC has over shimming is that it is non-selective, and so its excitations have no concerns regarding spatial orientation.

Another similarity between MAVRIC and shimming is that both procedures cause previously on-resonant regions distant from a metal to become off-resonant, through excitation frequency offsets and shimming respectively. Both techniques thus require the acquisition of on-resonant images; here the GS-WA was computed from four unshimmed relatively phase-cycled images. A final corrected image was generated by combining the shimmed and unshimmed images.

The CS proved optimal for combination of the heavily banded shimmed images, where exact demodulation techniques have difficulty. Unfortunately, combining the CS of the shimmed data and the GS-WA of the unshimmed data yields some slight artifacts due to their different contrast. Regardless, more serious image combination artifacts will arise from the combination of variably oriented shims with overlapping signal.

This section demonstrated that it is possible to recover signal loss close to metals with bSSFP imaging. However, signal loss artifact correction comes at the cost of moderate increases in scan time. Optimization of the shimmed data acquisition will be necessary when devising a final solution that can compare to techniques such as MAVRIC and SEMAC. When combined with a signal demodulation technique such as GAS or GS-WA, the shimming method introduces an important step towards comprehensive metal artifact correction near metals with bSSFP imaging.

5.5 Using bSSFP Signal Ellipse Phase for Distortion Correction

Although bSSFP imaging shows minimal signs of distortion, some is evident in regions of high field inhomogeneity, as may be seen near the implant in Figure 5.17. Here a distortion correction technique is proposed that does not cost additional scan time. The idea is described, a proof of concept is demonstrated, and the viability of this supplementary technique is discussed.

5.5.1 Background

Distortion correction was demonstrated in section 4.1 to be possible via the generation of a phase evolution map that correlates with signal displacement. Unfortunately, the demodulation techniques described in this chapter are sensitive to phase alteration due to the requirement of predictable phase cycling.

However, there is a phase image that may provide the solution. Recall from section 2.5.3 that the bSSFP signal ellipse is rotated by an angle $\varphi = \theta/2$ according to the evolved off-resonant phase from $t = 0 \rightarrow TE$. The GS discussed in section 5.2 locates a characteristic point M in the bSSFP signal ellipse, meaning that the GS phase tracks the ellipse phase φ and directly reflects off-resonance. Contrary to the biphasic character of bSSFP signal, the GS has continuous phase.

Similar to PLACE phase images, the GS/ellipse phase φ may be used to remap distortion. Since Eq. [2.15] informs on the accumulated elliptical phase $\varphi = \Delta\omega \cdot TE$, and the frequency off-resonance $\Delta\omega$ leads to a FE pixel shift of $\Delta x_{pix} = \Delta\omega \cdot N_x / BW_{RO}$,

$$\Delta x_{pix} = \frac{\varphi \cdot N_x}{2\pi \cdot TE \cdot BW_{RO}} \quad [5.14]$$

The additional factor of 2π accounts for the expression of BW_{RO} in [Hz].

5.5.2 Methods and Results

Figure 5.18 demonstrates GS magnitude and phase images of the CrCoMo/Lego phantom acquired identically to section 5.2.5 except with $\alpha = 40^\circ$ and a 256/152/60 matrix size. It shows that the strong field inhomogeneity near the implant results in wrapping of the GS phase.

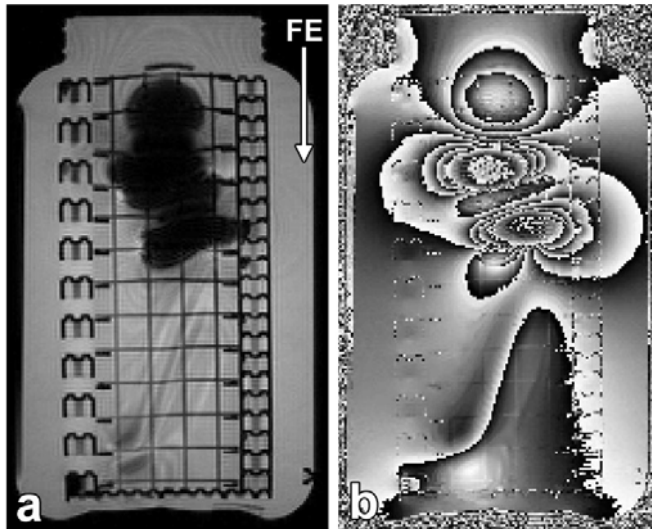


Figure 5.18 Geometric solution a) magnitude and b) phase of the CrCoMo/Lego phantom.

Figure 5.19 a&b show the GS phase and its unwrapped form using MATLAB's (The MathWorks, Natick, MA) "unwrap" algorithm for a region near the head of the implant depicted in Figure 5.18. The unwrapped phase was input into Eq. [5.14] to generate a displacement map. This map could then be used in a manner similar to PLACE and the other inhomogeneity mapping techniques described in sections 3.4.2 and 4.1.4.

Pixels in an expanded and slightly distorted GS magnitude map were mapped to their true locations with an expanded and smoothed displacement map. Data was rebinned to generate the GS demodulated image without distortion shown in Figure 5.19d; white arrows indicate the FE direction of distortion, and the regions of the polyethylene mesh that best demonstrate the distortion correction.

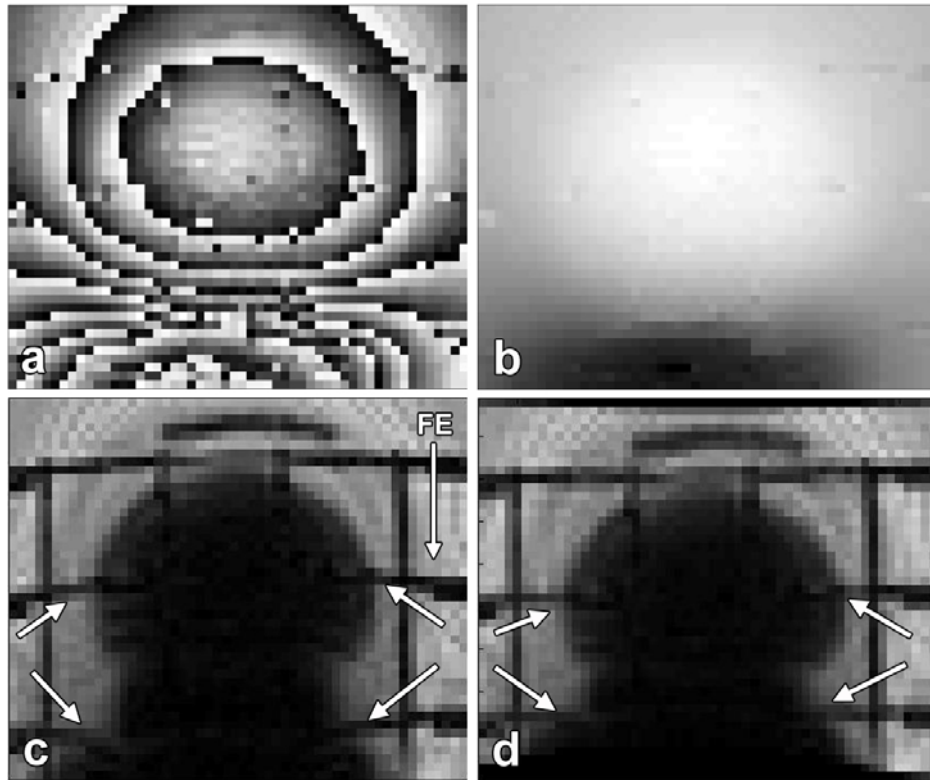


Figure 5.19 Ellipse phase distortion correction in the CrCoMo/Lego phantom. a) Geometric solution (GS) phase, b) MATLAB unwrapped GS phase, c) GS magnitude map, and d) remapped magnitude signal of c) using b) reduced FOV images of the prosthesis. Additional white arrows indicate distortion regions.

It is interesting to note that the lack of an accurate phase reference did not visibly deter the above correction. A zero phase reference was set distant to the implant; this might be expected to result in phase offset error and subsequently uncorrected distortion. However, the distortion appears corrected. The likely reason for this is that the accumulated phase in the region near the implant where distortions occur greatly exceeds the maximum offset error. Thus a relative measure of accumulated phase may be sufficient for correction.

Figure 5.19 demonstrates that the GS phase can achieve good distortion correction for bSSFP imaging near metals. No further data is required, aside from the four images acquired for signal demodulation. Unfortunately, the procedure required tweaking and manual adjustment of the phase unwrapping algorithm for optimal performance, which is not ideal for

procedural automation. Regardless, this method indicates that residual in-plane distortions in bSSFP images near metals can be corrected at no added scan time cost.

5.6 Imaging Near Metals with bSSFP Discussion

This chapter validates bSSFP's utility for imaging near metals, and demonstrates that it offers flexibility in the balance of scan time and image fidelity. For very fast imaging with accuracy in all regions save for immediately next to the implant, GAS image demodulation requires only four relatively RF phase-cycled images. Any residual distortion can be corrected using the GS phase without excess data acquisition. If signal closer to metals is desired, additional shimmed images may be acquired to compensate field inhomogeneity and recover lost signal, at the cost of increased scan time.

However, there are several non-inhomogeneity artifacts that should be considered when the aforementioned bSSFP techniques are employed. Dark flow artifacts arise if spins move through inhomogeneous fields that disturb their steady state, and then cross through signal null regions (106,124). The discrete and powerful PE gradients can induce eddy currents in metals and subsequent error in the RF pulse phase (125,126). Motion during multiple phase-cycled sequential acquisitions can cause unpredictability in component images (115,127). All of these mechanisms can muddle the described signal demodulation schemes, their corresponding debanding capabilities, and even yield oscillating steady states (128,129).

Additionally, biphasic intravoxel signal loss artifacts are not the only partial volume artifacts from which bSSFP suffers. Multiple intravoxel substructures such as lipids, proteins, iron carriers, and molecules of variable magnetic susceptibility can lead to further signal cancellation and profile asymmetry (20,130,131). While studies here have not indicated that this may be a problem, it is conceivable that the proposed signal demodulation techniques will have trouble in complicated tissue environments.

The described bSSFP artifact corrections may also be altered to accommodate contrast variation and reductions in scan time. This chapter outlined bSSFP demodulation techniques

that achieve M contrast as defined in Eq. [2.17], which is unique relative to SE and even standard bSSFP contrast. Other characteristic bSSFP signal points such as the centre-of-mass $\langle I \rangle$ could offer just as suitable signal demodulation, were it possible to calculate them exactly. As mentioned earlier, magnetization preparation can also be employed to enhance contrast. Scan time reduction is also feasible using parallel imaging (132,133), compressed sensing (122,123), or other methods such as the partial Fourier technique introduced next chapter.

The proposed work is at present unable to generate images with as comprehensive artifact correction as techniques such as MAVRIC, SEMAC, and SPI. However, there are signs that with further development a very efficient method can be generated which yields comparable correction capabilities. If the sequence is optimized temporally, it may prove useful for time-sensitive imaging near metals, such as for image-guided surgery. At present, the proposed bSSFP methods can be of value in bSSFP applications such as angiography and cardiac imaging when the magnetic field is inhomogeneous.

5.7 Summary

The results of this chapter indicate that bSSFP may soon generate diagnostically viable images near metals with both speed and flexibility. Complete signal demodulation and debanding was achieved in two unique ways. This inspired a higher performance composite solution that easily surpasses the intermittently successful multi-acquisitions methods listed in section 3.4.10. Additionally, corrections of residual distortion using GS phase data did not require additional acquisitions, and with further scans signal loss was recovered through field inhomogeneity compensation. This procedure may be customized to balance artifact correction and scan time requirements, indicating the utility of employing bSSFP imaging near metals.

Chapter 6: Reducing Scan Time of bSSFP Signal Off-Resonance Demodulation

The existence of two independent four-image solutions to bSSFP signal modulation indicates inherent solution redundancy. This inspires demodulation efforts using less data, which would be advantageous for time constrained procedures such as dynamic and motion-sensitive imaging. Two techniques are demonstrated that exploit the fact that two relatively phase-cycled bSSFP images can yield a linear solution; one method shows that a low resolution GS is sufficient to guide a weighted solution, and the other method indicates that a two image algebraic solution can achieve respectable debanding.

6.1 Geometric XS-Guided Solution for Reduced-Time Demodulation

This section introduces the first reduced scan time bSSFP demodulation technique, essentially a scaled down version of the GS-WA. A downsampled GS is computed to guide a linear weighted average of two full datasets for both simulated and experimental scenarios. The degree of downsampling is varied to determine the optimal data reduction factor that does not significantly sacrifice demodulation capabilities. Conclusions are made on the relative performance and clinical viability of the scan time reduction technique.

6.1.1 Background

Section 5.2.2 explained that the demodulated solution M is a weighted average of complex pixel values from two images relatively phase cycled by $\Delta\theta = 180^\circ$. The GS-WA weights were found in section 5.2.3 by analytically minimizing the regional differential energy (E) of such a weighted average from the four image GS. This begs the question: since the solution is confined to a single line in the complex plane, is it absolutely necessary to acquire the full four image GS to guide the solution? Here a downsampled GS is employed as a guide to limit the total acquisition to two full and two partial datasets, dubbed the XGS cross-guided-solution (134).

6.1.2 Methods

The simulated data from Figure 5.10 and a peripheral slice from the CrCoMo/Lego phantom dataset of Figure 5.4 were employed for these tests. Figure 6.1 shows the workflow for both simulated and experimental data. Four datasets with $\Delta\theta = 0^\circ, 90^\circ, 180^\circ,$ and 270° respective phase cycling are truncated in k-space to retain only the central phase encoded data. Ringing artifacts due to the subsequent k-space discontinuity are suppressed by low-pass filtering with a 1D MATLAB Hamming window extending across the retained k-space phase encodes. This data is zero padded and then inverse Fourier transformed. The output low resolution data is input pixel-by-pixel into Eq. [5.2] to generate a low resolution GS.

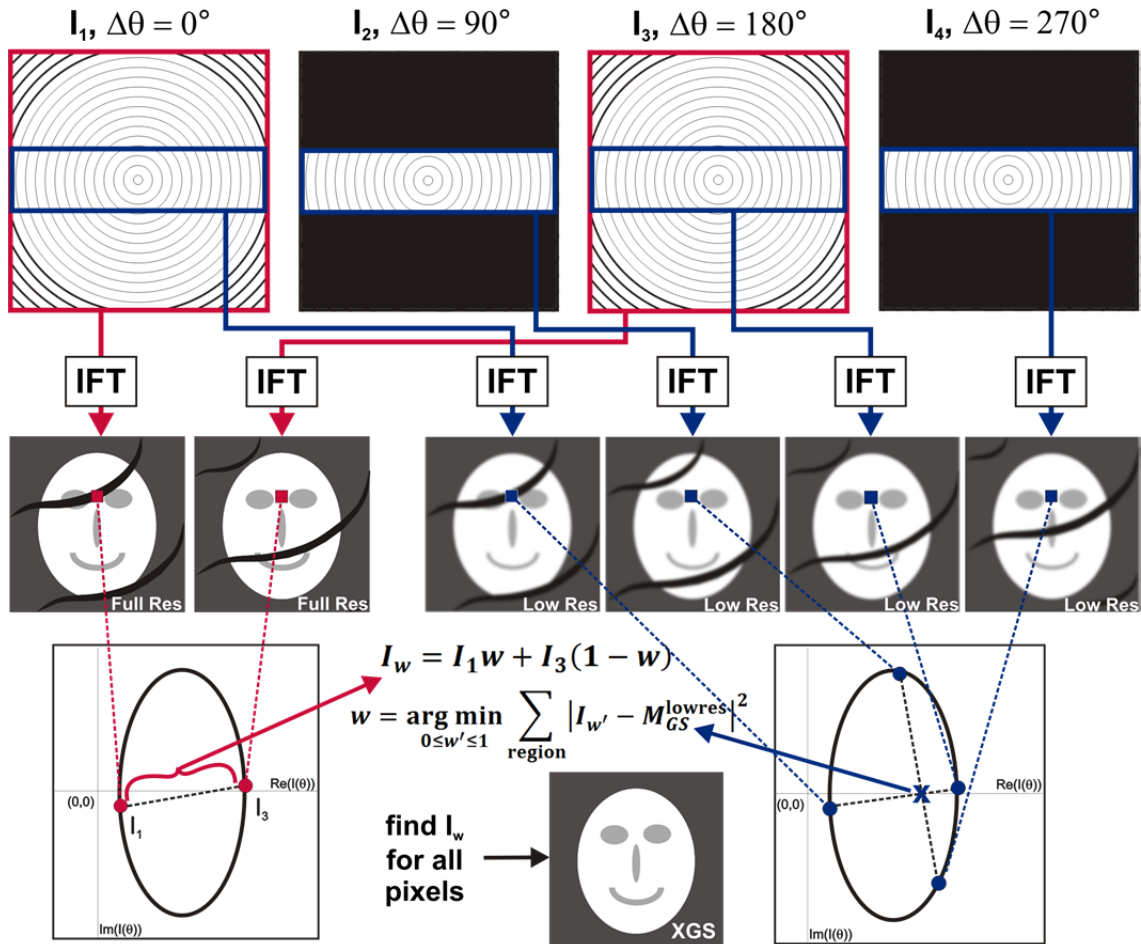


Figure 6.1 Workflow for the XS-guided solution (XGS). Four phase-cycled datasets are subsampled, inverse Fourier transformed, and a low resolution geometric solution (GS) computed in blue. A weighted average I_w of two full datasets is detailed in red. Weights w are calculated by regionally minimizing the complex deviation from the low resolution GS.

The machinery of section 5.2.3 was executed to compute the pixel-by-pixel demodulated weighted average of two full $\Delta\theta = 0^\circ$ & 180° images. With a square region of 5×5 pixels, the low resolution GS guided the E minimization to determine the proper weight w for a central pixel via Eq. [5.7], and the solution image pixel was formed by inputting the weights into Eq. [5.3]. This was iterated for all pixels to generate the final image.

Variable amounts of GS downsampling were tested, and for each linear weighted solution image the TRE from Eq. [5.12] was computed from the gold standard I_{gold} , which is the known value M for simulated data and the full GS for experimental phantom data. Several CS images were generated for comparison: $CS_{N=2}$ with $\Delta\theta = 0^\circ/180^\circ$, $CS_{N=3}$ with $\Delta\theta = 0^\circ/120^\circ/240^\circ$, and $CS_{N=4}$ with $\Delta\theta = 0^\circ/90^\circ/180^\circ/270^\circ$; their I_{gold} for simulated data is given by the centre-of-mass $\langle I \rangle$ defined in Eq. [2.24], equivalent to $CS_{N=\infty}$.

6.1.3 Results

Figure 6.2 and Figure 6.3 depict one full $\Delta\theta = 0^\circ$ bSSFP magnitude image, the $CS_{N=3}$, and the XGS using 25% GS k-space coverage for simulated and phantom data respectively. Using only $2 + 1/4 + 1/4 = 2.5$ datasets, the XGS significantly diminishes signal modulation and bands relative to the $CS_{N=3}$. However, slight evidence of banding remains.

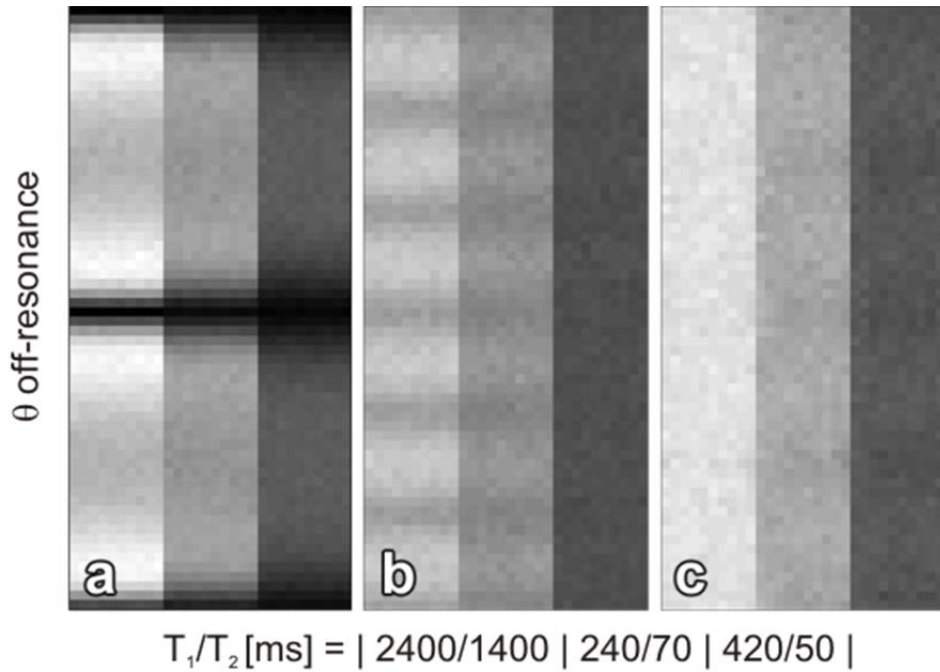


Figure 6.2 XS-guided solution (XGS) of “tri-tissue” bSSFP simulated data. “Tissues” with $T_1/T_2 = 2400/1400$, $240/70$, and $420/50$ are delimited horizontally, and θ is varied from -2π to 2π vertically. a) $\Delta\theta = 0^\circ$ bSSFP magnitude image, b) $N=3$ complex sum, and c) XGS guided by 25% XS k-space coverage.

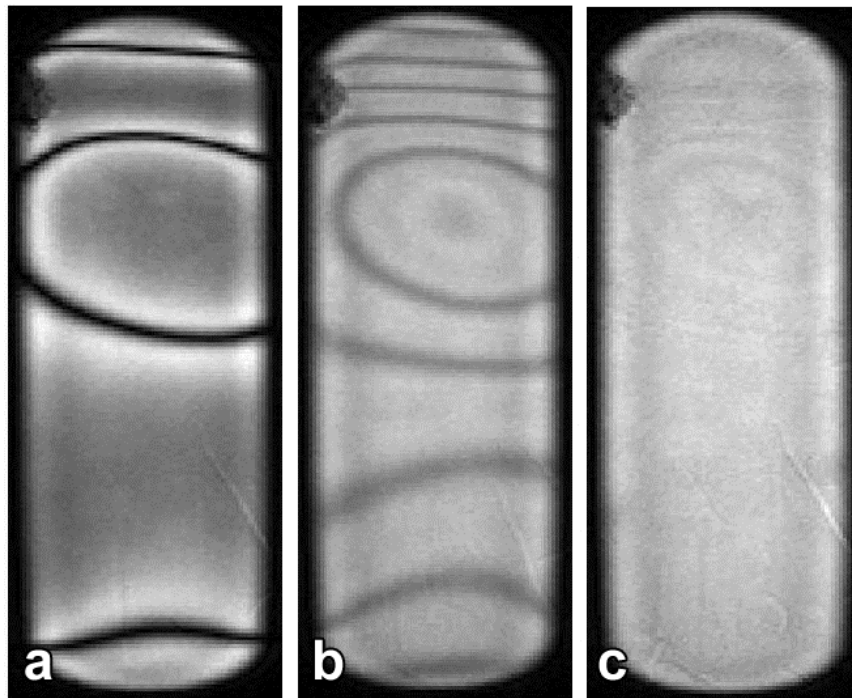


Figure 6.3 XS-guided solution (XGS) of bSSFP CrCoMo/Lego phantom data. a) $\Delta\theta = 0^\circ$ bSSFP magnitude image from peripheral water region, b) $N=3$ complex sum, and c) XGS guided by 25% XS k-space coverage.

Figure 6.4 plots the TRE of the XGS vs. the subsampled GS k-space coverage for a) simulated and b) phantom data. The $CS_{N=2}$, $CS_{N=3}$, and $CS_{N=4}$ error values are plotted at comparable scan times for the simulated data; since the XGS consists of two full scans plus two low resolution scans, 0% coverage $\approx N = 2$ scans, 50% coverage $\approx N = 3$ scans, and 100% coverage $\approx N = 4$ scans. Both plots show that only 25% of k-space (~ 2.5 scans) is needed for the GS to guide the XGS to minimal deviation from the gold standard relative to any CS method.

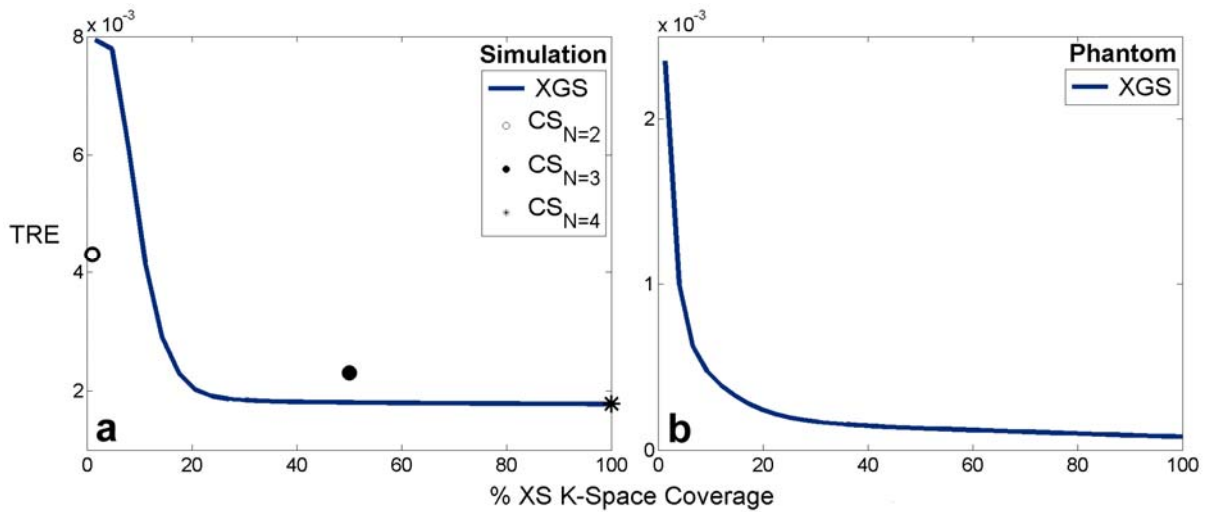


Figure 6.4 XS-guided solution (XGS) total relative error (TRE) curves for varied geometric cross-solution k-space coverage. a) Simulated data includes complex sum (CS) values with equal scan time requirements, and b) phantom data similar to Figure 6.2 and Figure 6.3 respectively.

6.1.4 Discussion

Only $\sim 25\%$ of two of the four datasets used in the XGS is needed to achieve marginally increased error relative to a full four image GS; that is, only ~ 2.5 images are needed for almost complete signal demodulation. The CS in contrast experiences a considerable increase in error as the number of datasets is reduced. This represents an excellent opportunity for accelerated bSSFP band correction.

However, the error analysis used to make these observations has limitations. Both the “tri-tissue” simulated data and the water phantom employed in constructing the error curves have spatially consistent signal intensity; it is possible that rapid spatial variations in tissue type

and signal intensity would be poorly reflected by the low resolution GS, yielding increased reconstruction error. Additionally, error calculations could not be made for the CS of experimental data, as CS error requires knowledge of the gold standard $CS_{N=\infty}$, and an infinite number of experimental images are difficult to acquire! However, an error calculation may still be made for the XGS of experimental data. Since the XGS seeks to emulate the full GS, the full GS represents a suitable gold standard.

While the XGS technique essentially only requires 2.5 datasets in order to achieve good banding correction, they come in the form of two full and two partial datasets. Thus four separate datasets must be sequentially acquired, which may pose difficulties for motion-sensitive imaging.

In conclusion, the XGS provides an excellent opportunity for reducing scan time without sacrificing significant bSSFP signal demodulation capabilities. The requirement to acquire four separate datasets may not be optimal for some motion-sensitive applications, but the technique provides a resourceful tool with surprisingly high performance results.

6.2 Algebraically Weighted Solution for Reduced-Time Demodulation

A two image algebraic solution for bSSFP signal demodulation near metals is presented to satisfy very fast imaging requirements. A θ -independent algebraic solution (AS2) is derived from two images with $\Delta\theta = 0^\circ$ & 180° respective phase cycling, and a second pass algebraically weighted solution (AWS) is then computed. The AWS is compared with a $CS_{N=2}$ of the same data, and its merits and drawbacks are discussed.

6.2.1 Theory

The AWS lacks the insensitivity to global rotation of the bSSFP signal ellipse exhibited by the other described demodulation solutions, and so the $\exp(-i \cdot \theta/2)$ term in Eq. [2.16] must be retained in the base signal expressions. The $\exp(-TE/T_2)$ dephasing term may still

be ignored as it only diminishes all signal components by an amount independent of the θ off-resonance value. Eq. [2.16] may be expressed as

$$I(\theta + \Delta\theta) = M \frac{1 - ae^{i(\theta+\Delta\theta)}}{1 - b \cos(\theta + \Delta\theta)} e^{-i\frac{\theta}{2}} \quad [6.1]$$

If two phase-cycled complex bSSFP signal equations are given by $I_1 = (\theta)$ and $I_2 = (\theta + \pi)$

$$I_2 = M \frac{1 \mp ae^{i\theta}}{1 \mp b \cos \theta} e^{-i\frac{\theta}{2}} \quad [6.2]$$

Expressing Eq. [6.2] in real and imaginary components yields

$$\begin{aligned} x_1 &= \frac{M(1-a) \cos \frac{\theta}{2}}{1-b \cos \theta} & y_1 &= \frac{M(1+a) \sin \frac{\theta}{2}}{1-b \cos \theta} \\ x_2 &= \frac{M(1+a) \cos \frac{\theta}{2}}{1+b \cos \theta} & y_2 &= \frac{M(1-a) \sin \frac{\theta}{2}}{1-b \cos \theta} \end{aligned} \quad [6.3]$$

Equation [6.3] lists four unique equations in terms of the four parameters M , a , b , and θ , and thus represents a solvable system. The AS2 was found by solving for the θ -independent magnetization parameter M in terms of x_1 , x_2 , y_1 , and y_2 using Maple™

$$\begin{aligned} M_{\frac{1}{2}} &= \frac{\sqrt{x_1 x_2 + y_1 y_2} (x_2 y_1 + \sqrt{x_1 x_2 y_1 y_2})}{\pm (y_1 \sqrt{x_1 x_2} + x_2 \sqrt{y_1 y_2})} \\ M_{\frac{3}{4}} &= \frac{\sqrt{x_1 x_2 + y_1 y_2} (x_2 y_1 - \sqrt{x_1 x_2 y_1 y_2})}{\pm (y_1 \sqrt{x_1 x_2} - x_2 \sqrt{y_1 y_2})} \end{aligned} \quad [6.4]$$

There are four solutions for M , although as shall be discussed, only one is correct for any given image pixel.

6.2.2 Methods

The solution was applied to two simulated and two MR phantom images with $\Delta\theta_{1/2} = 0^\circ/180^\circ$, $\alpha = 40^\circ$, and $TR/TE = 4.2/2.1$ ms. Noisy simulated data is identical to the “tri-tissue” data visualized in Figure 5.10. Experimental phantom data was identical to the dataset acquired from the CrCoMo/Lego/paté/gelatin/water phantom of section 5.3, except a more peripheral slice within the Lego was chosen for this particular study.

It was necessary to correct for spatial drift and offset due to the phase sensitivity of the AS2. A flattened phase map was first generated by doubling the phase of the original biphasic images. An approximation of the phase offset and drift was made, and this was compensated in the original images. The result was that the two images had phase values of $(0, \pi)$ and $(\pm\pi/2)$ respectively, which aided in overall solution performance.

Data was processed pixel-by-pixel: image real parts $x_{1/2}$ and imaginary parts $y_{1/2}$ were input into Eq. [6.4] to yield four AS2 solution images. The four images were then sifted for feasibility: on a pixel-by-pixel basis, the positive AS2 value that did not exceed the magnitude of both of the two input image pixels was chosen for the sifted AS2. A MATLAB golden section numerical minimization of the regional least squares residual between a weighted average of the original data and the sifted AS2 yielded the AWS.

TRE from Eq. [5.12] was calculated for the simulated data: for the AWS, the gold standard was the known M data in Figure 5.10i, and for the $CS_{N=2}$, the gold standard was the $CS_{N=\infty}$ of Eq. [2.24].

6.2.3 Results and Discussion

Figure 6.5 depicts the $\Delta\theta = 0^\circ$ simulated image magnitude, the AS2, sifted AS2, AWS, and $CS_{N=2}$. The $CS_{N=2}$ has residual bands in all three “tissues”, while the AWS only has bands in the leftmost “tissue”. TRE values are listed in red, indicating that the AWS has consistently less deviation from the gold standard than the $CS_{N=2}$ for each “tissue” tested.

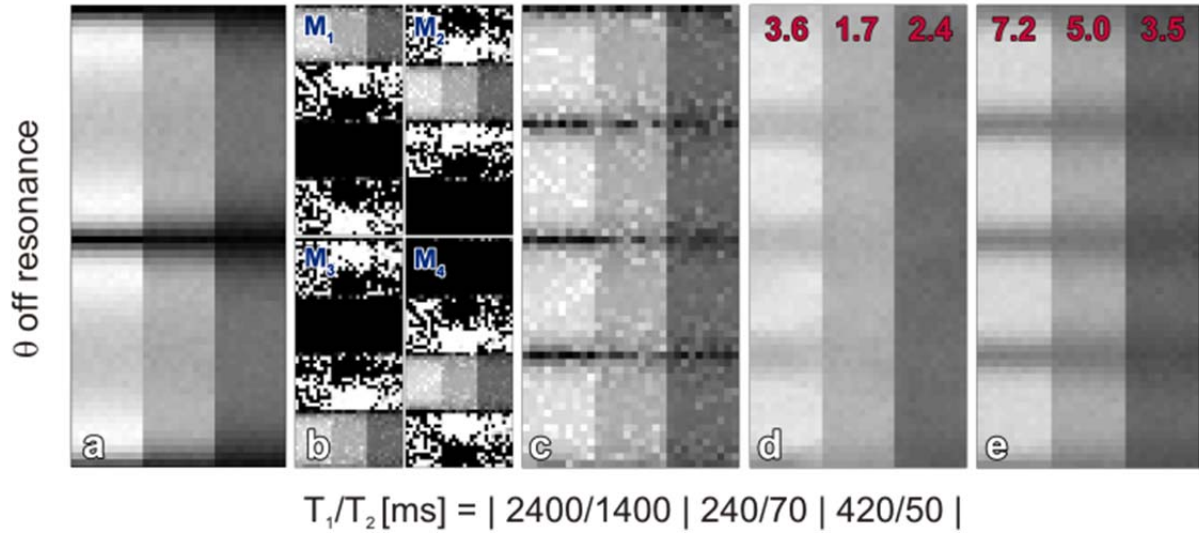


Figure 6.5 Algebraic weighted solution (AWS) of segmented “tri-tissue” bSSFP simulated data. $T_1/T_2 = 2400/1400, 240/70,$ and $420/ 50$ “tissue” regions are delimited horizontally, and θ is varied from -2π to 2π vertically. a) $\Delta\theta = 0^\circ$ magnitude image, b) AS2 algebraic solutions $M_1/M_2/M_3/M_4$ of $\Delta\theta = 0^\circ$ & 180° images, c) sifted AS2, d) AWS, and e) $N=2$ complex sum. Total relative error values are given in red.

Figure 6.6 shows the $\Delta\theta = 0^\circ$ bSSFP phantom magnitude image, the AS2, AWS, and $CS_{N=2}$. While the AWS shows considerable band reduction relative to the $CS_{N=2}$, it still suffers from some residual signal modulation in both simulated and phantom images.

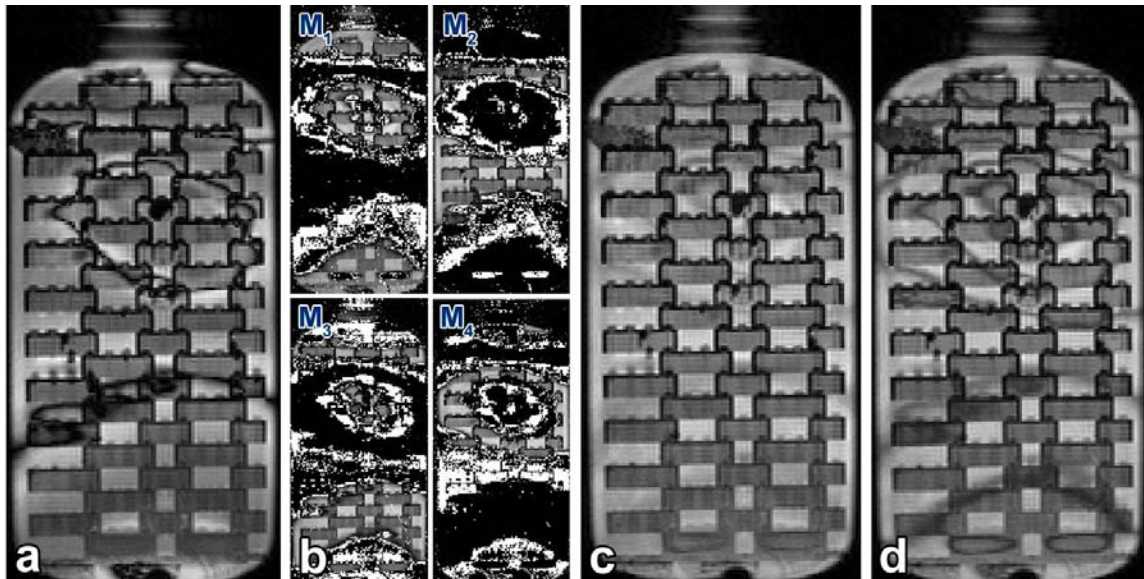


Figure 6.6 Algebraic weighted solution (AWS) of bSSFP CrCoMo/Lego phantom data. a) $\Delta\theta = 0^\circ$ magnitude image, b) AS2 algebraic solutions $M_1/M_2/M_3/M_4$ of $\Delta\theta = 0^\circ$ & 180° images, c) AWS, and d) $N=2$ complex sum.

The AWS represents a two image solution to the bSSFP banding problem. It has improved performance relative to the $CS_{N=2}$, and represents a valuable possibility for bSSFP imaging in inhomogeneous fields when imaging time must be constrained. This can be a viable option for imaging in motion-sensitive scenarios.

However, the AWS has residual banding, and requires phase correction, sifting of the AS2 four-part solution, and post-processing via a regional numerical optimization routine for predictable θ -demodulation. It is thus conceivable that other two image solutions such as a CS-guided or MI-guided weighted average could usurp this technique's performance and reliability. Alternatively, an exact three image solution may prove to be the best use of research and imaging time.

In conclusion, the AWS provides respectable two-image signal demodulation that may be desirable for certain time-sensitive clinical scenarios involving motion. However, there may be more optimal two or three image methods of bSSFP signal demodulation that can be devised.

6.3 Summary

The inherent redundancy of two independent four image solutions to the bSSFP signal modulation problem inspired efforts using less data. Two techniques were developed that exploited the fact that two relatively phase-cycled bSSFP images can yield a linear weighted solution to achieve demodulation with reduced data. These techniques could be useful for very time-sensitive procedures such as imaging in regions with motion. However, better techniques may be on the horizon, including exact methods requiring less data, parallel imaging (132,133) schemes, and compressed sensing (122,123) applications.

Chapter 7: Conclusion

The purpose of this study was to develop methods of imaging near metals in clinically feasible scan times. The bSSFP technique was discovered to be an efficient, high-fidelity method of imaging in inhomogeneous magnetic fields with unique contrast. Off-resonance banding artifacts and general signal modulation were eliminated with two unique methods. Performance improvements that employ linear averaging and variance-weighted combinations were proposed. A technique for signal loss recovery was developed for resolving biphasic intravoxel signal cancellation using shim gradients; maturation of this technique will facilitate bSSFP imaging in regions proximal to metals. A method inspired by previously developed techniques for distortion elimination in spin-echo images was developed for correction of remnant bSSFP distortion artifacts. Finally, two scan time minimization methods were formulated to reduce the amount of data required for bSSFP signal demodulation.

Imaging near metals in MRI has seen a large amount of research in recent years; many techniques offer near-comprehensive artifact correction, while others attempt to make corrections in short scan time, but to date none can boast to do both. Here an optimal balance of artifact correction and scan time parsimony is possible, and further improvements could facilitate time-constrained imaging applications such as dynamic or motion-sensitive imaging near metals. The use of bSSFP also offers unique contrast, which can be desirable in instances where clinicians desire T_1/T_2 ratio differentiation.

The proposed metal artifact correction techniques have some drawbacks. Spin-echo contrast is often more clinically desirable than bSSFP contrast. Phase-cycled bSSFP images must be sequentially acquired, which can create problems if there is motion. The proposed signal recovery procedure requires prediction of the field inhomogeneity prior to determination of shim gradient strength, and scan time sacrifices are necessary to recover signal loss. Finally, the residual distortion correction employs phase unwrapping for successful application, which is undesirable.

7.1 Future Work

There is thus still much work needed to bring bSSFP imaging near metals to full maturity. The efforts can be categorized in terms of scan time reduction and metal artifact reduction.

7.1.1 Scan Time Reduction

The existence of two unique and exact four-image solutions to bSSFP banding indicates redundancy. This has inspired the search for techniques using less than four datasets. This study discussed two possible methods, but optimally an exact solution using two or three datasets can be developed. Efforts to interleave steady state datasets are also gaining traction (135); this could help reduce scan time and alleviate motion artifacts associated with sequential acquisitions. Other efforts to reduce required data for corrections may include more sophisticated subsampling and post-processing methods.

7.1.2 Comprehensive bSSFP Metal Artifact Correction

Final debanded images showed that some signal loss and distortion still exists in bSSFP images containing metals. Gradient shimming has shown promise for signal recovery, but optimization of shim orientation and strength is essential. Alternatively, higher resolution imaging can achieve the same feat; since signal loss regions only exist in regions near metal, a technique with spatially variable resolution such as Locally Focused Tomography (136) can be developed to resolve strong field variations with minimal scan time sacrifices. Finally, efforts will be made to devise a method for residual distortion elimination in bSSFP images that does not require phase unwrapping.

Bibliography

1. Xiang Q-S. Introduction to Magnetic Resonance Imaging, UBC-PHYS 542 Class Notes. 2004.
2. Lauterbur PC. Image Formation by Induced Local Interactions: Examples Employing Nuclear Magnetic Resonance. *Nature* 1973;242:190-191.
3. Edelstein WA, Hutchison JM, Johnson G, Redpath T. Spin warp NMR imaging and applications to human whole-body imaging. *Phys Med Biol* 1980;25:751-756.
4. Kumar A, Welte D, Ernst R. Imaging of macroscopic objects by NMR Fourier zeugmatography. *Naturwissenschaften* 1975;62:34-34.
5. Bjarnason TA, Laule C, McCreary CR. Introduction to Quantitative T2 with emphasis on Medical Imaging. In: Bjarnason TA, editor: Lulu.com; 2011.
6. Hahn EL. Spin Echoes. *Physical Review* 1950;77(5):746-746.
7. Carr HY, Purcell EM. Effects of Diffusion on Free Precession in Nuclear Magnetic Resonance Experiments. *Physical Review* 1954;94(3):630-638.
8. Meiboom S, Gill D. Modified Spin-Echo Method for Measuring Nuclear Relaxation Times. *Rev Sci Instrum* 1958;29(8):688-691.
9. Hennig J, Nauerth A, Friedburg H. Rare Imaging - A Fast Imaging Method for Clinical MR. *Magn Reson Med* 1986;3(6):823-833.
10. Frahm J, Haase A, Matthaei D. Rapid NMR Imaging of Dynamic Processes Using the FLASH Technique. *Magn Reson Med* 1986;3(2):321-327.
11. Posse S, Aue WP. Susceptibility Artifacts in Spin-echo and Gradient-echo Imaging. *J Magn Reson* 1990;88(3):473-492.
12. Frahm J, Merboldt K-D, Hänicke W. Direct FLASH MR imaging of magnetic field inhomogeneities by gradient compensation. *Magn Reson Med* 1988;6:474-480.
13. Bernstein MA, Grgic M, Brosnan TJ, Pelc NJ. Reconstructions of phase contrast, phased array multicoil data. *Magn Reson Med* 1994;32:330-334.

14. Buxton RB, Fisel CR, Chien D, Brady TJ. Signal Intensity in Fast NMR Imaging with Short Repetition Times. *J Magn Reson* 1989;83(3):576-585.
15. Scheffler K, Lehnhardt S. Principles and applications of balanced SSFP techniques. *Eur Radiol* 2003;13:2409-2418.
16. Carr H. Steady-state free precession in nuclear magnetic resonance. *Physical Review* 1958;112:1693-1701.
17. Ernst RR, Anderson WA. Application of Fourier Transform Spectroscopy to Magnetic Resonance. *Rev Sci Instrum* 1966;37:93.
18. Freeman R, Hill H. Phase and intensity anomalies in fourier transform NMR. *J Magn Reson* 1971;4:366-383.
19. Oppelt A, Graumann R, Barfuss H, Fischer H, Hartl W, Schajor W. FISP: a new fast MRI sequence. *Electromedica* 1986;54:15-18.
20. Scheffler K, Hennig J. Is TrueFISP a gradient-echo or a spin-echo sequence? *Magn Reson Med* 2003;49:395-397.
21. Duerk JL, Lewin JS, Wendt M, Petersilge C. Remember true FISP? A high SNR, near 1-second imaging method for T2-like contrast in interventional MRI at .2 T. *Journal of magnetic resonance imaging : JMRI* 1998;8:203-208.
22. Zur Y, Stokar S, Bendel P. An analysis of fast imaging sequences with steady-state transverse magnetization refocusing. *Magn Reson Med* 1988;6:175-193.
23. Lauzon ML, Frayne R. Analytical characterization of RF phase-cycled balanced steady-state free precession. *Concepts in Magnetic Resonance Part A* 2009;34A:133-143.
24. Bottomley PA, Foster TH, Argersinger RE, Pfeifer LM. A review of normal tissue hydrogen NMR relaxation times and relaxation mechanisms from 1–100 MHz: Dependence on tissue type, NMR frequency, temperature, species, excision, and age. *Med Phys* 1984;11:425.
25. Wood ML, Bronskill MJ. MR desktop data. *J Magn Reson Imaging* 1992;2:13-17.
26. Bernstein MA, King KF, Zhou XJ. *Handbook of MRI Pulse Sequences*. Burlington, USA: Elsevier Academic Press; 2004. 1017 p.

27. Gold GE, Han E, Stainsby J, Wright G, Brittain J, Beaulieu C. Musculoskeletal MRI at 3.0 T: relaxation times and image contrast. *Am J Roentgenol* 2004;183:343-351.
28. Stanisz GJ, Odobina EE, Pun J, Escaravage M, Graham SJ, Bronskill MJ, Henkelman RM. T1, T2 relaxation and magnetization transfer in tissue at 3T. *Magn Reson Med* 2005;54:507-512.
29. Scheffler K. On the transient phase of balanced SSFP sequences. *Magn Reson Med* 2003;49:781-783.
30. Gyngell M. The steady-state signals in short-repetition-time sequences. *Journal of Magnetic Resonance (1969)* 1989;81:474-483.
31. Dharmakumar R, Wright GA. Understanding steady-state free precession: A geometric perspective. *Concepts in Magnetic Resonance Part A* 2005;26A:1-10.
32. Scheffler K. A pictorial description of steady-states in rapid magnetic resonance imaging. *Concepts Magn Resonance* 1999;11:291-304.
33. Schmitt P, Griswold MA, Gulani V, Haase A, Flentje M, Jakob PM. A simple geometrical description of the TrueFISP ideal transient and steady-state signal. *Magn Reson Med* 2006;55:177-186.
34. Gallo J, Kaminek P, Ticha V, Rihakova P, Ditmar R. Particle disease. A comprehensive theory of periprosthetic osteolysis: A review. *Biomedical Papers (Olomouc)* 2002;146(2):21-28.
35. Sochart DH. Relationship of acetabular wear to osteolysis and loosening in total hip arthroplasty. *Clin Orthop* 1999(363):135-150.
36. Koch KM, Hargreaves BA, Pauly KB, Chen W, Gold GE, King KF. Magnetic resonance imaging near metal implants. *Journal of magnetic resonance imaging : JMRI* 2010;32:773-787.
37. Kanal E, Shellock FG, Talagala L. Safety Considerations in MR Imaging. *Radiology* 1990;176(3):593-606.
38. Shellock FG. MR imaging of metallic implants and materials: a compilation of the literature. *AJR Am J Roentgenol* 1988;151:811-814.
39. Schenck JF. The role of magnetic susceptibility in magnetic resonance imaging: MRI magnetic compatibility of the first and second kinds. *Med Phys* 1996;23(6):815-850.

40. Wildermuth S, Dumoulin CL, Pfammatter T, Maier SE, Hofmann E, Debatin JF. MR-guided percutaneous angioplasty: Assessment of tracking safety, catheter handling and functionality. *Cardiovasc Intervent Radiol* 1998;21(5):404-410.
41. Henkelman RM, Bronskill MJ, Goebel PR. Absorption of NMR Signals at High Frequencies in Physiological Phantoms. *SPIE Medical Imaging and Instrumentation '84* 1984;486:192-197.
42. Koch KM, King KF, McKinnon GC. B1 Effects when Imaging Near Metal Implants at 3T. In: *Proceedings of the 18th Annual Meeting of ISMRM, Stockholm, Sweden, 2010*. p. 3082.
43. Levitt MH. Demagnetization field effects in two-dimensional solution NMR. *Concepts Magn Resonance* 1996;8(2):77-103.
44. Park HW, Ro YM, Cho ZH. Measurement of the magnetic susceptibility effect in high-field NMR imaging. *Phys Med Biol* 1988;33:339-349.
45. Teitelbaum G, Bradley W, Klein B. MR imaging artifacts, ferromagnetism, and magnetic torque of intravascular filters, stents, and coils. *Radiology* 1988;166:657-664.
46. Augustiny N, Vonschulthess GK, Meier D, Bosiger P. MR Imaging of Large Nonferromagnetic Metallic Implants at 1.5 T. *J Comput Assist Tomogr* 1987;11(4):678-683.
47. Farahani K, Sinha U, Sinha S, Chiu LCL, Lufkin RB. Effect of Field-Strength on Susceptibility Artifacts in Magnetic Resonance Imaging. *Comput Med Imaging Graph* 1990;14(6):409-413.
48. New P, Rosen B, Brady TJ, Buonanno F, Kistler J, Burt C, Hinshaw W, Newhouse J, Pohost G, Taveras J. Potential hazards and artifacts of ferromagnetic and nonferromagnetic surgical and dental materials and devices in nuclear magnetic resonance imaging. *Radiology* 1983;147:139.
49. Schenck JF. Quantitative Analysis of Intensity Artifacts in Spin-Echo Images Produced by Variations in Magnetic Susceptibility within the Field of View: Equations for the Rapid Determination of Susceptibilities and Analogies with Catastrophe Optics and Optical Causti. In: *Proceedings of the 1st Annual Meeting of ISMRM, New York, NY, USA, 1993*. p. 360.

50. Koch KM, Hinks RS. Empirical and Computed B0 Perturbations Induced by Metallic Implants. In: Proceedings of the 16th Annual Meeting of ISMRM, Toronto, ON, Canada, 2008. p. 1180.
51. Bartusek K, Dokoupil Z, Gescheidtova E. Magnetic field mapping around metal implants using an asymmetric spin-echo MRI sequence. *Meas Sci Technol* 2006;17(12):3293-3300.
52. Kaur P, Senthil Kumaran S, Tripathi RP, Khushu S, Kaushik S. Protocol error artifacts in MRI: Sources and remedies revisited. *Radiography* 2007;13(4):291-306.
53. Hargreaves BA, Worters PW, Pauly KB, Pauly JM, Koch KM, Gold GE. Metal-induced artifacts in MRI. *AJR Am J Roentgenol* 2011;197:547-555.
54. O'Donnell M, Edelstein WA. NMR imaging in the presence of magnetic field inhomogeneities and gradient field nonlinearities. *Med Phys* 1985;12:20.
55. Lüdeke KM, Röschmann P, Tischler R. Susceptibility artefacts in NMR imaging. *Magn Reson Imaging* 1985;3(4):329-343.
56. Sekihara K, Matsui S, Kohno H. NMR imaging for magnets with large nonuniformities. *Medical Imaging, IEEE Transactions on* 1985;4:193-199.
57. Lu WM, Pauly KB, Gold GE, Pauly JM, Hargreaves BA. SEMAC: Slice Encoding for Metal Artifact Correction in MRI. *Magn Reson Med* 2009;62(1):66-76.
58. Mechlin M, Thickman D, Kressel HY, Geftter W, Joseph P. Magnetic Resonance Imaging of Postoperative Patients with Metallic Implants. *Am J Roentgenol* 1984;143(6):1281-1284.
59. Heindel W, Friedmann G, Bunke J, Thomas B, Firsching R, Ernestus RI. Artifacts in MR Imaging after Surgical Intervention. *J Comput Assist Tomogr* 1986;10(4):596-599.
60. Bangerter NK, Hargreaves BA, Vasanaawala SS, Pauly JM, Gold GE, Nishimura DG. Analysis of multiple-acquisition SSFP. *Magn Reson Med* 2004;51:1038-1047.
61. Muir ER, Duong TQ. Layer-specific functional and anatomical MRI of the retina with passband balanced SSFP. *Magn Reson Med* 2011;66:1416-1421.
62. Petersilge CA, Lewin JS, Duerk JL, Yoo JU, Ghaneyem AJ. Optimizing imaging parameters for MR evaluation of the spine with titanium pedicle screws. *Am J Roentgenol* 1996;166(5):1213-1218.

63. Young IR, Cox IJ, Bryant DJ, Bydder GM. The Benefits of Increasing Spatial Resolution as a Means of Reducing Artifacts Due to Field Inhomogeneities. *Magn Reson Imaging* 1988;6(5):585-590.
64. Laakman R, Kaufman B, Han J, Nelson A, Clampitt M, O'Block A, Haaga J, Alfidi R. MR imaging in patients with metallic implants. *Radiology* 1985;157:711-714.
65. Guermazi A. Metallic Artefacts in MR Imaging: Effects of Main Field Orientation and Strength. *Clin Radiol* 2003;58:322-328.
66. Alanen A, Bondestam S, Komu M. Artifacts in MR Imaging Caused by Small Quantities of Powdered Iron. *Acta Radiol* 1995;36(1):92-95.
67. Czervionke LF, Daniels DL, Wehrli FW, Mark LP, Hendrix LE, Strandt JA, Williams AL, Haughton VM. Magnetic Susceptibility Artifacts in Gradient-Recalled Echo MR Imaging. *American journal of neuroradiology* 1988;9(6):1149-1155.
68. Tartaglino LM, Flanders AE, Vinitzki S, Friedman DP. Metallic Artifacts on MR-Images on the Postoperative Spine-Reduction with Fast Spin Echo Techniques. *Radiology* 1994;190(2):565-569.
69. Eustace S, Goldberg R, Williamson D, Melhem ER, Oladipo O, Yucel EK, Jara H. MR imaging of soft tissues adjacent to orthopaedic hardware: techniques to minimize susceptibility artefact. *Clin Radiol* 1997;52:589-594.
70. Ladd ME, Erhart P, Debatin JF, Romanowski BJ, Boesiger P, McKinnon GC. Biopsy needle susceptibility artifacts. *Magn Reson Med* 1996;36(4):646-651.
71. Bydder GM, Pennock JM, Steiner RE, Khenia S, Payne JA, Young IR. The Short T1 Inversion Recovery Sequence: an Approach to MR Imaging of the Abdomen. *Magn Reson Imaging* 1985;3:251-254.
72. Kim JK, Plewes DB, Mark Henkelman R. Phase constrained encoding (PACE): A technique for MRI in large static field inhomogeneities. *Magn Reson Med* 1995;33:497-505.
73. Maudsley AA, Oppelt A, Ganssen A. Rapid Measurement of Magnetic Field Distributions Using Nuclear Magnetic Resonance. *Siemens Forschungs-Und Entwicklungsberichte-Siemens Research and Development Reports* 1979;8(6):326-331.
74. Willcott MR, Mee GL, Chesick JP. Magnetic Field Mapping in NMR Imaging. *Magn Reson Imaging* 1987;5(4):301-306.

75. Yamamoto E, Kohno H. Corrections of Field Errors caused by Field Errors in MR Imaging. In: Book of Abstracts: Society of Magnetic Resonance in Medicine, New York, NY, USA, 1987. p. 402.
76. Chang H, Fitzpatrick JM. A Technique for Accurate Magnetic Resonance Imaging in the Presence of Field Inhomogeneities. *IEEE Trans Med Imaging* 1992;11(3):319-329.
77. Marques JP, Bowtell R. Application of a Fourier-based method for rapid calculation of field inhomogeneity due to spatial variation of magnetic susceptibility. *Concepts in Magnetic Resonance Part B: Magnetic Resonance Engineering* 2005;25B:65-78.
78. Salomir R, de Senneville BD, Moonen CT. A fast calculation method for magnetic field inhomogeneity due to an arbitrary distribution of bulk susceptibility. *Concepts Magn Resonance* 2003;19B:26-34.
79. Koch KM, Papademetris X, Rothman DL, de Graaf Ra. Rapid calculations of susceptibility-induced magnetostatic field perturbations for in vivo magnetic resonance. *Phys Med Biol* 2006;51:6381-6402.
80. Emid S, Creyghton JHN. Hig-Resolution NMR Imaging in Solids. *Physica B & C* 1985;128(1):81-83.
81. Gravina S, Cory DG. Sensitivity and Resolution of Constant-Time Imaging. *J Magn Reson Ser B* 1994;104(1):53-61.
82. Brown T, Kincaid B, Ugurbil K. NMR chemical shift imaging in three dimensions. *Proceedings of the National Academy of Sciences* 1982;79:3523.
83. Bendel P. Echo Projection Imaging - A Method to Obtain NMR Images Undistorted by Magnetic Field Inhomogeneities. *IEEE Trans Med Imaging* 1985;4(2):114-119.
84. Cho ZH, Ro YM. Multipoint K-space Point Mapping (KPM) Technique for NMR Microscopy. *Magn Reson Med* 1994;32(2):258-262.
85. Balcom BJ, MacGregor RP, Beyea SD, Green DP, Armstrong RL, Bremner TW. Single-point ramped imaging with T-1 enhancement (SPRITE). *J Magn Reson Ser A* 1996;123(1):131-134.
86. Robson MD, Gore JC, Constable RT. Measurement of the point spread function in MRI using constant time imaging. *Magn Reson Med* 1997;38:733-740.

87. Robson MD, Gatehouse PD, Bydder M, Bydder GM. Magnetic resonance: An introduction to ultrashort TE (UTE) imaging. *J Comput Assist Tomogr* 2003;27(6):825-846.
88. Idiyatullin D, Corum C, Park JY, Garwood M. Fast and quiet MRI using a swept radiofrequency. *J Magn Reson* 2006;181(2):342-349.
89. Rahmer J, Bornert P, Dries SPM. Assessment of Anterior Cruciate Ligament Reconstruction Using 3D Ultrashort Echo-Time MR Imaging. *J Magn Reson Imaging* 2009;29(2):443-448.
90. Gold GE, Thedens D, Pauly JM, Fechner KP, Bergman G, Beaulieu CF, Macovski A. MR imaging of articular cartilage of the knee: New methods using ultrashort TEs. *Am J Roentgenol* 1998;170(5):1223-1226.
91. Du J, Borden K, Diaz E, Bydder M, Bae W, Patil S, Bydder GM, Chung C. Imaging of Metallic Implant Using 3D Ultrashort Echo Time (3D UTE) Pulse Sequence. In: *Proceedings of the 18th Annual Meeting of ISMRM, Stockholm, Sweden, 2010.* p. 2310.
92. Carl M. MR Imaging Near Metal With 3D UTE-MAVRIC Sequences. In: *Proceedings of the 20th Annual Meeting of ISMRM, Melbourne, Australia, 2012.* p. 2434.
93. Cho ZH, Kim DJ, Kim YK. Total inhomogeneity correction including chemical shifts and susceptibility by view angle tilting. *Med Phys* 1988;15:7.
94. McGowan AJ, MacKay AL, Xiang Q-S, Connell DG, Janzen DL, Munk PL. Reduction of Image Distortion in the Presence of Metal. In: *Proceedings of the 5th Annual Meeting of ISMRM, Vancouver, BC, Canada, 1997.* p. 1973.
95. Chang SD, Lee MJ, Munk PL, Janzen DL. MRI of spinal hardware : comparison of conventional T1-weighted sequence with a new metal artifact reduction sequence. *Skeletal Radiol* 2001:213-218.
96. Olsen RV, Munk PL, Lee MJ. Metal Artifact Reduction Sequence: Early Clinical Applications. 2000:699-712.
97. Kolind SH, MacKay AL, Munk PL, Xiang Q-S. Quantitative evaluation of metal artifact reduction techniques. *Journal of magnetic resonance imaging : JMRI* 2004;20:487-495.

98. Butts K, Pauly JM, Gold GE. Reduction of blurring in view angle tilting MRI. *Magn Reson Med* 2005;53:418-424.
99. Yang QX, Williams GD, Demeure RJ, Mosher TJ, Smith MB. Removal of local field gradient artifacts in T-2*-weighted images at high fields by gradient-echo slice excitation profile imaging. *Magn Reson Med* 1998;39(3):402-409.
100. Lu W, Pauly KB, Gold GE, Pauly JM, Hargreaves Ba. Towards Artifact-free MRI near Metallic Implants. In: *Proceedings of the 16th Annual Meeting of ISMRM*, Toronto, ON, Canada, 2008. p. 838.
101. Hargreaves BA, Chen W, Lu W, Alley MT, Gold GE, Brau ACS, Pauly JM, Pauly KB. Accelerated slice encoding for metal artifact correction. *Journal of magnetic resonance imaging : JMRI* 2010;31:987-996.
102. Koch KM, Lorbiecki JE, Hinks RS, King KF. A multispectral three-dimensional acquisition technique for imaging near metal implants. *Magn Reson Med* 2009;61:381-390.
103. Venook RD, Matter NI, Ramachandran M, Ungersma SE, Gold GE, Giori NJ, Macovski A, Scott GC, Conolly SM. Prepolarized magnetic resonance imaging around metal orthopedic implants. *Magn Reson Med* 2006;56:177-186.
104. Bos C, den Harder CJ, van Yperen G. MR Imaging near Orthopedic Implants with Artifact Reduction Using View-angle Tilting and Off-Resonance Suppression. In: *Proceedings of the 18th Annual Meeting of ISMRM*, Stockholm, Sweden, 2010. p. 129.
105. Schwenk A. NMR pulse technique with high sensitivity for slowly relaxing systems. *Journal of Magnetic Resonance (1969)* 1971;5:376-389.
106. Patz S. Some factors that influence the steady state in steady-state free precession. *Magn Reson Imaging* 1988;6:405-413.
107. Ernst RR, inventor; Varian Associates, assignee. Fourier Transform NMR Spectroscopy Employing a Phase Modulated RF Carrier. US Patent 3,968,424. July 6, 1976.
108. Casselman JW, Kuhweide R, Deimling M, Ampe W, Dehaene I, Meeus L. Constructive interference in steady state-3DFT MR imaging of the inner ear and cerebellopontine angle. *American journal of neuroradiology* 1993;14(1):47-57.

109. Elliott AM, Bernstein Ma, Ward Ha, Lane J, Witte RJ. Nonlinear averaging reconstruction method for phase-cycle SSFP. *Magn Reson Imaging* 2007;25:359-364.
110. Xiang Q-S, Ye FQ. Correction for geometric distortion and N/2 ghosting in EPI by phase labeling for additional coordinate encoding (PLACE). *Magn Reson Med* 2007;57:731-741.
111. Hoff MN, Xiang Q-S. Eliminating Metal Artifact Distortion using 3D-PLACE. In: *Proceedings of the 17th Annual Meeting of ISMRM, Honolulu, HI, USA, 2009*. p. 570.
112. Mansfield P. Multi-planar image formation using NMR spin echoes. *Journal of Physics C: Solid State Physics* 1977;10:L55.
113. Bracewell RN. *The Fourier Transform and its Applications*. New York, NY: McGraw-Hill; 1986.
114. Xiang Q-S. Anti-Aliasing Acquisition for Velocity Encoded CINE. In: *Proceedings of the 9th Annual Meeting of ISMRM, Glasgow, Scotland, 2001*. p. 1978.
115. Vasanawala SS, Pauly JM, Nishimura DG. Linear combination steady-state free precession MRI. *Magn Reson Med* 2000;43:82-90.
116. Cukur T, Bangerter NK, Nishimura DG. Enhanced spectral shaping in steady-state free precession imaging. *Magn Reson Med* 2007;58:1216-1223.
117. Xiang Q-S, Hoff MN. Simple Cross-Solution for Banding Artifact Removal in bSSFP Imaging. In: *Proceedings of the 18th Annual Meeting of ISMRM, Stockholm, Sweden, 2010*. p. 74.
118. Xiang Q-S, An L. Water-fat imaging with direct phase encoding. *J Magn Reson Imaging* 1997;7:1002-1015.
119. Hoff MN, Green JD, Xiang Q-S. Imaging Near Metals with Phase-Cycled SSFP. In: *Proceedings of the 18th Annual Meeting of ISMRM, 2010*. p. 3081.
120. Scheffler K, Heid O, Hennig J. Magnetization preparation during the steady state: Fat-saturated 3D TrueFISP. *Magn Reson Med* 2001;45(6):1075-1080.
121. Hoff MN, Xiang Q-S. An Algebraic Solution for Banding Artifact Removal in bSSFP Imaging. In: *Proceedings of the 19th Annual Meeting of ISMRM, Montreal, QC, Canada, 2011*. p. 2824.

122. Candes EJ, Romberg J, Tao T. Robust uncertainty principles: Exact signal reconstruction from highly incomplete frequency information. *IEEE Trans Inf Theory* 2006;52(2):489-509.
123. Donoho DL. Compressed sensing. *Information Theory, IEEE Transactions on* 2006;52:1289-1306.
124. Storey P, Li W, Chen Q, Edelman RR. Flow artifacts in steady-state free precession cine imaging. *Magn Reson Med* 2004;51:115-122.
125. Bieri O, Markl M, Scheffler K. Analysis and compensation of eddy currents in balanced SSFP. *Magn Reson Med* 2005;54:129-137.
126. Markl M, Leupold J, Bieri O, Scheffler K, Hennig J. Double average parallel steady-state free precession imaging: optimized eddy current and transient oscillation compensation. *Magn Reson Med* 2005;54:965-974.
127. Vasanawala SS, Pauly JM, Nishimura DG. Fluctuating equilibrium MRI. *Magn Reson Med* 1999;42:876-883.
128. Overall WR, Conolly SM, Nishimura DG, Hu BS. Oscillating dual-equilibrium steady-state angiography. *Magn Reson Med* 2002;47:513-522.
129. Scheffler K, Maderwald S, Ladd ME, Bieri O. Oscillating steady states. *Magn Reson Med* 2006;55:598-603.
130. Miller KL. Asymmetries of the balanced SSFP profile. Part I: theory and observation. *Magn Reson Med* 2010;63:385-395.
131. Hargreaves BA, Vasanawala SS, Nayak KS, Hu BS, Nishimura DG. Fat-suppressed steady-state free precession imaging using phase detection. *Magn Reson Med* 2003;50:210-213.
132. Sodickson DK, Manning WJ. Simultaneous acquisition of spatial harmonics (SMASH): fast imaging with radiofrequency coil arrays. *Magn Reson Med* 1997;38:591-603.
133. Roemer PB, Edelstein WA, Hayes CE, Souza SP, Mueller OM. The NMR Phased-Array. *Magn Reson Med* 1990;16(2):192-225.
134. Hoff MN, Xiang Q-S. An XS-Guided Solution for bSSFP Banding Artifact Correction with Reduced Scan Time. In: *Proceedings of the 20th Annual Meeting of ISMRM, Melbourne, Australia, 2012.* p. 2416.

135. Kellman P, Guttman MA, Herzka DA, McVeigh ER. Phased array ghost elimination (PAGE) for segmented SSFP imaging with interrupted steady-state. *Magn Reson Med* 2002;48:1076-1080.
136. Cao Y, Levin DN. MR Imaging with Spatially Variable Resolution. *J Magn Reson Imaging* 1992;2(6):701-709.

Appendices

Appendix A Derivation of bSSFP Centre-of-Mass

The formula for bSSFP signal at $t = 0$ is given by the elliptical formulation in Eq. [2.22]

$$I(\theta) = M \frac{1 - ae^{i\theta}}{1 - b \cos \theta} \quad [\text{A.1}]$$

As previously calculated for up to $N = 6$ (23), the centre-of-mass $\langle I \rangle$ may become convoluted. However, as $N \rightarrow \infty$, the mean signal $\langle I \rangle$ may be found by integrating Eq. [A.1] over a continuous distribution of θ values from $0 \rightarrow 2\pi$

$$\langle I \rangle = \frac{1}{2\pi} \int_0^{2\pi} I(\theta) d\theta = \frac{M}{2\pi} \int_0^{2\pi} \frac{1 - ae^{i\theta}}{1 - b \cos \theta} d\theta \quad [\text{A.2}]$$

which may be simplified to

$$\langle I \rangle = M \left(1 + \frac{b - a}{\pi} \int_0^{\pi} \frac{\cos \theta}{1 - b \cos \theta} d\theta \right) \quad [\text{A.3}]$$

The integral in Eq. [A.3] may be found in a table of definite integrals (Gradshteyn IS, Ryzhik IM. Table of Integrals, Series, and Products: Academic Press; 2007):

$$\int_0^{\pi} \frac{\cos n\theta}{1 + a \cos \theta} d\theta = \frac{\pi}{\sqrt{1 - a^2}} \left(\frac{\sqrt{1 - a^2} - 1}{a} \right)^n \quad a^2 < 1 \quad [\text{A.4}]$$

Substitution of [A.4] into [A.3] yields the closed-form expression for the centre-of-mass given in Eq. [2.24]

$$\langle I \rangle = M \left[1 + \frac{b - a}{b} \left(\frac{1}{\sqrt{1 - b^2}} - 1 \right) \right] \quad [\text{A.5}]$$

Appendix B Proof: The bSSFP Ellipse Must Be Vertical in the Complex Plane

Equation [2.26] and Figure 2.11a inform that for the bSSFP signal ellipse to be horizontal in the complex plane

$$b > \frac{2a}{1 + a^2} \quad [\text{B.1}]$$

Insertion of the parameters a and b from Eqs. [2.18] and [2.19] yields

$$\frac{E_2(1 - E_1)(1 + \cos \alpha)}{1 - E_1 \cos \alpha - E_2^2(E_1 - \cos \alpha)} > \frac{2E_2}{1 + E_2^2} \quad [\text{B.2}]$$

Following algebraic manipulation, the expression becomes

$$\cos \alpha - E_1 + E_2^2 - E_1 E_2^2 \cos \alpha > 1 - E_1 \cos \alpha - E_1 E_2^2 + E_2^2 \cos \alpha \quad [\text{B.3}]$$

which can be factored to yield

$$(1 - \cos \alpha)(E_2 - 1)(E_2 + 1)(E_1 + 1) > 0 \quad [\text{B.4}]$$

Since $0 < E_1, E_2 < 1$ and $-1 < \cos \alpha < 1$, all bracketed terms are positive except the 2nd, which is always negative. Thus Eq. [B.4] and subsequently Eq. [B.1] is incorrect, and the ellipse cannot be horizontal. For the ellipse to be a circle, the left hand side of Eq. [B.4] must equal zero, achieved by $E_2 = 1$ or $\alpha = 0$. Since neither is a reasonable assumption, the ellipse must be vertical in the complex plane.

Appendix C Derivation of a Minimal-Variance Sum of Two Images

A weighted sum I_w of two images $I_1 = I_0 + n_1$ and $I_2 = I_0 + n_2$ with base signal I_0 and noise n_1 and n_2 respectively may be given by:

$$I_w = wI_1 + (1 - w)I_2 \quad [\text{C.1}]$$

For i observations with uncorrelated noise of standard deviation σ_i , the weighted sample mean of all observations has variance $\sigma^2 = \sum_i w^2 \sigma_i^2$. I_w then has a variance σ_w^2 given by

$$\sigma_w^2 = w^2 \sigma_1^2 + (1 - w)^2 \sigma_2^2 \quad [\text{C.2}]$$

The optimal weighting of I_1 and I_2 is defined here to yield a minimum value of σ_w^2 . This is found by solving $\partial \sigma_w^2 / \partial w = 0$ for w to yield

$$w = \frac{\sigma_2^2}{\sigma_1^2 + \sigma_2^2} \quad [\text{C.3}]$$

which when input into Eq. [C.1] yields

$$I_w = \frac{\sigma_2^2}{\sigma_1^2 + \sigma_2^2} I_1 + \frac{\sigma_1^2}{\sigma_1^2 + \sigma_2^2} I_2 = \frac{\sigma_2^2 I_1 + \sigma_1^2 I_2}{\sigma_1^2 + \sigma_2^2} \quad [\text{C.4}]$$

which is the result stated in Eq. [5.11].